UNIVERSITY OF CALIFORNIA
RIVERSIDE

Morphological Study on Polyaromatic Carbon-Based Materials

A Dissertation submitted in partial satisfaction
of the requirements for the degree of

Doctor of Philosophy

in

Chemistry

by

Wangxiang Li

December 2021

Dissertation Committee:
Dr. Christopher J. Bardeen, Chairperson
Dr. Elena B. Haddon
Dr. Ludwig Bartels

The Dissertation of Wangxiang Li is approved:

_____

_____

_____

Committee Chairperson

University of California, Riverside

Acknowledgment

First, I would like to express my gratitude to Prof. Christopher Bardeen. Chris is a great mentor and inspiring scientist. He always has cool ideas with pretty high success rate. When I have ideas, which could be stupid sometimes, he also allows me to explore them with considerable freedom, encouraging me to be an independent researcher. After almost five years working with him, Chris has taught me not only the knowledge of chemistry, but also humble and open-minded attitudes towards scientific research. This long journey of PhD becomes quite fruitful and surprisingly pleasant under his mentorship. I am really lucky to have Chris as my supervisor during my PhD.

Second, I would like to thank Dr. Elena B. Haddon as my co-adviser. During the early years when I was still a freshman who knew nothing about research, Elena trained me on instruments and techniques with full patience. After the sudden passing of Dr. Robert Haddon, she has given me and my colleague Mingguang maximum support to keep pursuing the unfinished projects. After joining Chris' group, she still selflessly allows me to use resources in Haddon's lab to finish my PhD study and provides me with scientific guidance when I encounter research obstacles. I am fortunate to have Elena as my co-advisor during this journey.

I am also very grateful to Dr. Robert Haddon, who first took me in during my study at UCR as a visiting undergraduate student and later gave me an opportunity to study as a PhD researcher in his group. His passion and dedication to science always inspire me up to the present and make me believe that doing science can be a rewarding lifetime job.

I also would like to thank Dr. Mingguang Chen, my senior colleague in Haddon's group. Working with him during my early years helped me build a good foundation of experimental skills and problem-solving mindsets that go a long way in my later PhD study.

I want to thank Dr. Yan Dong, the ace engineer (now the manager) of the cleanroom. Whenever a new idea comes up that requires fabrications, he is my first person to ask for checking the feasibility. Without help from him, I believe my projects would proceed much slower.

I thank Dr. Joshua Lui for important guidance in both life and science. I thank my wonderful colleagues and collaborators: Dr. Mikhail Iktis, Dr. Kerry Hanson, Adam Berges, Nathen Tierce, Dr. Jeremiah van Baren, Dr. Fei Tong, Dr. Xinning Dong, Thomas Gately, Brandon Lui, Taylor Lewis, Dr. Hossein Mostafavi, Dr. Hao Tian, Dr. Guanghui Li, Dr. Dejan Stekovic, Dr. Mashael Altaiary, Dr. Bassim Arkook, Dr. Song Wang. I will not be able to finish my work without help from them.

At last, I would like to give my sincere thanks to my family for their unconditional love and support.

Portions of the dissertation are adapted with permission from the following references:

Chapter 3:

Li, W.; van Baren, J.; Berges, A.; Bekyarova, E.; Lui, C. H.; Bardeen, C. J., Shaping Organic Microcrystals Using Focused Ion Beam Milling. *Crystal Growth & Design* **2020**, 20 (3), 1583-1589.

Chapter 4:

Li, W.; Tierce, N. T.; Bekyarova, E.; Bardeen, C. J., Protection of Molecular Microcrystals by Encapsulation under Single-Layer Graphene. *ACS Omega* **2018**, 3, 8129-8134.

Chapter 5:

Li, W.; Tian, H.; van Baren, J.; Berges, A.; Altaiary, M. M.; Liu, E.; Bekyarova, E.; Lui, C. H.; Liu, J.; Bardeen, C. J., Hexagonal Boron Nitride Encapsulation of Organic Microcrystals and Energy-Transfer Dynamics. *Journal of Physical Chemistry C* **2020**, 124 (38), 21170-21177.

Chapter 6:

Chen, M.; Li, W.; da Silveira Venzel, T. E.; Li, G.; Itkis, M. E.; Haddon, R. C.; Bekyarova, E., Effect of constructive rehybridization on transverse conductivity of aligned single-walled carbon nanotube films. *Materials Today* **2018**, 21 (9), 937-943.

ABSTRACT OF THE DISSERTATION

Morphological Study on Polyaromatic Carbon-Based Materials

by

Wangxiang Li

Doctor of Philosophy, Graduate Program in Chemistry
University of California, Riverside, December 2021
Dr. Christopher J. Bardeen, Chairperson

Polyaromatic carbon-based materials, including polyaromatic hydrocarbons (PAH), graphene, and carbon nanotubes (CNT), are envisioned to be widely used in next-generation electronics for their great properties, richness in richness source materials, adaptability in applications, and scalability. Morphological engineering of materials' shape, size, surface, and orientation is necessary to control their mesoscopic properties and incorporate them into practical electronic devices. This dissertation explores different strategies to control the morphology of polyaromatic carbon-based materials and also investigates the accompanied morphological effect that changes materials' properties.

PAH monomers have many novel excitonic properties. By packing them orderly, monomers can be assembled into molecular crystals suitable for solid-state organic electronics. However, a general method to control the shape of molecular crystals after growth is still lacking. One of the intuitive ways to shape an object is using a knife to cut

or sculpt it. Therefore, in Chapter 3, a hypothetical knife made of a focused ion beam (FIB) will be used to shape PAH microcrystals. A stream of high-energy Ga^+ ions are used to mill organic perylene crystals coated with a chemically removable gold layer. A programmable FIB blade can machine crystals into arbitrary shapes. The cutting resolution of FIB is found to be about 130 nm. Perylene crystals retain 90% of its original fluorescence after the whole shaping process. This experiment provides a general way to control the shape and size of polyaromatic crystals in a top-down fashion.

Another problem limiting the potential of PAHs is that bare molecular crystals can be easily corroded by solvents, moisture, heat, and vacuum. Even if we manage to control crystals' bulk shape, these surface corrosions can still exclude PAHs from many practical applications. So, in Chapter 4, an impermeable atomic blanket—graphene is draped on molecular crystals to passivate their surfaces and protect them from the environment. Graphene successfully encapsulates perylene microcrystals grown on glasses, protecting the sample from solvent dissolution and sublimation at high temperatures. No detectable impact is found on the fluorescence lifetime of underneath thick crystals with thicknesses around 150 nm.

In Chapter 5, the quenching effect at the graphene/PAH interface is further investigated by interfacing graphene with dye-doped emitting polymer films with various thicknesses. Time-resolved PL measurements are done on these samples. A quenching radius of 14.6 nm is extracted from the fitting of a series of PL decay data. Therefore, graphene encapsulation is still not a perfect solution since graphene can quench the molecules near the interface. An insulating few-layer hexagonal boron nitride (h-BN) is then used as an

alternative protective layer to further eliminate the quenching effect at the interface. h-BN also successfully protects perylene crystals from solvent and heat. Surprisingly, wet-transferred h-BN is not totally inert but has a quenching radius of 2.9 nm. This quenching effect can be avoided by the dry transfer method that minimizes the lattice distortion and breakage from liquids (etching solutions and solvents). The work demonstrates the possibility of protecting molecular crystals by interfacing them with 2D materials. The investigated charge transfer dynamics provides guidance for the design of perspective organic/2D heterostructure devices

Similar to PAH molecules, individual CNTs can also be assembled into macroscopic solid CNT networks by the filtration method. However, the randomly oriented network structure deteriorates films' conductivity because of inter-tube junctions that hinder the carrier transport. Thus, in Chapter 6, the filtration method is modified to produce aligned CNT thin films. The film's conductivity is improved in the alignment direction because of a reduction in the number of junction sites. Chromium surface functionalization that connects adjacent CNTs is then applied to reduce the junction resistance further. Cr atoms are inserted between CNTs by photochemistry to provide electrical channels at junctions for carriers to pass through. A reversible switch is also built to demonstrate the reversibility of this Cr functionalization.

Table of Contents

List of Tables

List of Figures

Chapter 1. Introduction

Morphology means the form, shape, or structure of things. The morphological study of nature has always been a central topic for philosophers and scientists since ancient times. Why do the sun and the moon appear to be round and nearly the same size? What is the shape of the earth, flat or spheric? Why can water transform between ice, liquid, and vapor? How does a microscopic cell grow into a meter-scale adult? Those questions drive humanity to think, explore, and experiment up to the present, creating the scientific society we have today. Various instruments like telescopes, microscopes, ultrasound have been developed along the way to observe the shape of our research targets. Tools like bombs, blades, lasers, synchrotrons have also been made to manipulate the morphology on the scale from terrain to atoms. Theories that connect the structure of matter to its properties have been continuously expanded and improved.

In the field of chemistry, studying and engineering the morphologies of functional materials has practical value for real-world applications in both academia and industry. Polyaromatic carbon-based materials have been intensively studied during the recent decades. They are envisioned to be the alternative to silicon for next-generation electronics because of its novel electro-optical properties, abundance in raw material, low-production cost, versatility in form, and scalability.[1-4] The research in this thesis is focused on the morphological study and engineering of polyaromatic carbon-based materials. Three different types of polyaromatic materials are investigated: polyaromatic hydrocarbons, graphene, and carbon nanotubes.

This chapter is divided into two major parts. The first part (Page 2-27) introduces three carbon-based materials in terms of their structures, properties, morphologies, and applications. The second part (Page 28-33) delivers an overview of the morphological study contributed by this thesis on these polyaromatic carbon-based materials.

1.1 Introduction of polyaromatic carbon-based materials

This part is an introduction of three different kinds of polyaromatic carbon-based materials: polyaromatic hydrocarbon, graphene, and carbon nanotubes. Their molecular structures, properties, morphologies, and applications that related to my research are elaborated in respective sub-chapters.

1.1.1 Polyaromatic hydrocarbon molecules

Polycyclic aromatic hydrocarbons (PAHs) refer to a large class of organic molecules containing multiple aromatic rings. This conjugated system is widely studied in many research fields of chemistry and material science. PAHs have been used as the building block to synthesize other carbon materials of interest in this thesis--graphene and carbon nanotubes. [5-6] For fundamental science, PAHs can serve as a reliable platform for studying novel quantum dynamics of the exciton.[7] In the field of astrophysics, the light emitted from PAHs provides us with valuable information about interstellar chemistry.[8] PAHs, in their crystalline form, are also a promising candidate for organic optoelectronic devices.[1] This sub-chapter provides a brief overview of PAHs, illustrating their molecular structures, properties, morphology, and applications related to my Ph.D. research.

Molecular structure

The simplest PAHs are naphthalene, composed of two fused benzene rings and tricyclic anthracene, as shown in Figure 1.1. Due to the rigid sp^2 network of the aromatic rings, most PAH molecules maintain a planer structure even with large molecular dimensions, like ovalene.[9] However, in some cases, steric hindrance forces the molecule to take a non-planer form, like the concaved bowl shape adopted by corannulene to reduce bond stress.[10]

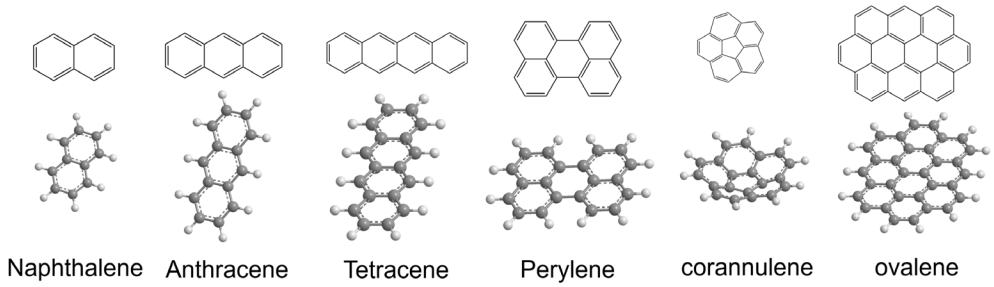

Figure 1.1. Molecular structure of polyaromatic hydrocarbon molecules.

Electronic structure

The sp^2 hybridization grants PAHs a highly conjugated molecular structure. Strong π-π interactions between p_z orbitals allow electrons to be delocalized across the whole molecule. The highest occupied molecular orbital (HOMO) and lowest unoccupied molecular orbital (LUMO) determine the excitonic behaviors of PAHs. The energy gap between HOMO and LOMO is a critical parameter determining various properties of PAH molecules. Due to the conjugated structure of the PAH, the magnitude of the HOMO-LUMO gap (ΔE_G^{H-L}) is closely correlated with the molecular size.[11-12] Detailed theoretical calculations were carried out by Ruiz-Morales, showing that the magnitude of PAHs' ΔE_G^{H-L} is not only related to the number of fused rings but also the compactness of the ring

arrangement. If all rings are arranged in a linear form, the magnitude of ΔE_G^{H-L} is inversely proportional to the number of the rings. When two molecules have the same aromatic ring count (anthracene and phenanthrene, for example), the more compact isomer will have a wider energy gap.[12] The far end of this trend brings us another target material of this thesis—graphene. With an almost infinite amount of the aromatic ring arranged in a planar form, graphene has a zero bandgap.[13] The details about graphene will be further elaborated in sub-chapter 1.3.

The magnitude of the ΔE_G^{H-L} reveals the semiconducting nature of most PAHs. With a few exceptions of really compact molecules like naphthalene and phenanthrene, the ΔE_G^{H-L} of PAHs are mostly smaller than 4 eV, so they can be categorized as wide-bandgap semiconductors.[12] In addition, the ΔE_G^{H-L} of PAH is correlated with its optical band gap($\Delta E_G^{Optical}$), which is the energy difference between the ground state and the first excited state during exciton formation. Due to the electrostatical binding of the electron-hole pair, $\Delta E_G^{Optical}$ is smaller than ΔE_G^{H-L} by the exciton binding energy.[14] $\Delta E_G^{Optical}$ determines the absorption and emission properties of PAHs. Similar to ΔE_G^{H-L}, $\Delta E_G^{Optical}$ also depends on the size of the conjugated system. The most compact PAHs such as naphthalene and anthracene absorb in UV (<400 nm) and emit in the ultraviolet to blue region.[15] Larger PAHs like tetracene and perylene absorb violet-blue light and emit visible light from cyan to red.[16-17] The wide variety in PAH sizes gives us an abundant library of light-sensitive materials to work with according to specific applications.

After PAHs molecules are packed together orderly into molecular crystals, the overlap of the π-molecular orbitals between adjacent molecules gives rise to the metallic conductivity

in charge transfer crystals.[18] Similar to the discovery of metallic properties and superconductivity in alkali-doped carbon fullerenes[19-21], intercalating alkali-metal atoms into some PAH systems are also found to induce the unconventional superconductivity with the critical temperature up to 33K.[22-23]

Excitonic dynamics

The light-matter interaction is a long-standing research topic in PAHs. Many novel phenomena happen by simply shining light on these molecules. The Jablonski diagram is a famous and useful picture that illustrates the relaxation dynamics in electronic states during and after photoexcitation.[24] Here an overview will be given of the excitonic processes after irradiating PAH molecules.

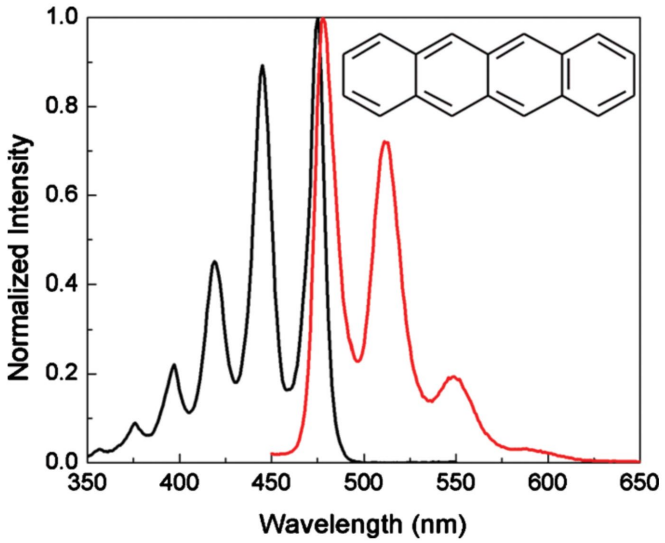

Figure 1.2. Absorption and emission spectra of tetracene dissolved in toluene.[16] Copyright (2010) AIP Publishing.

Absorption: Due to the fact that PAHs have much more complex skeletons than single atoms, each electronic state gives rise to many vibronic states from atomic motions. Thus,

the absorption of PAHs consists of several vibronic peaks, like the plot in Figure 1.2, showing the absorption spectra of tetracene monomer in toluene. In the Jablonski diagram in Figure 1.3, the purple arrow represents the absorption process. When a photon hits the PAH molecule, one of the electrons in S_0 ground state is excited into vibrational states in the S_1 to form a singlet. Different peaks in the absorption spectrum represent different vibronic states in S_1. The absorption (excitation) process is extremely fast on the order of 10^{-15} s. The intensity of peaks is determined by Franck–Condon principle, from which the transition with minimal atomic coordinate (or atomic motion) change has the highest probability.

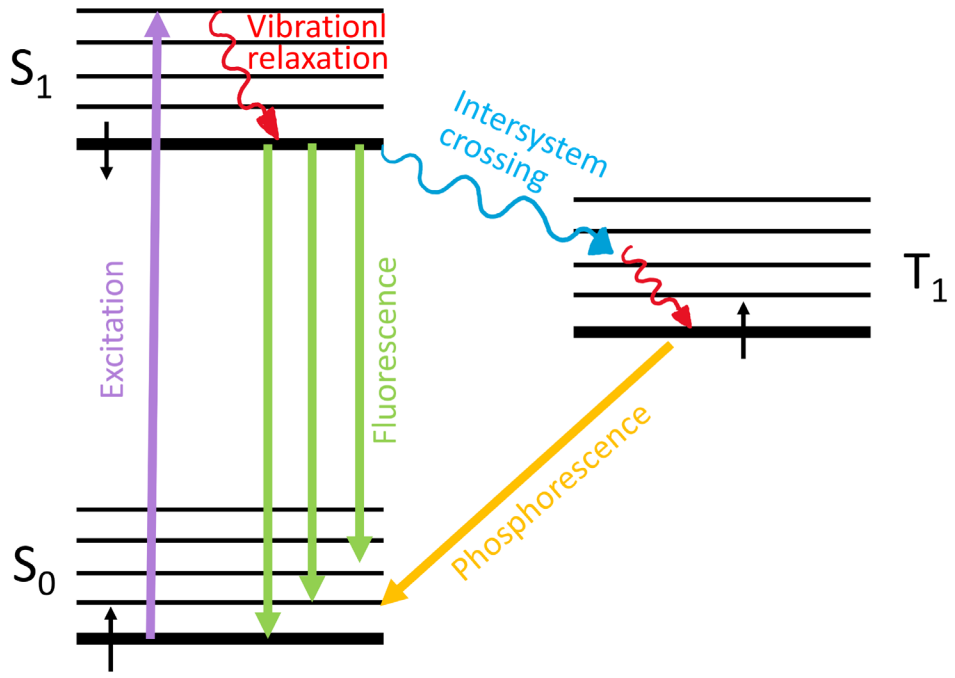

Figure 1.3. Jablonski diagram of absorption and emission processes.

Emission: PAH emission is a more complicated process than absorption. After the electron is excited, internal conversion and vibrational relaxation happens next at the rate of 10^{-12}

s. The excited electron then relaxs to the lowest vibronic state. The energy is dissipated non-radiatively in this process, causing the Stoke shift of the emission spectrum, which is red-shifted compared with the absorption as shown in Figure 1.2. The excited state can relax back to different ground vibronic states in S_0, generating multiple peaks in the emission spectrum. The probabilities of the electron falling into each vibronic state are also ruled by Franck–Condon principle. The relaxation rate is on the order of 10^{-9}, which is slower than absorption and vibrational relaxation. Fluorescence will always happen after vibrational relaxation. The significant kinetic difference between radiative recombination and vibrational relaxation constitutes Kasha's rule: Photoemission occurs only at the lowest level of the excited state.[25] In theory, the excitation wavelength generally will not affect the quantum yield of the singlet emission. Kasha's rule and the Frank-Condon principle together lead to the mirror symmetry between absorption and emission spectra of PAH monomers.[24] The time window for the singlet to recombine is labeled as singlet lifetime, which can be probed with time-resolved photoluminescence spectroscopy.

Apart from direct radiative recombination, the newly created exciton can also go through intersystem crossing (blue wavy line in Figure 1.3) and relax to a lower T_1 state to form a triplet. This spin-flip process is mainly due to the spin-orbit coupling between the excited electron and its surrounding magnetic field from molecular orbitals. The magnitude of spin-orbit coupling is proportional to the atomic number of the nuclei. Previous work has shown that introducing heavy metal atoms into the PAH matrix is effective in facilitating the intersystem crossing process.[26] The direct radiative transition from T_1 to S_1 emits phosphorescence. The rate of this transition is very slow as a consequence of being a spin-

forbidden transition. Typical phosphorescence lifetimes (or triplet lifetimes) are in the range of $>10^{-6}$ s.[24] There are also two other indirect triplet radiative transitions producing delayed fluorescence in many PAHs molecules, such as anthracene, tetracene, and rubrene. One of them is thermally activated delayed fluorescence, where the population in T_1 jumps back to the S_1 state if the thermal energy is greater than the gap between T_1 and S_1.[27] Delayed fluorescence can also realized by triplet-triplet annihilation (TTA), in which two triplets in two molecules fuse, leaving one molecule in the S_1 state while the other goes back to S_0.[28] Both transitions emit the same spectra as the singlet radiative recombination.

Non-radiative recombination of excitons

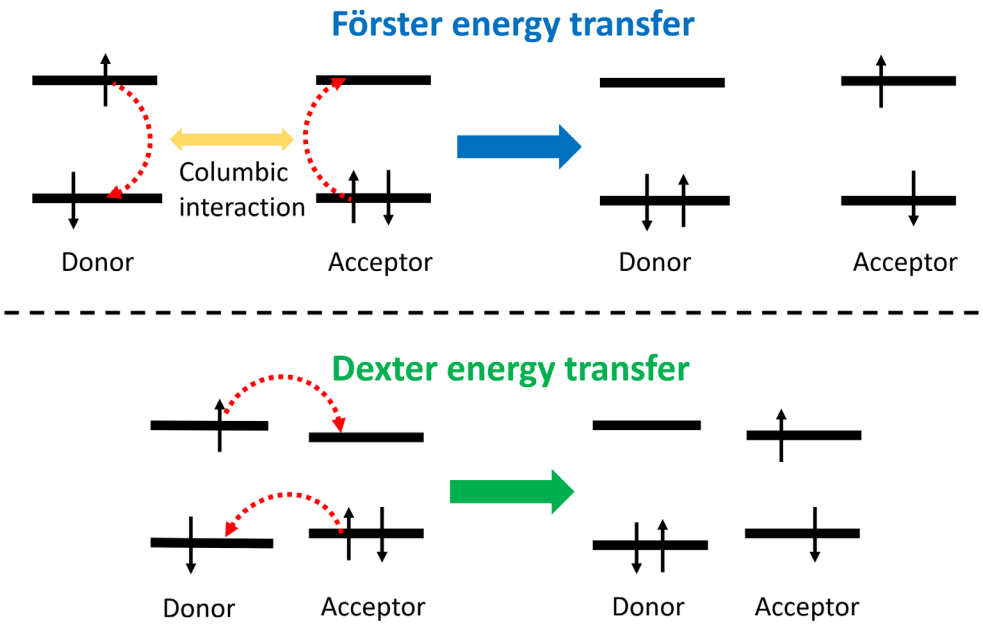

Figure 1.4. Schematic of Förster and Dexter energy transfer processes.

After we excite PAH molecules, the exciton can also relax through non-radiative processes that kinetically compete with the radiative processes mentioned above. The non-radiative

process has also been called quenching because photoluminescence from the molecule can be suppressed if the non-radiative recombination outcompetes the radiative recombination. Internal conversion is one possible process that takes the molecule to its ground state, releasing energy as heat. Another possible process is the energy transfer between the excited molecule and its surroundings. There are two mechanisms to describe the energy transfer according to the spatial distance between two transfer participants.

Förster resonance energy transfer (FRET) describes long-range (1 to 10 nm) energy transfer between two fluorophores based on the electrostatic dipole-dipole interaction.[29] The theory can also be extended to other low/zero bandgap materials, such as carbon nanotube and graphene, which can also serve as quenchers. Due to the distance separation between donor and acceptor, the individual electron does not migrate out of its original host molecule. The upper part of Figure 1.4 shows the schematic of this process. In the donor molecule, the excited singlet recombined by releasing a virtual photon. The virtual photon is then absorbed by the acceptor molecule. The overlap between emission spectra of the donor and absorption spectra of the acceptor is one of the prerequisites for the energy transfer to happen, meaning that the optical bandgap of the donor needs to be equal or wider than the optical bandgap of the acceptor. The efficiency of FRET is very sensitive to the distance R between donor and acceptor. The conventional Förster energy transfer rate constant is described by Eqn. (1) and (2)[30]:

$$k_{ET} \propto \left(\frac{R_0}{R}\right)^6 \frac{1}{\tau_D} \quad (1)$$

$$R_0 \propto \frac{J\phi_D\kappa^2}{n^4} \quad (2)$$

where R is the distance between the donor (D) and acceptor (A). R_0 is the Förster distance at which the energy transfer efficiency is 50%. τ_D is the donor's fluorescence lifetime without the presence of the acceptor. J is the spectral overlap integral between two molecules. ϕ_D is the donor quantum yield in the absence of the acceptor. κ^2 is the orientation factor which describes the relative orientation between two dipoles. n is the refractive index of the medium.

If the donor and acceptor are all point dipoles (single molecules), the efficiency is inversely proportional to R^6. Some works have shown that the FRET efficiency between a molecule and 2D graphene has a R^{-4} dependence.[31] The quenching effect due to a fullerene can be analogous to the single-molecule case with R^{-6} dependence.[32]

Dexter energy transfer describes short-range excitonic interactions, typically within 1 nm. The process requires wavefunction (orbital) overlap between the donor and the acceptor to facilitate the inter-molecule charge transfer.[33] The process is illustrated in the bottom part of Figure 1.4. This process allows both singlets and triplets to transfer their energy to another molecule through the spin-allowed electron exchange process. An excited electron in the donor molecule flows from its S_1 or T_1 state to the acceptor's S_1 or T_1 state. The ground-state electron in the acceptor transitions to the S_0 state of the donor. When designing an energy transfer heterostructure based on the Dexter mechanism, not only does the bandgap magnitude requirement mentioned in the FRET section need to be satisfied, the relative energy level values of two molecules also should be considered. The excited state of the acceptor should not be higher than the excited state of the donor. The ground state of the donor also needs to be lower or equal to the acceptor ground state.

The efficiency of Dexter energy transfer is also strongly dependent on the inter-molecular distance. The rate constant of this process is shown in Eqn. (3),[34]

$$k_{ET} \propto Je^{\frac{-2R}{L}} \quad (3)$$

where R is still the distance between the donor and acceptor, L is the sum of their van der Waals radii, and J is the spectral overlap integral.

Sample preparation methods and applications

PAHs can be dissolved in organic solvents to form a solution. At low concentrations, PAHs are separated by the solvent molecules. The properties of the individual molecule with all degrees of vibrational freedom can be probed when PAH is in this state. When the concentration is high, the distance between PAHs becomes small enough to allow inter-molecular interaction to take place. The spectra will be altered by the interactions between molecules.[35] The solution state of PAH is usually used in fundamental research for studying excitonic dynamics. PAH molecules can also be chemically or physically embedded in a polymer matrix, such as microbeads and thin films, to form light-sensitive composites.[36-37] PAH functionalized fluospheres are widely used in biological microscopy as fluorescence probes to image the biological cells.[37-38] Polymer thin films doped with PAHs have been fabricated into optical waveguiding devices.[39] PAHs can be crystallized by solvent recrystallization and physical vapor deposition.[40-41] Solution drop-casting with controlled temperature and concentration is a simple way to grow single crystals with low defect density.[42] Vapor deposition can be used to grow polycrystalline thin film with controllable thicknesses.[43] Close packing of molecules in solid-state contributes many unique properties distinct from the monomer, such as delocalization of charged carriers and enhanced exciton

diffusion.[7] Crystalline PAHs has also been envisioned as a promising materials for organic electronics. Pentacene, anthracene, and rubrene crystals have been used as the active layer for organic field-effect transistors, which can be gated both electrically and optically.[1, 4] Tetracene solid films has been applied onto silicon as a sensitizer to improve the solar cell efficiency by singlet fission.[44] PAHs molecule

Morphology engineering of PAH crystals

The physical properties of a PAH crystal depend not only on the molecule type, but also on the morphological difference in size, shape, orientation, and surface. Morphology modulation is an effective route to tune the properties of molecular crystals for different applications.

Crystal growth and polymorphism: Crystal growth is the primary step that influences the morphology of PAH crystals. Nowadays, despite all kinds of technological advancement, molecular crystal growth is still considered an art by most chemists due to its requirement of dedication to the details, repetitive trial and errors, and a bit of luck. One of the fundamental reasons behind that is polymorphism.[45] Polymorphism is referred to the variety of crystal structure arrangements in solid crystals. Differences in molecular packing and orientation create macroscopic morphological diversity of the bulk crystal. Here I will use perylene as an example to demonstrate polymorph control in crystal growth and the effect of polymorphism on the crystal properties.

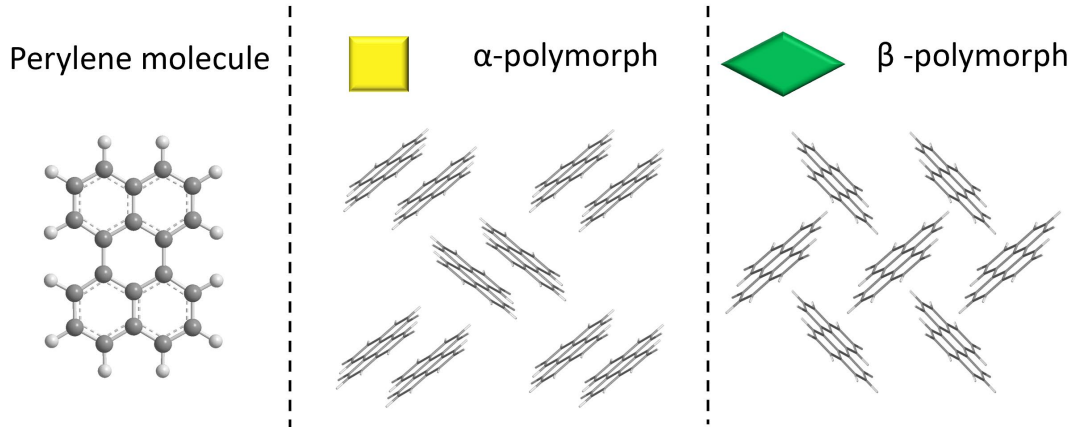

Figure 1.5. Perylene's molecular structure and the crystal packing of its α- and β-polymorphs. The shape and fluorescence color of two polymorphs are also different from each other.

Perylene is a PAH with two polymorphs, denoted as the α- and β-phases, which have different packing motifs.[41] Perylene in the α-polymorph packs in a dimeric sandwich-herringbone motif, while in the β-phase, molecules are arranged in a monomeric γ-herringbone structure, as illustrated in Figure 1.5. Macroscopically, α-crystals adopt quadratic shapes with 92º corner angles, and β-crystals grow in rhombic shapes with 122º corner angles.[41] Selective growth of each polymorph has been studied in the past. Yago et al. showed that rapid cooling (-30K/min) of a saturated solution could preferentially precipitate β-polymorph while slow cooling (-1K/min) favors the growth of α-polymorph.[46] Pick et al. demonstrated that keeping the growth substrate at high temperature with a low vapor deposition rate exclusively forms α-phases. Lowering the temperature and increasing the rate allows a notable portion of β-polymorph to be crystallized.[41] Both works indicate that kinetic control of crystal growth is essential for polymorph selection.

Physical property differences from polymorphism: Because of different molecular packing motifs and intermolecular interactions, the α- and β-polymorphs of perylene

exhibit different absorption and emission properties. Under excitation, the green fluorescence of β-polymorph is noticeably blue-shifted compared to the yellow color of α-phase as showed in Figure 1.5.[40] The shorter intermolecular distance and the face-to-face packing motif of perylene molecule in α-polymorph enhance the intermolecular π-π interaction, allowing a larger electron delocalization within the crystal. Therefore, the α-polymorph has a smaller bandgap than its counterpart. From theoretical calculations, the carrier mobilities in the α-polymorph are also higher than the β-polymorph.[47] Both electrical and optical properties of perylene can be tuned by the selective growth of polymorphs.

Other morphology control beyond crystal packing: There are other morphology control methods besides using polymorphism. Anodic aluminum oxide template growth has been used to grow photomechanical nanorods of anthracene derivatives.[48] The resulting composite could exhibit a photo-induced bending motion. Well-designed pentacene, rubrene and fullerene crystal arrays have been achieved by substrate functionalization and patterning, allowing further fabrications of organic transistor circuits on a single substrate.[4] Oxygen plasma etching has been used to pattern pentacene thin-film transistor in conjunction with a layer of water-soluble photoresist.[49] The surface roughness of vapor-deposited perylene thin films could also be reduced down to sub-nm level by plasma polymerization to reduce the light scattering on the wafer-scale.[50]

1.1.2 Graphene

Graphene can be viewed as an infinite extension of a planer polyaromatic hydrocarbon molecule. It is a monolayer conjugated sp^2 carbon network arranged in a two-dimensional

honeycomb lattice.[51] Since the discovery by Geim and Novoselov using scotch tape exfoliation of graphite, graphene has attracted numerous attention from many fields of science for its distinctive electronic, optical and mechanical properties.[13, 52] Up to the present, a large variety of real-world applications, from smartphone screens to tennis rackets, has been realized based on graphene. This sub-chapter provides a short introduction about the structure, properties, morphological effects, and applications of graphene.

Structure

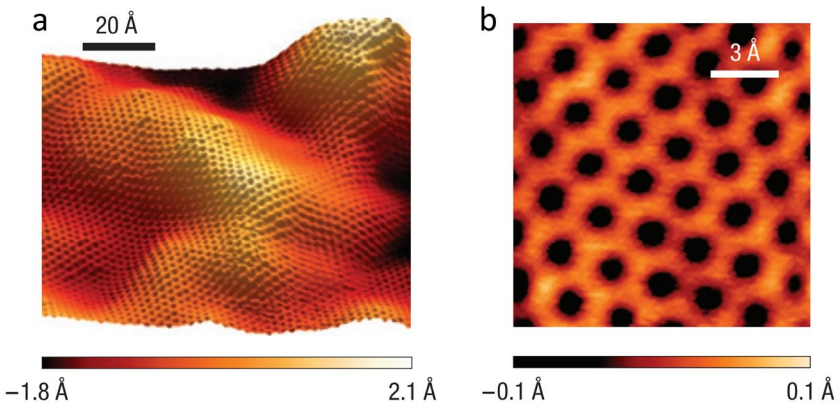

Figure 1.6. a) STM topograph of a graphene flake above a SiO_2 substrate. **b)** Close-up STM scanning of the graphene honeycomb lattice.[53] Copyright (2008) Springer Nature.

Graphene's primitive cell contains two carbon atoms (A and B) as shown in Figure 1.7a. Each carbon atom (A for example) is covalently bonded with three other carbon atoms (B) through σ-bonds between hybridized s, p_x, p_y orbitals. The leftover valence electron in each carbon stays in p_z orbitals interconnected through π-bonds. The conjugated network allows the π-electron to be delocalized across the entire lattice, resulting in graphene's superior conductivity. The thickness of graphene is only 0.345 nm (basically one-atom-thick).

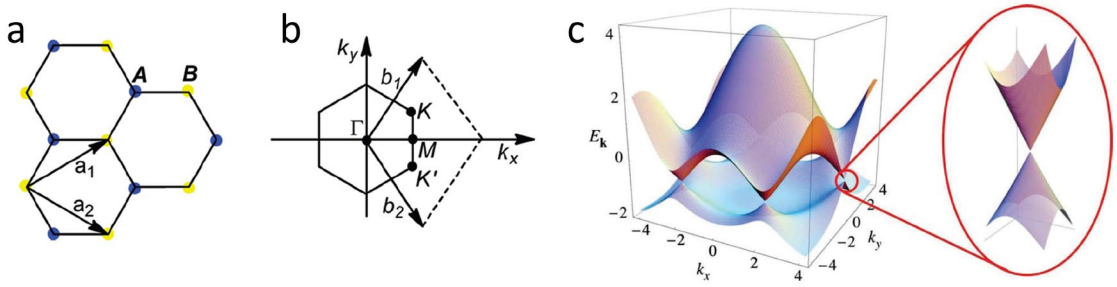

Figure 1.7. a) Real space graphene lattice, showing the unit cell vectors and **b)** Brillouin zone of graphene in momentum space. **c)** Graphene energy band dispersion in momentum space.[51] Copyright (2009) American Physical Society.

Electronic properties

Graphene is a zero-bandgap semiconductor as indicated by the band structure in Figure 1.7c.[51] Due to its unique structure, graphene has an ultra-high room-temperature carrier mobility > 200,000 $cm^2/(Vs)$, which is more than 100 times that of crystalline silicon (1400 cm^2/ Vs).[54] The carrier concentration in graphene can be easily tuned bipolarly with electro-capacitance gating or doping from the environment.[55] Chemical functionalization and dimension control (graphene nanoplatelets) can open a bandgap in graphene to enhance the on/off ratio for transistor-type devices.[56-57] Stacking two pieces of graphene together with an angle mismatch creates a Moire-superlattice. When the mismatch angle is at 1.1º (magic angle), stacked graphene exhibits low-temperature superconducting and insulating behavior controlled by electrical gating.[58-59]

Optical properties

Graphene has a near-constant absorbance of 2.3% in the visible light region.[60] This non-trivial absorbance allows researchers to directly observe this one-atom-thick film with the naked eye. Other visualization techniques such as AFM, TEM and SEM all failed to hunt

down graphene in the first place because of the extremely weak contrast from its atomic thickness. The traditional optical microscope can easily detect single-layer graphene on a standard 300 nm SiO_2/Si wafer based on the contrast as demonstrated in Figure 1.8.[61] Graphene becomes more accessible because of its optical visibility, allowing researchers from all kinds of fields to study it just with a scotch tape and a microscope. Similar to the conductance, the absorption of graphene can also be modulated through electrical gating and chemical functionalization, which can change the carrier population in the band.[62-63]

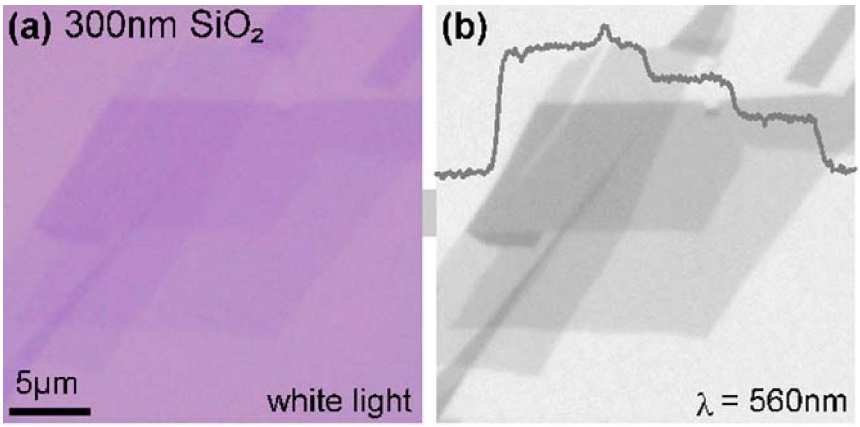

Figure 1.8. Exfoliated graphene crystallites on 300 nm SiO_2 imaged with **a)** white light and **b)** through a 560 nm filter. The scanning trace in **b)** shows stepwise changes in the contrast for 1, 2, and 3 layers. [61] Copyright (2007) AIP Publishing.

Raman spectroscopy of graphene

Graphene has three signature peaks in its Raman spectra—the G, D and 2D bands as shown in Figure 1.9a.[64-65] The G-Peak at near 1580 cm^{-1} is one of the most prominent features in the Raman spectra of graphitic materials. It is a strong indication of the existence of π-π sp^2 carbon network structure in graphene. The D-peak at 1300 to 1400 cm^{-1} is the result of the disorder in sp^2-hybridized carbon lattice. The disorder could come from intrinsic defects in the lattice or covalent functionalization converting sp^2 hybridization to sp^3.

Analyzing the intensity ratio between the D and G bands is a standard method to quantify the graphene sample's quality or functionalization level.[66]

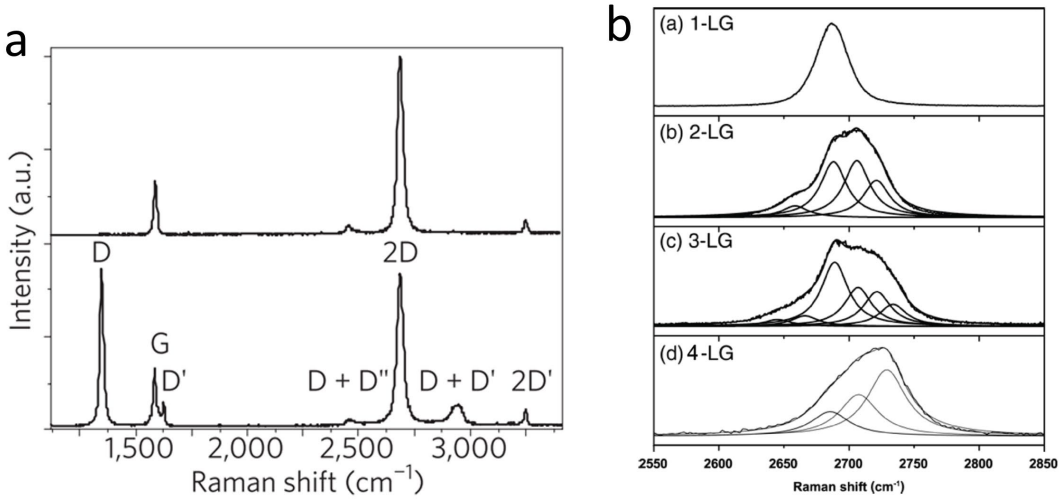

Figure 1.9. a) Raman spectra of pristine (top) and defected (bottom) graphene.[65] Copyright (2013) Springer Nature. **b)** The 2D spectra for graphene as a function of the number of layers.[64] Copyright (2010) American Chemical Society.

The 2D band at 2500-2800 cm^{-1} is the highest peak in the Raman spectra of pristine graphene. It originates from a second order scattering process, that is the overtone of the D band scattering. The 2D band is very sensitive to the layer number of the graphene as shown in Figure 1.9b. With the increase of the layer number, the 2D band change from symmetric (single layer) to dispersive (bilayer to multilayer) and the full width at half maximum of the peak become larger. All three peaks are sensitive to perturbations of graphene lattice. These peaks' positions, intensities, and shapes are tunable by electrical or chemical doping and mechanical strain/stress.[67]

Impermeability of graphene

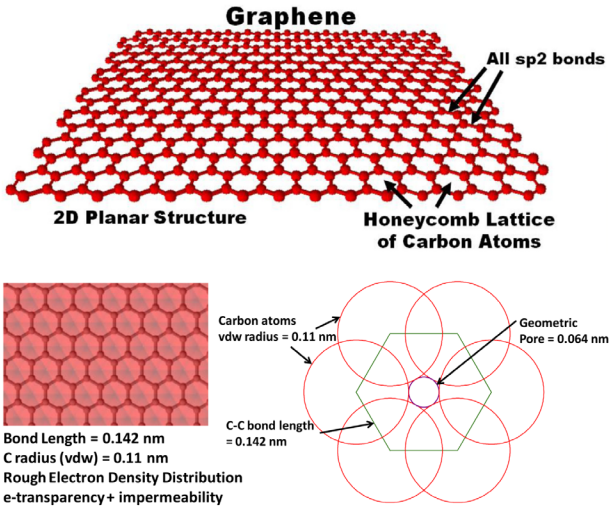

Figure 1.10. Graphene lattice structure: sp^2 hybridized carbon atoms arranged in a 2D honeycomb lattice. (Bottom) the molecular structure with rough electronic density distribution: while graphene is relatively transparent to electrons, it is practically impermeable to all molecules at room temperature. Geometric pore (0.064 nm) is also small enough not to allow molecules to pass through.[68] Copyright (2013) Elsevier.

The lattice of graphene consists of aromatic sp^2 network. The only path for a molecule or atom to pass across the graphene lattice is through the hole of each aromatic ring. With the C-C bond length of 0.142 nm, the pore size of the aromatic ring is 0.246 nm. This pore is already too narrow for particles like helium (0.28 nm) or hydrogen (0.314 nm) to cross. If we add the van der Waals radius of the carbon atom (0.11 nm), as shown in Figure 1.10, the geometric pore size decreases further to 0.064 nm, which is even smaller than the hydrogen atom (0.24 nm).[68] Only fundamental particles like protons (or H^+) and electrons can pass through a perfect graphene lattice.

Many workers have demonstrated the impermeability of graphene and contrive novel applications based on this. Bunch et al. investigated the permeance of several gas molecules

with graphene capped micro-chamber. Even with five atm pressure differences imposed across the graphene, the impermeability still holds for hydrogen and helium gas.[69] Geim et al. have shown that the proton (H^+) is small enough to penetrate the graphene lattice with an applied electrical field.[70] The electrical and optical conductivity and atomic thickness made graphene a perfect protective material for corrosion protection and electron microscopy measurement. Yuk, Park et al. have constructed a TEM-compatible liquid cell by encapsulating micro-liquid bubbles between two graphene layers.[71]

Morphology of graphene

Graphene can come in different forms based on its preparation method. The morphological difference can affect the properties and applications of graphene. Figure 1.11 shows three different types of graphene.[72-74] The tape-exfoliation method can produce high-quality single-crystal graphene on a small scale (<100 μm). Epitaxial growth and chemical vapor deposition (CVD) can usually deliver wafer-size polycrystalline graphene with small grain sizes (1 to 50 μm).[75-76] Recent progress has been made to synthesize monodomain graphene on millimeter-scales through both CVD and epitaxial growth.[77-78] The electrical mobilities of charged carriers are greatly influenced by grain boundaries, which can serve as scattering sites during carrier transport.[79] In devices with the same channel dimension, graphene with larger domain sizes yields higher carrier mobility and conductivity. Exfoliated graphene is usually used in academia as a platform to study electron dynamics, while CVD graphene has been widely applied in high-performance electrical and optical devices.

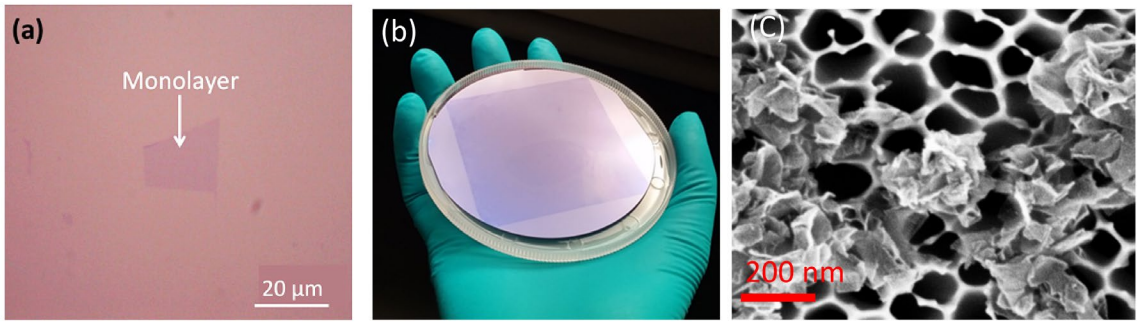

Figure 1.11. Different forms of graphene **a)** exfoliated monolayer graphene[72] (Copyright (2010) American Chemical Society) **b)** CVD monolayer graphene transferred onto a wafer[73] (Copyright (2019) American Chemical Society) **c)** SEM image of graphene nanoplatelets on a filter membrane.[74] Copyright (2016) American Chemical Society.

Graphene in the form of nanoplatelets (GNP) or nanoflakes, like the sample in Figure 1.11c, can be produced from solvent exfoliation of graphite or reducing graphene oxide.[80-81] Due to the nanometer-scale grain size, GNPs sacrifices the high carrier mobility and impermeability of single-layer graphene for superior chemical reactivity, processibility, and scalability. The reactivity of the graphene usually comes from defective sites in the lattice. The graphene edges with dangling bonds are more chemically reactive than the stable sp^2 conjugated network in the middle.[82] Therefore, due to their small size, GNPs can be easily chemically functionalized on their boundaries with high yield. After being functionalized with different groups, GNPs can be suspended in aqueous or organic solvents for solution-based applications, such as conductive ink and paste.[83] The suspension can also be converted into solid films by spray coating, filtration, or merging with other polymers on a large scale for water filtration, electrical/heat-conductive film and catalysts.[74, 84]

1.1.3 Carbon nanotubes

Since their discovery by Sumio Iijima in 1991, carbon nanotubes (CNTs) have been exemplary one-dimensional systems studied by researchers across different fields due to their unique structure and remarkable electrical, optical, and mechanical properties.[85-86] This sub-chapter presents a short introduction about CNTs' structure, properties, morphology, and applications related to my research.

Structure

The carbon nanotube (CNT) is a one-dimensional cylindrical carbon tube with nm-scale diameter. Its structure can be perceived as rolling a hypothetically tailored piece of graphene and then stitching two ends together.[87] The direction we roll this hypothetical graphene ribbon determines the chirality of resulted carbon nanotube.[88] As mentioned in the graphene sub-chapter, the primitive cell of graphene contains two different carbon atoms (A and B). Each type of carbon atom can form a triangular lattice. The rolling direction is defined by the chiral vector $\overrightarrow{C_h} = (n, m)$ connecting two crystallographically equivalent carbon atoms (A_1-A_2 or B_1-B_2) in their own triangle lattice, as shown in the Figure 1.12a. Then two cuts normal to the vector are made at the A_1, A_2 atoms and we can roll this tailored graphene ribbon into a carbon nanotube.

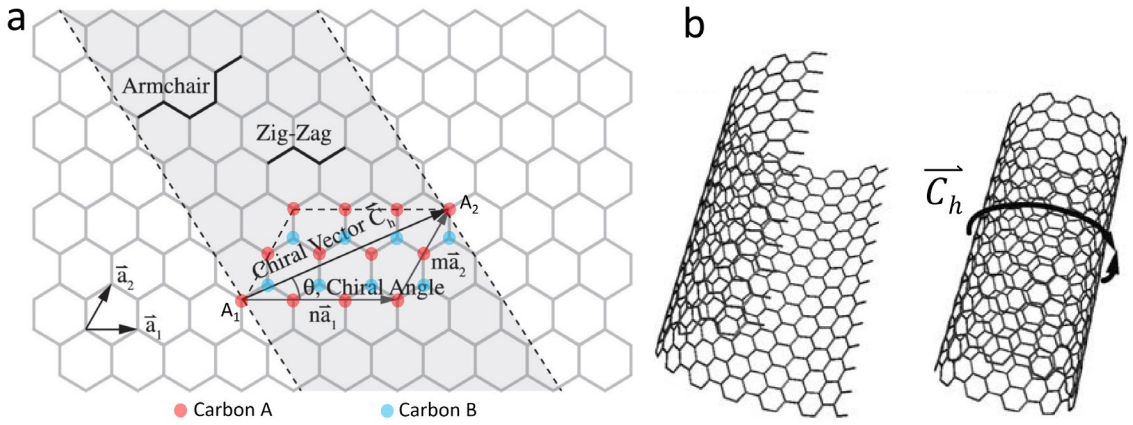

Figure 1.12. Carbon nanotube can be viewed as a graphene cylinder. **a)** schematics of defining the chiral vector of CNT. [89] Copyright (2001) Elsevier. **b)** Imaginative rolling of a graphene ribbon in the direction of chiral vector.[87] Copyright (2006) Springer Nature.

The chirality of CNT is denoted by n, m. The CNT circumference c is determined by the magnitude of the chiral vector (n,m) and can be calculated using the following equation:

$$c = u\sqrt{(n^2 + nm + m^2)} \approx 0.246\sqrt{(n^2 + nm + m^2)} \text{ nanometer}$$

where u is the unit length of the triangular lattice, which is equal to $2\sqrt{3}\, a_{C-C\ length}$.

The diameter d of the CNT is $\frac{c}{\pi}$, that is equal to

$$d \approx 0.0783\sqrt{(n^2 + nm + m^2)} \text{ nanometer}$$

Based on its chiral number (n, m), a CNT can be categorized into three types: armchair (n=m), zigzag (n=0 or m=0) and chiral (n≠m and n, m>0).

Electronic properties

The electronic properties of a CNT are affected by its chiral number. Armchair CNTs are all metallic with a zero bandgap. Zigzag and chiral CNTs are metallic when $\frac{n-m}{3}$ is an integer. Otherwise, they are semiconducting with non-zero bandgaps. The bandgap of

semiconducting CNT is inversely proportional to the vector magnitude of (n, m). A CNT with a larger diameter has a smaller bandgap.[90] The charge carrier density in semiconducting CNT can be modulated through field-effect gating or chemical doping.[91-92] Different dopants can change semiconducting CNTs into either p-type or n-type.[92-93]

Optical properties

The density of states of CNTs consists of multiple sharp van Hove peaks that arise from the one-dimensionality, as shown in Figure 1.13.[94] Strong photon absorption happens at the S_{11}, S_{22}, transitions for semiconducting CNTs, and M_{11} for the metallic CNTs. These inter-band transitions contribute to the signature peaks in CNT absorption spectra in Figure 1.13. Following the absorption process, the excited electron will then go through the internal conversion to the lowest conduction band, and the hole will go up to the highest valence band. In the end, for the semiconducting CNT, the electron and hole will recombine and emit light with bandgap energy. The recombination is a non-radiative process for metallic CNT because electron and hole pair will just meet at Fermi level in the middle through vibrational relaxation. The absorption and emission can both be modulated by chemical doping and electrical gating. The conduction band's filling or the valence band's depletion can both block some inter-band transitions, suppressing peaks in the absorption spectra.[95-96] Absorption and emission spectra both can be used to determine the chirality of CNTs because of the correlation between (n,m) and the bandgap.[97-98]

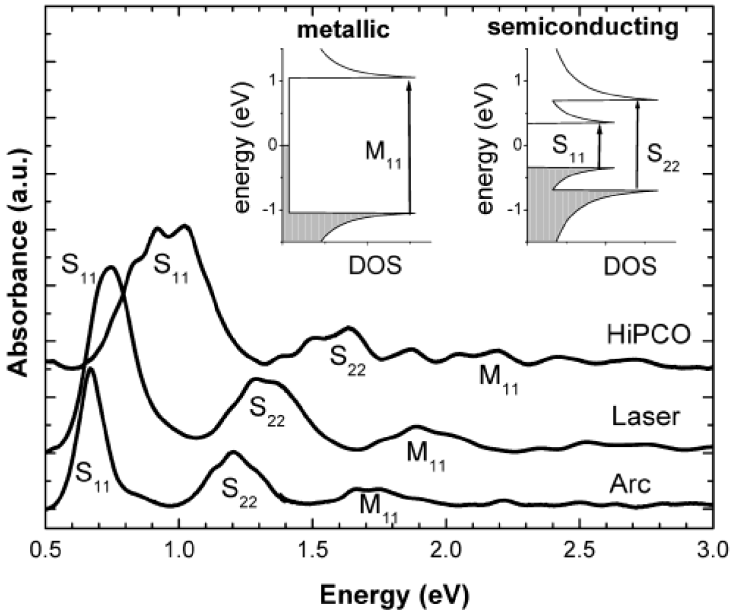

Figure 1.13. Absorption spectra of CNTs from different synthesis methods. Embedded illustrations show the density of states of metallic and semiconducting CNTs and the inter-band transitions during the absorption process.[94] Copyright (2002) American Chemical Society.

Raman spectroscopy of carbon nanotube

CNTs share some of the signature Raman peaks (G, D bands) with graphene as shown in Figure 1.14.[64] However, because the symmetry of each aromatic ring is broken as a consequence of the tube-like structure, the G band splits into two peaks G^+, G^-. Another unique Raman mode of CNT is the radial breathing mode (RBM) in the low-frequency range (<500 cm^{-1}), which arises from the radial expansion and contraction of the whole tube. The RBM is strongly coupled with the radius of CNTs. Its position can provide an estimation of CNTs' diameter *d* by the following equation[64]:

$$d = \frac{234}{\nu RBM(in\ cm^{-1})} \text{ nanometer}$$

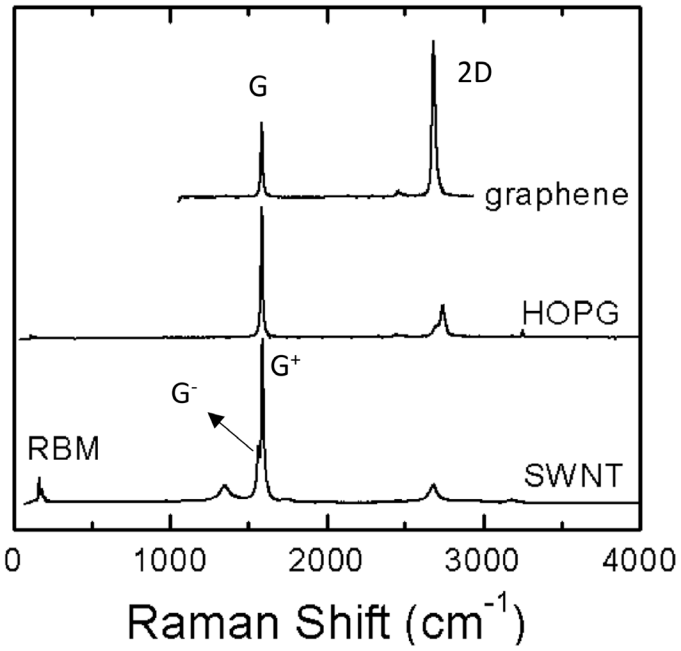

Figure 1.14. Raman spectra from graphene, highly oriented pyrolytic graphite, and single wall carbon nanotube.[64] Copyright (2010) American Chemical Society.

Different forms of carbon nanotubes and their applications

CNT samples can take many forms based on their production methods and applications. Freshly produced CNT forests grown by CVD or the Arc-discharge method can be drawn and spun into yarns for macroscopic applications.[99] Superaligned CNTs inside the yarn grant the fiber remarkable mechanical properties.[100] CNTs can also be dispersed in organic solvent through continuous sonication and in water with the help of surfactants.[101-102] Solution phase CNT samples can be directly used as electrically and thermally conductive ink/paste materials.[103] Separation of metallic and semiconducting CNTs can be done in suspension with the help of special polymer dopants that selectively absorb CNTs with different chirality.[104] The dispersed CNTs in solutions can be prepared as solid thin films by the filtration or spray-coating method.[105-106] CNT thin films can be further patterned by

standard photolithography and O_2 plasma etching.[106-107] High-performance flexible logical circuits completely made of CNTs have been achieved by patterning semiconducting CNT films on a plastic membrane[108-109]. CNT thin films have also been applied in smart optical windows. By electrical gating with ab ionic liquid, the IR absorption of CNT thin films can be modulated effectively.[96, 110-111]

Morphological effect on carbon nanotubes

A CNT is a one-dimensional system with a huge spatial aspect ratio (>1000) between its length and radius. This huge aspect ratio endows CNT with the spatial anisotropic electrical and optical properties. Carriers can transport ballistically inside individual CNT.[91] Through the van der Waals interaction, multiple CNTs can be closely packed into a bundle with a larger diameter and length. However, each bundle usually yields a lower carrier mobility than the individual CNT. The reason for this is the inter-tube junctions break the ballistic transport trend when carriers travel across multiple nanotubes.[106] As mentioned above, CNT thin films with thicknesses from 2 nm to a few microns can be prepared through filtration of CNT dispersion.[112-113] The thickness of CNT film can affect ion diffusion in ionic liquid-gated transistor devices.[96] Thicker CNT films could slow the ion diffusion, prolonging the response time of the devices.

1.2 Overview of the morphological study in this thesis

All three polyaromatic carbon-based materials mentioned above have great properties and valuable applications. Their structures, forms, and morphological effect on materials' properties have also been discussed. It is clear that the versatility in real-world applications depends on the variety of materials' morphology. Therefore, morphology control of materials' shape, surface, and orientation is essential for scientists and engineers to maximize the potential of these conjugated carbon materials.

The next stage in the development of polyaromatic carbon materials will involve the control of their mesoscopic properties and how different polyaromatic materials (PAHs and graphene, for example) interface with each other. The work in this thesis explores different physical and chemical strategies for enhancing the properties of carbon materials, from PAHs to CNTs, by controlling their morphology.

This part of Chapter 1 gives an overview of this thesis' goals and contributions to the morphological study on PAHs, graphene, and CNTs.

1.2.1 Top-down shape engineering of molecular crystals

As mentioned in Chapter 1.1.1, the properties of functional PAH crystals can be tuned by their morphology. Controlling crystals' shapes and dimensions is also necessary to incorporate them into practical devices. There are several levels to morphologically engineer a PAH molecular crystal. First, the PAH molecule itself can be chemically modified with functional groups. The attached groups can affect the intermolecular interaction during the self-assembling crystal growth. The molecular packing and the morphology of resulting crystal can be different from its original form. Second, we can

rely on polymorphism to grow crystals with different shapes and orientations from the same molecules. To selectively grow the desired phase, precise multidimensional control of its growth conditions like temperature, pressure, solvent, and growth templates is required. The third level is to modify the morphology after the crystal growth.

The first two levels require specific experimental explorations for each PAH molecule. The working experimental details, which could be published, are sometimes unreliable for chemists from other labs to reproduce. In many cases, a distribution of crystals with different sizes and shapes will coexist in the final sample. This is not ideal for applying PAH crystals in large-scale practical devices, which require a high production yield. Thus, a generalized way to control the crystal morphology after growth is needed.

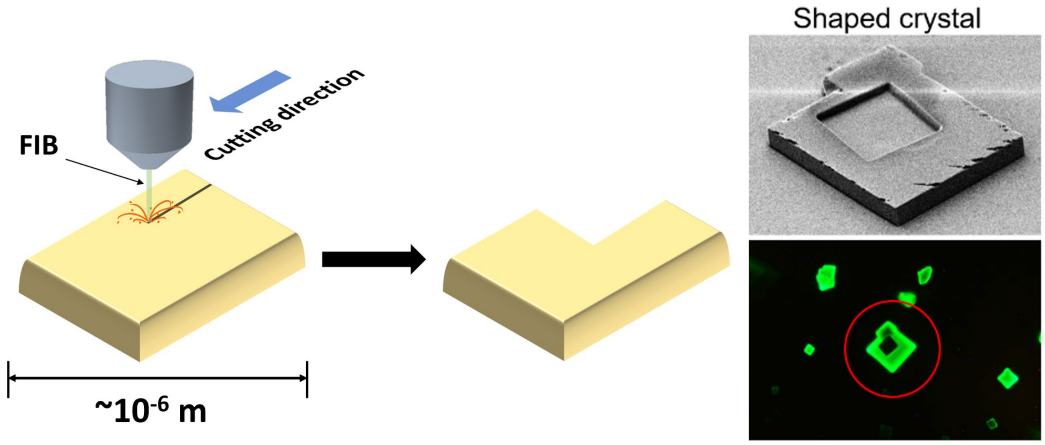

Figure 1.15. An illustration of using FIB milling to shape molecular crystals (left) and the SEM and fluorescence image of a shaped perylene crystal (right).[35] Copyright (2020) American Chemical Society.

In Chapter 3, a special "knife" made with a stream of focused ions is used to cut perylene microcrystals in a top-down fashion, as illustrated in Figure 1.15. Thanks to the ultra-short De Broglie wavelength of the Ga ions, the cutting resolution of the FIB on organics is about

130 nm, which is higher than the best laser cutter in the world. The focused ion beam can be programmed to machine microcrystal into arbitrary shapes with minimum damage. 90% of the photoluminescence is retained after FIB. This proof-of-concept demonstration provides a promising general method to create molecular crystals with user-defined shapes.

1.2.2 Surface passivation of molecular crystals by 2D materials

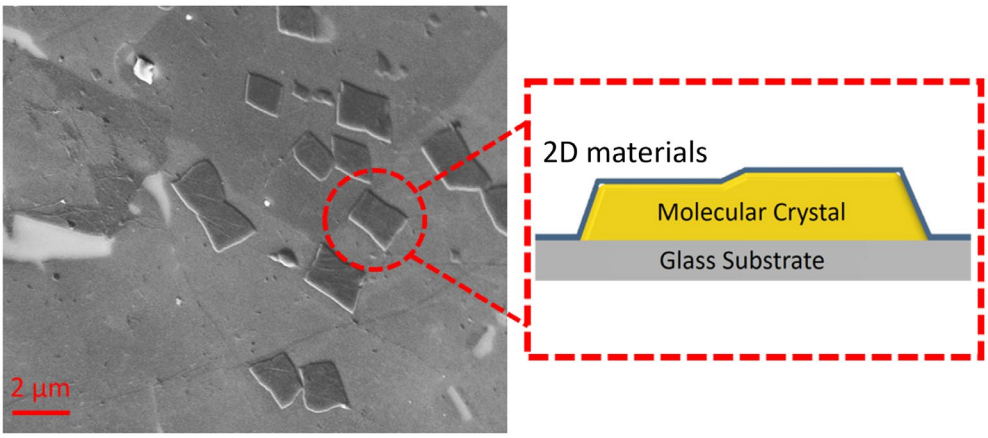

Figure 1.16. The SEM image of graphene encapsulated perylene crystals and the schematic of the sample structure.[114] Copyright (2018) American Chemical Society.

Another challenge hindering the practical application of PAHs in functional devices is that organic crystals are subjected to corrosion from the environment. The electronic properties of PAHs are sensitive to the impurities, such as water or O_2, in the air. Organic crystals also dissolve easily in organic solvent and sublime away in high vacuum or elevated temperatures. Thus, a strategy to protect PAH crystals from their environment is required. Current protection methods include isolating them under vacuum or glovebox and encapsulating them under a thick metal layer or between two glass slides sealed with glues.

However, those methods usually block the close-contact electrical or optical access to the target crystal, limiting its potential applications.

In the Chapter 4, the surface morphology of the crystal is modified by draping another polyaromatic carbon-based material—graphene on top, as shown in Figure 1.16. Despite graphene's atomic thickness, the impermeable membrane successfully protects the organic crystal from solvent dissolution and sublimation at high temperatures while still maintaining its optical access. The effect of graphene on PAH excimer dynamics is measured by photoluminescence (PL) decay. As a zero-bandgap semiconductor, graphene can quench PL from PAH through Förster resonance energy transfer. From the results, the graphene has no detectable quenching effect on bulk crystals because crystals have a much larger thickness (~150 nm) compared to the graphene quenching radius (<20 nm) estimated from the fitting. The majority of the crystal does not even feel the existence of graphene at the interface.

In the Chapter 5, the quenching effect of graphene is further evaluated by interfacing it with fluorescent dye-doped polymer films with a series of thicknesses. PL decay measurements are done on these samples. From the fitting, the quenching radius of graphene is found to be about 14.6 nm. So even if the quenching effect is not detected on the bulk crystal/graphene sample, the energy transfer is still happening at the interface. Therefore, to further eliminate the quenching effect, graphene is replaced with a few-layer hexagonal boron nitride (h-BN) as the encapsulating blanket. h-BN is a wide-bandgap insulator with a bandgap of about 6 eV. Similar to graphene, few-layer h-BN successfully protects PAH crystals from solvent and high temperature. The surprising result is that wet-

transferred hBN is not photophysically inert but instead has an effective quenching radius of 2.9 nm. This quenching effect can be avoided by using the dry-transfer method. h-BN's final quality as an inert protection layer is determined by its sample preparation conditions.

1.2.3 Carbon nanotube alignment and surface functionalization

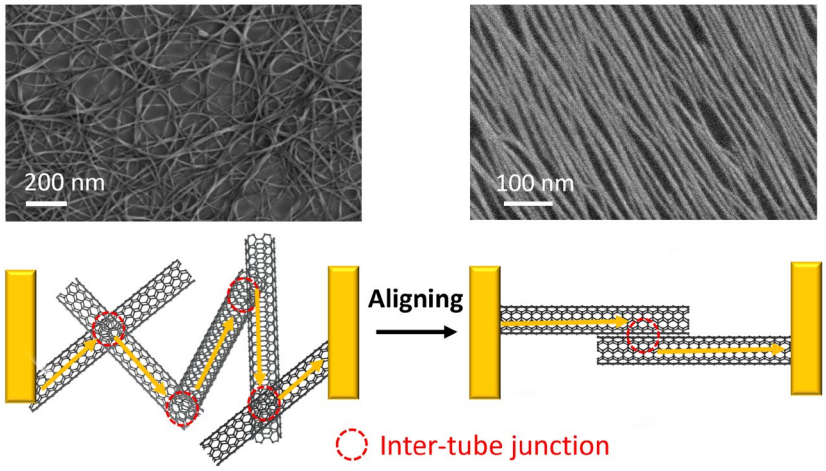

Figure 1.17 The number of inter-tube junctions in a given channel can be reduced by aligning carbon nanotubes in the current direction.[115-116] Copyright (2014) (2019) American Chemical Society.

Individual single-walled carbon nanotubes have excellent electronic properties thanks to their high carrier mobility. They can be dispersed into a homogenous suspension by sonication. The suspension can be filtered, forming solid-state CNT thin films. Compared to individual nanotubes, CNT thin films have superior scalability and processibilities but degraded conductivity and carrier mobilities. The reason for that is the inter-tube junctions process much higher resistance that slows down the carrier transport.

In Chapter 5, two methods are applied to address this problem. First, the morphology of thin film is modified from random networks to aligned arrays, as shown in the top part of Figure 1.17. The speed-controlled filtration process allows the CNTs to be self-assembled

into aligned thin films. The prepared aligned CNT films have large spatial anisotropy in their optical and electrical properties. Carriers that flow parallel to the alignment direction encounter fewer inter-tube junctions in a given channel than carriers that travel in the transverse direction or across random networks, as illustrated in the bottom part of Figure 1.17.

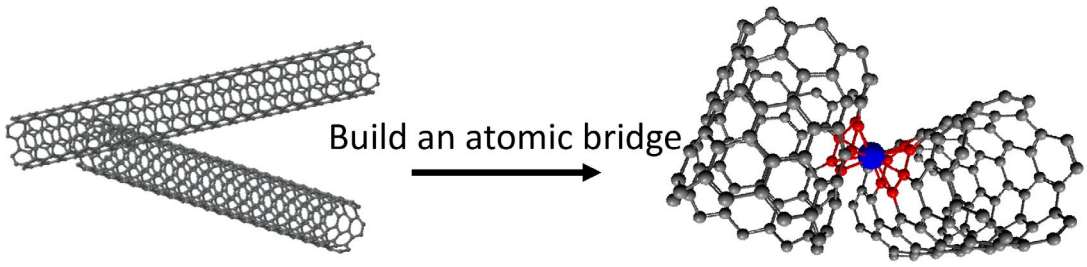

Figure 1.18 Schematic of chromium functionalization that creates a conductive bridge at the inter-tube junction.[117] Copyright (2013) American Chemical Society.

The junction resistance can be further reduced by organometallic photochemistry that inserts chromium atoms between CNTs, as shown in Figure 1.18. The Cr atoms can serve as electrical channels junctions for carrier transport. The functionalization drastically increases the film conductance in the transverse direction, while it has a much smaller effect on the conductivity in the parallel direction. Finally, a reversible switch is fabricated to demonstrate the reversibility of this functionalization. The device current can be turned up by the Cr photochemistry and turned down using ionic liquid gating that breaks the Cr linkage to the CNTs.

The results in this thesis present new ways to control the morphology and interfaces of polyaromatic carbon-based materials. Hopefully, they will help bring about the era of carbon-based electronics.

References

1. Reese, C.; Bao, Z., Organic single-crystal field-effect transistors. *Materials Today* **2007,** *10* (3), 20-27.

2. Avouris, P.; Chen, Z.; Perebeinos, V., Carbon-based electronics. *Nanoscience and Technology: A Collection of Reviews from Nature Journals* **2010**, 174-184.

3. Avouris, P.; Freitag, M.; Perebeinos, V., Carbon-nanotube photonics and optoelectronics. *Nature Photonics* **2008,** *2* (6), 341-350.

4. Briseno, A. L.; Mannsfeld, S. C. B.; Ling, M. M.; Liu, S.; Tseng, R. J.; Reese, C.; Roberts, M. E.; Yang, Y.; Wudl, F.; Bao, Z., Patterning organic single-crystal transistor arrays. *Nature* **2006,** *444*, 913-917.

5. Wu, J.; Gherghel, L.; Watson, M. D.; Li, J.; Wang, Z.; Simpson, C. D.; Kolb, U.; Müllen, K., From branched polyphenylenes to graphite ribbons. *Macromolecules* **2003,** *36* (19), 7082-7089.

6. Scott, L. T.; Jackson, E. A.; Zhang, Q.; Steinberg, B. D.; Bancu, M.; Li, B., A short, rigid, structurally pure carbon nanotube by stepwise chemical synthesis. *Journal of the American Chemical Society* **2012,** *134* (1), 107-110.

7. Bardeen, C. J., Excitonic processes in molecular crystalline materials. *MRS Bulletin* **2013,** *38* (1), 65-71.

8. Léger, A.; d'Hendecourt, L.; Boccara, N., *Polycyclic aromatic hydrocarbons and astrophysics*. Springer Science & Business Media: 2012; Vol. 191.

9. Donaldson, D.; Robertson, J. M., The crystal and molecular structure of ovalene a quantitative X-ray investigation. *Proceedings of the Royal Society of London. Series A. Mathematical and Physical Sciences* **1953,** *220* (1141), 157-170.

10. Lawton, R. G.; Barth, W. E., Synthesis of corannulene. *Journal of the American Chemical Society* **1971,** *93* (7), 1730-1745.

11. Malloci, G.; Cappellini, G.; Mulas, G.; Mattoni, A., Electronic and optical properties of families of polycyclic aromatic hydrocarbons: A systematic (time-dependent) density functional theory study. *Chemical Physics* **2011,** *384* (1-3), 19-27.

12. Ruiz-Morales, Y., HOMO− LUMO gap as an index of molecular size and structure for polycyclic aromatic hydrocarbons (PAHs) and asphaltenes: A theoretical study. I. *Journal of Physical Chemistry A* **2002,** *106* (46), 11283-11308.

13. Novoselov, K. S.; Geim, A. K.; Morozov, S. V.; Jiang, D.; Katsnelson, M. I.; Grigorieva, I.; Dubonos, S.; Firsov; AA, Two-dimensional gas of massless Dirac fermions in graphene. *Nature* **2005,** *438* (7065), 197-200.

14. Bredas, J.-L., Mind the gap! *Materials Horizons* **2014,** *1* (1), 17-19.

15. Sugioka, M., The Relationship Between UV-VIS Absorption and Structure of Organic Compounds. *UV Talk Letter February. Shimadzu* **2009,** *2*, 5-6.

16. Burdett, J. J.; Müller, A. M.; Gosztola, D.; Bardeen, C. J., Excited state dynamics in solid and monomeric tetracene: The roles of superradiance and exciton fission. *Journal of Chemical Physics* **2010,** *133* (14), 144506.

17. Pookpanratana, S. J.; Goetz, K. P.; Bittle, E. G.; Haneef, H.; Youa, L.; Hackera, C. A.; Robeye, S. W.; Jurchescu, O. D.; Ovsyannikov, R.; Giangrisostomi, E., Electronic Properties and Structure of Single Crystal Perylene. *Organic Electronics* **2018,** *61*, 157-163.

18. Soos, Z. G., Theory of π-molecular charge-transfer crystals. *Annual Review of Physical Chemistry* **1974,** *25* (1), 121-153.

19. Haddon, R. C., Design of organic metals and superconductors. *Nature* **1975,** *256* (5516), 394-396.

20. Kortan, A., Superconductivity at 18 K in potassium-doped C60. *Nature* **1991,** *350*.

21. Haddon, R.; Hebard, A.; Rosseinsky, M.; Murphy, D.; Duclos, S.; Lyons, K.; Miller, B.; Rosamilia, J.; Fleming, R.; Kortan, A., Conducting films of C 60 and C 70 by alkali-metal doping. *Nature* **1991,** *350* (6316), 320-322.

22. Wang, X.; Liu, R.; Gui, Z.; Xie, Y.; Yan, Y.; Ying, J.; Luo, X.; Chen, X., Superconductivity at 5 K in alkali-metal-doped phenanthrene. *Nature Communications* **2011,** *2* (1), 1-7.

23. Xue, M.; Cao, T.; Wang, D.; Wu, Y.; Yang, H.; Dong, X.; He, J.; Li, F.; Chen, G., Superconductivity above 30 K in alkali-metal-doped hydrocarbon. *Scientific Reports* **2012,** *2* (1), 1-4.

24. Lichtman, J. W.; Conchello, J.-A., Fluorescence microscopy. *Nature Methods* **2005,** *2* (12), 910-919.

25. Kasha, M., Characterization of electronic transitions in complex molecules. *Discussions of the Faraday Society* **1950,** *9*, 14-19.

26. Easley, C. J.; Mettry, M.; Moses, E. M.; Hooley, R. J.; Bardeen, C. J., Boosting the heavy atom effect by cavitand encapsulation: room temperature phosphorescence of pyrene in the presence of oxygen. *Journal of Physical Chemistry A* **2018,** *122* (32), 6578-6584.

27. Thorsmølle, V. K.; Averitt, R. D.; Demsar, J.; Smith, D.; Tretiak, S.; Martin, R.; Chi, X.; Crone, B.; Ramirez, A.; Taylor, A., Morphology effectively controls singlet-triplet exciton relaxation and charge transport in organic semiconductors. *Physical Review Letters* **2009,** *102* (1), 017401.

28. Singh-Rachford, T. N.; Castellano, F. N., Photon upconversion based on sensitized triplet–triplet annihilation. *Coordination Chemistry Reviews* **2010,** *254* (21-22), 2560-2573.

29. Jones, G. A.; Bradshaw, D. S., Resonance energy transfer: from fundamental theory to recent applications. *Frontiers in Physics* **2019,** *7*, 100.

30. Gadella, T. W., *FRET and FLIM techniques*. Elsevier: 2011.

31. Swathi, R. S.; Sebastian, K. L., Long Range Resonance Energy Transfer from a Dye Molecule to Graphene has (Distance)$^{-4}$ Dependence. *Journal of Chemical Physics* **2009,** *130*, 086101/1-3.

32. Liu, Y.-X.; Summers, M. A.; Scully, S. R.; McGehee, M. D., Resonance energy transfer from organic chromophores to fullerene molecules. *Journal of Applied Physics* **2006,** *99* (9), 093521.

33. Dexter, D. L., A theory of sensitized luminescence in solids. *Journal of Chemical Physics* **1953,** *21* (5), 836-850.

34. Adronov, A.; Fréchet, J. M., Light-harvesting dendrimers. *Chemical Communications* **2000,** (18), 1701-1710.

35. Li, W.; van Baren, J.; Berges, A.; Bekyarova, E.; Lui, C. H.; Bardeen, C. J., Shaping Organic Microcrystals Using Focused Ion Beam Milling. *Crystal Growth & Design* **2020,** *20* (3), 1583-1589.

36. Ito, F.; Kogasaka, Y.; Yamamoto, K., Fluorescence spectral changes of perylene in polymer matrices during the solvent evaporation process. *Journal of Physical Chemistry B* **2013,** *117* (13), 3675-3681.

37. Solomon, E. B.; Matthews, K. R., Use of fluorescent microspheres as a tool to investigate bacterial interactions with growing plants. *Journal of Food Protection* **2005,** *68* (4), 870-873.

38. FluoSpheres, C.-M., *Working With FluoSpheres® Fluorescent Microspheres.*

39. Cerdán, L.; Costela, A.; Durán-Sampedro, G.; García-Moreno, I.; Calle, M.; Juan-y-Seva, M.; de Abajo, J.; Turnbull, G. A., New perylene-doped polymeric thin films for efficient and long-lasting lasers. *Journal of Materials Chemistry* **2012,** *22* (18), 8938-8947.

40. Sato, K.; Katoh, R., Fluorescence properties of β-perylene crystals prepared by a physical vapor transport method under atmospheric pressure. *Chemical Physics Letters* **2019,** *730*, 312-315.

41. Pick, A.; Klues, M.; Rinn, A.; Harms, K.; Chatterjee, S.; Witte, G., Polymorph-Selective Preparation and Structural Characterization of Perylene Single Crystals. *Crystal Growth & Design* **2015,** *15*, 5495-5504.

42. Cruz, C. D.; Chronister, E. L.; Bardeen, C. J., Using temperature dependent fluorescence to evaluate singlet fission pathways in tetracene single crystals. *Journal of Chemical Physics* **2020,** *153* (23), 234504.

43. Costa, J. C.; Rocha, R. M.; Vaz, I. s. C.; Torres, M. C.; Mendes, A.; Santos, L. M., Description and test of a new multilayer thin film vapor deposition apparatus for organic semiconductor materials. *Journal of Chemical & Engineering Data* **2015,** *60* (12), 3776-3791.

44. Einzinger, M.; Wu, T.; Kompalla, J. F.; Smith, H. L.; Perkinson, C. F.; Nienhaus, L.; Wieghold, S.; Congreve, D. N.; Kahn, A.; Bawendi, M. G., Sensitization of silicon by singlet exciton fission in tetracene. *Nature* **2019,** *571* (7763), 90-94.

45. Caira, M. R., Crystalline polymorphism of organic compounds. *Design of Organic Solids* **1998**, 163-208.

46. Yago, T.; Tamaki, Y.; Furube, A.; Katoh, R., Growth of β-perylene crystal. *Chemistry Letters* **2007,** *36* (3), 370-371.

47. Datta, A.; Mohakud, S.; Pati, S. K., Comparing the electron and hole mobilities in the α and β phases of perylene: role of π-stacking. *Journal of Materials Chemistry* **2007,** *17* (19), 1933-1938.

48. Tong, F.; Bardeen, C. J.; Al-Kaysi, R. O., Photomechanical Crystals Made from Anthracene Derivatives. *Mechanically Responsive Materials for Soft Robotics* **2020**, 29-56.

49. Steudel, S.; Myny, K.; De Vusser, S.; Genoe, J.; Heremans, P., Patterning of organic thin film transistors by oxygen plasma etch. *Applied Physics Letters* **2006,** *89* (18), 183503.

50. Blaszczyk-Lezak, I.; Aparicio, F. J.; Borras, A.; Barranco, A.; Alvarez-Herrero, A.; Fernandez-Rodriguez, M.; Gonzalez-Elipe, A., Optically active luminescent perylene thin

films deposited by plasma polymerization. *Journal of Physical Chemistry C* **2009,** *113* (1), 431-438.

51. Castro Neto, A. H.; Guinea, F.; Peres, N. M. R.; Novoselov, K. S.; Geim, A. K., The electronic properties of graphene. *Reviews of Modern Physics* **2009,** *81* (1), 109-162.

52. Novoselov, K. S.; Fal'ko, V. I.; Colombo, L.; Gellert, P. R.; Schwab, M. G.; Kim, K., A Roadmap for Graphene. *Nature* **2012,** *490*, 192-200.

53. Zhang, Y.; Brar, V. W.; Wang, F.; Girit, C.; Yayon, Y.; Panlasigui, M.; Zettl, A.; Crommie, M. F., Giant phonon-induced conductance in scanning tunnelling spectroscopy of gate-tunable graphene. *Nature Physics* **2008,** *4* (8), 627-630.

54. Chen, J.-H.; Jang, C.; Xiao, S.; Ishigami, M.; Fuhrer, M. S., Intrinsic and extrinsic performance limits of graphene devices on SiO 2. *Nature Nanotechnology* **2008,** *3* (4), 206-209.

55. Novoselov, K. S.; Geim, A. K.; Morozov, S. V.; Jiang, D.-e.; Zhang, Y.; Dubonos, S. V.; Grigorieva, I. V.; Firsov, A. A., Electric field effect in atomically thin carbon films. *Science* **2004,** *306* (5696), 666-669.

56. Elias, D. C.; Nair, R. R.; Mohiuddin, T.; Morozov, S.; Blake, P.; Halsall, M.; Ferrari, A. C.; Boukhvalov, D.; Katsnelson, M.; Geim, A., Control of graphene's properties by reversible hydrogenation: evidence for graphane. *Science* **2009,** *323* (5914), 610-613.

57. Han, M. Y.; Özyilmaz, B.; Zhang, Y.; Kim, P., Energy band-gap engineering of graphene nanoribbons. *Physical Review Letters* **2007,** *98* (20), 206805.

58. Cao, Y.; Fatemi, V.; Fang, S.; Watanabe, K.; Taniguchi, T.; Kaxiras, E.; Jarillo-Herrero, P., Unconventional superconductivity in magic-angle graphene superlattices. *Nature* **2018,** *556* (7699), 43-50.

59. Cao, Y.; Fatemi, V.; Demir, A.; Fang, S.; Tomarken, S. L.; Luo, J. Y.; Sanchez-Yamagishi, J. D.; Watanabe, K.; Taniguchi, T.; Kaxiras, E., Correlated insulator behaviour at half-filling in magic-angle graphene superlattices. *Nature* **2018,** *556* (7699), 80-84.

60. Falkovsky, L. In Optical properties of graphene, *Journal of Physics: conference series*, IOP Publishing: 2008; p 012004.

61. Blake, P.; Hill, E.; Castro Neto, A.; Novoselov, K.; Jiang, D.; Yang, R.; Booth, T.; Geim, A., Making graphene visible. *Applied Physics Letters* **2007,** *91* (6), 063124.

62. Li, Z.; Henriksen, E. A.; Jiang, Z.; Hao, Z.; Martin, M. C.; Kim, P.; Stormer, H. L.; Basov, D. N., Dirac charge dynamics in graphene by infrared spectroscopy. *Nature Physics* **2008,** *4* (7), 532-535.

63. Liu, H.; Liu, Y.; Zhu, D., Chemical doping of graphene. *Journal of Materials Chemistry* **2011,** *21* (10), 3335-3345.

64. Dresselhaus, M. S.; Jorio, A.; Hofmann, M.; Dresselhaus, G.; Saito, R., Perspectives on carbon nanotubes and graphene Raman spectroscopy. *Nano Letters* **2010,** *10* (3), 751-758.

65. Ferrari, A. C.; Basko, D. M., Raman spectroscopy as a versatile tool for studying the properties of graphene. *Nature Nanotechnology* **2013,** *8* (4), 235-246.

66. Cançado, L. G.; Jorio, A.; Ferreira, E. M.; Stavale, F.; Achete, C. A.; Capaz, R. B.; Moutinho, M. V. d. O.; Lombardo, A.; Kulmala, T.; Ferrari, A. C., Quantifying defects in graphene via Raman spectroscopy at different excitation energies. *Nano Letters* **2011,** *11* (8), 3190-3196.

67. Huang, M.; Yan, H.; Chen, C.; Song, D.; Heinz, T. F.; Hone, J., Phonon Softening and Crystallographic Orientation of Strained Graphene Studied by Raman Spectroscopy. *Proceedings of the National Academy of Sciences* **2009,** *106*, 7304-7308.

68. Berry, V., Impermeability of graphene and its applications. *Carbon* **2013,** *62*, 1-10.

69. Bunch, J. S.; Verbridge, S. S.; Alden, J. S.; Zande, A. M. v. d.; Parpia, J. M.; Craighead, H. G.; McEuen, P. L., Impermeable Atomic Membranes from Graphene Sheets. *Nano Letters* **2008,** *8*, 2458-2462.

70. Hu, S.; Lozada-Hidalgo, M.; Wang, F.; Mishchenko, A.; Schedin, F.; Nair, R. R.; Hill, E.; Boukhvalov, D.; Katsnelson, M.; Dryfe, R. A., Proton transport through one-atom-thick crystals. *Nature* **2014,** *516* (7530), 227-230.

71. Yuk, J. M.; Park, J.; Ercius, P.; Kim, K.; Hellebusch, D. J.; Crommie, M. F.; Lee, J. Y.; Zettl, A.; Alivisatos, A. P., High-resolution EM of colloidal nanocrystal growth using graphene liquid cells. *Science* **2012,** *336* (6077), 61-64.

72. Huang, Y.; Sutter, E.; Shi, N. N.; Zheng, J.; Yang, T.; Englund, D.; Gao, H.-J.; Sutter, P., Reliable exfoliation of large-area high-quality flakes of graphene and other two-dimensional materials. *ACS Nano* **2015,** *9* (11), 10612-10620.

73. Shivayogimath, A.; Whelan, P. R.; Mackenzie, D. M.; Luo, B.; Huang, D.; Luo, D.; Wang, M.; Gammelgaard, L.; Shi, H.; Ruoff, R. S., Do-it-yourself transfer of large-area graphene using an office laminator and water. *Chemistry of Materials* **2019,** *31* (7), 2328-2336.

74. Chen, M.; Tian, X.; Li, W.; Bekyarova, E.; Li, G.; Moser, M.; Haddon, R. C., Application of organometallic chemistry to the electrical interconnection of graphene nanoplatelets. *Chemistry of Materials* **2016,** *28* (7), 2260-2266.

75. Emtsev, K. V.; Bostwick, A.; Horn, K.; Jobst, J.; Kellogg, G. L.; Ley, L.; McChesney, J. L.; Ohta, T.; Reshanov, S. A.; Röhrl, J., Towards wafer-size graphene layers by atmospheric pressure graphitization of silicon carbide. *Nature Materials* **2009,** *8* (3), 203-207.

76. Reina, A.; Jia, X.; Ho, J.; Nezich, D.; Son, H.; Bulovic, V.; Dresselhaus, M. S.; Kong, J., Large area, few-layer graphene films on arbitrary substrates by chemical vapor deposition. *Nano Letters* **2009,** *9* (1), 30-35.

77. Wu, Y. A.; Fan, Y.; Speller, S.; Creeth, G. L.; Sadowski, J. T.; He, K.; Robertson, A. W.; Allen, C. S.; Warner, J. H., Large single crystals of graphene on melted copper using chemical vapor deposition. *ACS Nano* **2012,** *6* (6), 5010-5017.

78. Xu, X.; Zhang, Z.; Dong, J.; Yi, D.; Niu, J.; Wu, M.; Lin, L.; Yin, R.; Li, M.; Zhou, J., Ultrafast epitaxial growth of metre-sized single-crystal graphene on industrial Cu foil. *Science Bulletin* **2017,** *62* (15), 1074-1080.

79. Song, H.; Li, S.; Miyazaki, H.; Sato, S.; Hayashi, K.; Yamada, A.; Yokoyama, N.; Tsukagoshi, K., Origin of the relatively low transport mobility of graphene grown through chemical vapor deposition. *Scientific Reports* **2012,** *2* (1), 1-6.

80. Compton, O. C.; Nguyen, S. T., Graphene oxide, highly reduced graphene oxide, and graphene: versatile building blocks for carbon-based materials. *Small* **2010,** *6* (6), 711-723.

81. Khan, U.; O'Neill, A.; Lotya, M.; De, S.; Coleman, J. N., High-concentration solvent exfoliation of graphene. *Small* **2010,** *6* (7), 864-871.

82. Denis, P. A.; Iribarne, F., Comparative study of defect reactivity in graphene. *Journal of Physical Chemistry C* **2013,** *117* (37), 19048-19055.

83. Arapov, K.; Rubingh, E.; Abbel, R.; Laven, J.; de With, G.; Friedrich, H., Conductive screen printing inks by gelation of graphene dispersions. *Advanced Functional Materials* **2016,** *26* (4), 586-593.

84. Jia, Y.; Zhang, L.; Du, A.; Gao, G.; Chen, J.; Yan, X.; Brown, C. L.; Yao, X., Defect graphene as a trifunctional catalyst for electrochemical reactions. *Advanced Materials* **2016,** *28* (43), 9532-9538.

85. Iijima, S., Helical microtubules of graphitic carbon. *Nature* **1991,** *354* (6348), 56-58.

86. Iijima, S.; Ichihashi, T., Single-shell carbon nanotubes of 1-nm diameter. *Nature* **1993,** *363* (6430), 603-605.

87. Thomsen, C.; Reich, S., Raman scattering in carbon nanotubes. *Light Scattering in Solid IX* **2006**, 115-234.

88. Rafiee, R.; Pourazizi, R., Evaluating the influence of defects on the young's modulus of carbon nanotubes using stochastic modeling. *Materials Research* **2014,** *17*, 758-766.

89. Thostenson, E. T.; Ren, Z.; Chou, T.-W., Advances in the science and technology of carbon nanotubes and their composites: a review. *Composites science and technology* **2001,** *61* (13), 1899-1912.

90. Dresselhaus, M. S.; Dresselhaus, G.; Eklund, P. C., *Science of fullerenes and carbon nanotubes: their properties and applications*. Elsevier: 1996.

91. Javey, A.; Guo, J.; Wang, Q.; Lundstrom, M.; Dai, H., Ballistic carbon nanotube field-effect transistors. *Nature* **2003,** *424* (6949), 654-657.

92. Javey, A.; Tu, R.; Farmer, D. B.; Guo, J.; Gordon, R. G.; Dai, H., High performance n-type carbon nanotube field-effect transistors with chemically doped contacts. *Nano Letters* **2005,** *5* (2), 345-348.

93. Kang, D.; Park, N.; Ko, J.-h.; Bae, E.; Park, W., Oxygen-induced p-type doping of a long individual single-walled carbon nanotube. *Nanotechnology* **2005,** *16* (8), 1048.

94. Niyogi, S.; Hamon, M. A.; Hu, H.; Zhao, B.; Bhowmik, P.; Sen, R.; Itkis, M. E.; Haddon, R. C., Chemistry of Single-Walled Carbon Nanotubes. *Accounts of Chemical Research* **2002,** *35*, 1105-1113.

95. Shimotani, H.; Tsuda, S.; Yuan, H.; Yomogida, Y.; Moriya, R.; Takenobu, T.; Yanagi, K.; Iwasa, Y., Continuous Band-Filling Control and One-Dimensional Transport in Metallic and Semiconducting Carbon Nanotube Tangled Films. *Advanced Functional Materials* **2014,** *24*, 3305-3311.

96. Stekovic, D.; Arkook, B.; Li, G.; Li, W.; Bekyarova, E.; Itkis, M. E., High modulation speed, depth, and coloration efficiency of carbon nanotube thin film electrochromic device achieved by counter electrode impedance matching. *Advanced Materials Interfaces* **2018,** *5* (20), 1800861.

97. Liu, H. P.; Nishide, D.; Tanaka, T.; Kataura, H., Large-scale Single-chirality Separation of Single-wall Carbon Nanotubes by Simple Gel Chromatography. *Nature Communications* **2011,** *2*, 309(8).

98. Liu, H.; Tanaka, T.; Urabe, Y.; Kataura, H., High-efficiency single-chirality separation of carbon nanotubes using temperature-controlled gel chromatography. *Nano Letters* **2013,** *13* (5), 1996-2003.

99. Jiang, K.; Li, Q.; Fan, S., Spinning continuous carbon nanotube yarns. *Nature* **2002,** *419* (6909), 801-801.

100. Baughman, R. H.; Zakhidov, A. A.; de Heer, W. A., Carbon nanotubes - the Route Toward Applications. *Science* **2002,** *297* (5582), 787-792.

101. Chen, J.; Hamon, M. A.; Hu, H.; Chen, Y.; Rao, A. M.; Eklund, P. C.; Haddon, R. C., Solution properties of single-walled carbon nanotubes. *Science* **1998,** *282* (5386), 95-98.

102. Rastogi, R.; Kaushal, R.; Tripathi, S.; Sharma, A. L.; Kaur, I.; Bharadwaj, L. M., Comparative study of carbon nanotube dispersion using surfactants. *Journal of Colloid and Interface Science* **2008,** *328* (2), 421-428.

103. Tortorich, R. P.; Choi, J.-W., Inkjet printing of carbon nanotubes. *Nanomaterials* **2013,** *3* (3), 453-468.

104. Tu, X.; Zheng, M., A DNA-based approach to the carbon nanotube sorting problem. *Nano Research* **2008,** *1* (3), 185-194.

105. Bekyarova, E.; Itkis, M. E.; Cabrera, N.; Zhao, B.; Yu, A.; Gao, J.; Haddon, R. C., Electronic Properties of Single-Walled Carbon Nanotube Networks. *Journal of the American Chemical Society* **2005,** *127*, 5990-5995.

106. Hu, L.; Hecht, D. S.; Grüner, G., Carbon Nanotube Thin Films: Fabrication, Properties, and Applications. *Chemical Reviews* **2010,** *110* (10), 5790-5844.

107. Engel, M.; Small, J. P.; Steiner, M.; Freitag, M.; Green, A. A.; Hersam, M. C.; Avouris, P., Thin Film Nanotube Transistors Based on Self-Assembled, Aligned, Semiconducting Carbon Nanotube Arrays. *ACS Nano* **2008,** *2*, 2445-2452.

108. Cao, Q.; Kim, H.-s.; Pimparkar, N.; Kulkarni, J. P.; Wang, C.; Shim, M.; Roy, K.; Alam, M. A.; Rogers, J. A., Medium-scale carbon nanotube thin-film integrated circuits on flexible plastic substrates. *Nature* **2008,** *454* (7203), 495-500.

109. Wang, S.; Xu, J.; Wang, W.; Wang, G.-J. N.; Rastak, R.; Molina-Lopez, F.; Chung, J. W.; Niu, S.; Feig, V. R.; Lopez, J., Skin electronics from scalable fabrication of an intrinsically stretchable transistor array. *Nature* **2018,** *555* (7694), 83-88.

110. Wang, F.; Itkis, M. E.; Bekyarova, E.; Haddon, R. C., Charge-compensated, semiconducting single-walled carbon nanotube thin film as an electrically configurable optical medium. *Nature Photonics* **2013,** *7* (6), 459-465.

111. Liu, L.; Han, J.; Xu, L.; Zhou, J.; Zhao, C.; Ding, S.; Shi, H.; Xiao, M.; Ding, L.; Ma, Z., Aligned, high-density semiconducting carbon nanotube arrays for high-performance electronics. *Science* **2020,** *368* (6493), 850-856.

112. Timmermans, M. Y.; Estrada, D.; Nasibulin, A. G.; Wood, J. D.; Behnam, A.; Sun, D.-m.; Ohno, Y.; Lyding, J. W.; Hassanien, A.; Pop, E., Effect of carbon nanotube network morphology on thin film transistor performance. *Nano Research* **2012,** *5* (5), 307-319.

113. He, X. W.; Gao, W. L.; Xie, L. J.; Li, B.; Zhang, Q.; Lei, S. D.; Robinson, J. M.; Haroz, E. H.; Doorn, S. K.; Wang, W. P.; Vajtai, R.; Ajayan, P. M.; Adams, W. W.; Hauge, R. H.; Kono, J., Wafer-scale Monodomain Films of Spontaneously Aligned Single-walled Carbon Nanotubes. *Nature Nanotechnology* **2016,** *11* (7), 633-638.

114. Li, W.; Tierce, N. T.; Bekyarova, E.; Bardeen, C. J., Protection of Molecular Microcrystals by Encapsulation under Single-Layer Graphene. *ACS Omega* **2018,** *3*, 8129-8134.

115. Tian, X.; Moser, M. L.; Pekker, A.; Sarkar, S.; Ramirez, J.; Bekyarova, E.; Itkis, M. E.; Haddon, R. C., Effect of Atomic Interconnects on Percolation in Single-Walled Carbon Nanotube Thin Film Networks. *Nano Letters* **2014,** *14*, 3930-3937.

116. Chen, M.; Li, W.; Kumar, A.; Li, G.; Itkis, M. E.; Wong, B. M.; Bekyarova, E., Covalent atomic bridges enable unidirectional enhancement of electronic transport in aligned carbon nanotubes. *ACS Applied Materials & Interfaces* **2019,** *11* (21), 19315-19323.

117. Bekyarova, E.; Sarkar, S.; Wang, F.; Itkis, M. E.; Kalinina, I.; Tian, X.; Haddon, R. C., Effect of Covalent Chemistry on the Electronic Structure and Properties of Carbon Nanotubes and Graphene. *Accounts of Chemical Research* **2013,** *46*, 65-76.

Chapter 2. Experimental

This Experimental chapter is divided into four parts corresponding to different projects during my PhD study.

2.1 Shaping perylene with focused ion beam (FIB) milling[1]

Preparation of perylene microcrystals for FIB: A concentrated perylene (PER)/toluene solution (10^{-3} M) was drop-cast onto a clean glass substrate and dried in air, forming a yellow film composed of individual microcrystals. A 4 nm Au conductive layer was coated onto the substrate using electron beam evaporation (Temescal BJD 1800 system). The sample was then mounted in a Leo XB 1540 Focused Ion Beam Milling system (Zeiss).

FIB micro-machining of perylene crystal: The target crystal was first located and imaged by the scanning electron microscopy inside the FIB system. The desired milling patterns were designed during the imaging process using the shape function of SmartSEM software. The milling parameters were also set before switching to FIB imaging in order to minimize pre-milling exposure to the Ga^+ ion beam. After switching to FIB mode, the magnification was set to the same as the SEM magnification. Typically, a slight realignment between the design pattern and the target crystal is needed, after which the sample can be milled by the Ga^+ ion beam. The parameters of FIB imaging and milling are identical (30kV, 50pA) to avoid changing the aperture, which will induce a shift of the beam alignment. The time of milling for each crystal was estimated from the empirical perylene etching rate of 800 s/μm^3. After milling, the Au coating layer was removed by immersing the sample in a

commercial potassium iodide/iodine etchant (Transene Gold Etchant TFA) for 2 s at room temperature, immediately followed by water rinsing.

Microscopy characterization: Optical microscope images were acquired using an Olympus BX51WI microscope. Fluorescence images were taken through a fluorescein isothiocyanate (FITC) filter. Atomic force microscopy (AFM) images were collected using a Digital Instruments Nanoscope IIIA scanned probe microscope system (AFM Probe: NSG01, NT-MDT Spectrum Instruments) in tapping mode. Scanning electron microscopy (SEM) image collection was performed using a Leo XB 1540 Focused Ion Beam Milling system with 5 kV electron beam voltage.

Spectroscopy characterization: Steady state photoluminescence spectra from localized regions in a single crystal were collected using a Nicolet Almega XR Dispersive Raman microscope using 532 nm laser excitation with an estimated focus size of 1 μm. Time-resolved PL experiments were conducted using the time-correlated single photon counting technique. For the high repetition rate experiments, samples were excited with 515 nm light generated by the second harmonic of a 1030 nm (Light Conversion Inc., Pharos) laser with an 80 MHz repetition rate and a 90 fs pulse duration. These samples were first located through the integrated microscope system with a 40× objective (NA= 0.6) before excitation. The PL signal was detected with an avalanche photodiode (PicoQuant, PDM) and its temporal trace was measured by time-correlated single photon counting (PicoQuant, PicoHarp 300). For the lower repetition rate experiments, samples were excited with 400 nm light generated by the second harmonic of a mode-locked 800 nm (Coherent, Inc, Libra)

Ti:Sapphire laser with a 1 kHz repetition rate and a 100 fs pulse duration. Samples were located and excited as previously described, with the PL signal and its temporal trace measured collected by a streak camera and triggering unit (Hamamatsu Photonics, C4334 and C4792-01).

2.2 Encapsulating perylene with graphene[2]

Perylene encapsulation by graphene: All materials were used as received. The perylene (PER) microcrystals were grown from a 10^{-3} M solution of PER (Aldrich) in tetrahydrofuran (Aldrich) and depositing several drops onto a clean glass substrate. After the solvent evaporates, a yellow microcrystal film is left on the substrate. The placement of a graphene sheet on the microcrystals involved adapting techniques from a previously published method.[3] A layer of cellulose acetate was spin-coated (2000 r.p.m.;45s) on the purchased monolayer CVD graphene (Graphene Supermarket). The graphene on the opposite side of the Cu foil was etched away by an oxygen plasma (Oxford Plasmalab 100/180 model; ICP power 300 W; forward power 30 W; etching time 30 s). The Cu foil was then chemically etched away using an aqueous solution of HCl (1 M) and H_2O_2 (0.5 M). The graphene sample was rinsed several times with deionized water and floated on the water surface. The substrate coated with PER microcrystals is then prepared and used within a few minutes after drying. It is submerged in the water and then used to lift up the floating graphene sample. The substrate with transferred graphene was dried in the air for 30 minutes, then immersed in acetone for 1 hour to dissolve the cellulose acetate support layer. Finally, the substrate was rinsed with acetone and dried with gentle air flow.

Prior to microcrystal growth, alignment marks were patterned on the glass substrate using photolithography and deposited through electron beam evaporation (10 nm Cr/100 nm Au) using a Temescal BJD 1800 system in a cleanroom.

Microscopy characterization: Optical microscope images were taken using an Olympus BX51W1 microscope. Fluorescence images were taken using a fluorescein isothiocyanate (FITC) filter under 15s exposure time. SEM image collection was performed on a Leo XB 1540 Focused Ion Beam Milling system. AFM images were collected in tapping mode using a Digital Instruments Nanoscope IIIA scanned probe microscope system (AFM Probe: NSG01, NT-MDT Spectrum Instruments). The AFM cross-section analysis was performed on the AFM image using Nanoscope Control software.

Spectroscopy characterization: Raman spectra were collected with a Nicolet Almega XR Dispersive Raman microscope using 780 nm laser excitation with an estimated focus size of 1 μm. To collect the spectra, 20 scans with an exposure time of 15s were taken. During Raman measurements of plain graphene and graphene coated PER, the Raman signal was first maximized according to the highest intensity of the 2D peak at 2600 cm^{-1}. The laser focus point was then moved to an area without any graphene and a background signal from the glass substrate was collected under the same conditions. Subtraction and manual baseline correction were performed using OMNIC for Dispersive Raman software. Time-resolved photoluminescence measurements were done using 400 nm femtosecond pulses at a 1 kHz repetition rate. The 400 nm excitation wavelength was generated by sending the 800 nm fundamental of a Coherent Libra regeneratively amplified Ti:sapphire laser system

into a frequency doubling Beta Barium Borate (BBO) crystal cavity. The 400 nm pulses were then focused onto the sample in air using an Olympus LCPlanFl 40x, 0.6 NA objective lens. Steady state photoluminescence spectra were collected by the same lens, passed through a dichroic mirror, and detected using a Hanamatsu C4334 streak camera with a time and spectral resolution of 15 ps and 2.5 nm respectively.

2.3 Encapsulating perylene with h-BN[4]

Perylene crystals and PMMA/Lumogen Red film preparation: To prepare isolated perylene (PER) microcrystals, a PER/acetone solution (10^{-3} M) was drop cast onto a glass substrate, which was dried in air. Chemical vapor deposition (CVD) grown monolayer graphene, monolayer h-BN and multilayer h-BN were purchased from Graphene Supermarket. Multilayer h-BN was grown on a Ni substrate using the molecular beam epitaxy (MBE) method, as described previously.[5] To make polymer-dye films for the fluorescence quenching studies, the dye Lumogen Red (LR) and the polymer poly (methyl methacrylate) (PMMA) (MW ≈ 120000 g/mol, Sigma-Aldrich) were codissolved in toluene at an appropriate weight percentage (LR: PMMA ≈ 1:1200). The solution was then diluted with toluene into lower concentrations. The resulting solutions had different viscosities and were spin coated onto the glass substrate at 500-4000 rpm to make solid films with different thicknesses but with the same dye concentration ≈ 1 mM. The final thickness of the polymer layer was measured using atomic force microscopy.

2D material transfer: Two different methods, wet and dry, were used to place the 2D materials in contact with the organic component. In the wet transfer method, a thin (~200

nm) layer of PMMA (Microchem 950 PMMA A4) was spin-coated onto commercially available graphene and h-BN grown by CVD on a Cu substrate or onto MBE grown h-BN on a Ni substrate. The metal support was then chemically etched away using an aqueous solution of HCl (5 wt.% in water) and $FeCl_3$ (0.3M). The etching solution was replaced by deionized water to rinse the 2D samples, and this replacement could be repeated multiple times to extract any remaining metal ions. The previously prepared glass substrate with PER crystals was then used to lift up the floating 2D layer. The substrate with its transferred 2D layer was dried in air for 30 minutes and then immersed in acetone for 1 hour to dissolve PMMA layer. Finally, the substrate was dried with a gentle air flow. For the dry transfer of h-BN, the h-BN layer on Ni was first exfoliated using silicone-free adhesive film (Ultron Systems Inc.). Then the adhesive film was firmly pressed onto the SiO_2/Si substrate using cotton swabs. The film was peeled away slowly and h-BN flakes remained on the SiO_2/Si substrate.

Microscopy characterization: Optical and fluorescence microscopy images were taken using an Olympus BX51W1 microscope. Fluorescence images were taken using either a fluorescein isothiocyanate (FITC) filter cube (resulting in a green image) or a rhodamine conjugate U-MNG filter cube (resulting in a red image). SEM image collection was performed using a Leo XB 1540 Focused Ion Beam Milling system with 3 kV electron beam voltage. Atomic force microscopy AFM images were collected in tapping mode using a Digital Instruments Nanoscope IIIA scanned probe microscope system (AFM Probe: NSG01, NT-MDT Spectrum Instruments). Cross-sectional analysis was performed using the Nanoscope Control software.

Spectroscopic characterization: Steady-state photoluminescence spectra were collected using a Nicolet Almega XR Dispersive Raman microscope with 532 nm laser excitation through a 50x objective (NA = 0.8) with an estimated focus size of 1 μm. Time-resolved photoluminescence experiments were conducted using the time-correlated single photon counting technique. The output of a laser oscillator (Light Conversion Inc., Pharos) at a central wavelength of 1030 nm, with 80 MHz repetition rate and 90 fs pulse duration, was frequency-doubled to 515 nm. These pulses were directed through an integrated microscope system with a 40x objective (NA = 0.6) and used to excite localized sample areas on the order of 1 μm in diameter. The photoluminescence signal was detected with an avalanche photodiode (PicoQuant, PDM) and its temporal trace measured by a time-correlated single photon counting module (PicoQuant, PicoHarp 300). X-ray photoelectron spectroscopy (XPS) characterization was carried out using a Kratos AXIS ULTRADLD XPS system equipped with an Al Kα monochromated X-ray source and a 165-mm mean radius electron energy hemispherical analyzer. The vacuum pressure was kept below 3×10^{-9} torr during the acquisition. A neutralizer was also applied to compensate for charging during the measurement.

2.4 Organometallic functionalization of aligned carbon nanotube[6]

Preparation of aligned SWNT films: Purified unsorted arc discharge SWNTs (P2-SWNTs, Carbon Solution, Inc.) were dispersed in water using sodium deoxycholate (1 wt%). Dispersion with a concentration of 0.4 mg/mL was prepared by ultrasonication in a bath sonicator for 10 min followed by a tip sonication (Cole-Parmer cup-horn sonicator, power level 40 W, 1/2-inch probe) for 1 hr in an ice bath. The obtained dispersion was

centrifuged for 1 hr at 40,000 r.p.m (Beckman TL-100 ultracentrifuge with Beckman TLA-100.3 rotor) in order to remove large SWNT bundles. The supernatant was collected as a stock solution (concentration ~ 20 μg/mL). Aligned SWNT films were prepared by slow filtration using a modified literature procedure [7]. For the filtration a portion of the stock solution was diluted with nano pure water to obtain a dispersion with SWNT concentration of 2 μg/ml (surfactant concentration 0.1%). The SWNT dispersion (2.5 ml) was filtered through a standard vacuum filtration system with a polycarbonate filter membrane (Nuclepore track-etched polycarbonate hydrophilic membranes, 200 nm pore size) without applying vacuum during the filtration. At the end of the filtration process vacuum was applied overnight to dry the SWNT film and the membrane. The film was removed from the filtration system after the SWNT film and the membrane were completely dry.

Fabrication of two-terminal devices: Two-terminal devices were fabricated to study the effect of hexahapto complexation of Cr on the resistance of aligned SWNT films. The aligned SWNT thin films were transferred on a glass substrate with pre-patterned gold contacts separated by 10 μm (channel length). The SWNT films width was in the range of 500 - 800 μm. For device preparation, substrate the polycarbonate filter/SWNT film was placed on the substrate with the SWNT film facing the glass surface and a few drops of ethanol were added to improve adhesion. The polycarbonate membrane was removed by first dissolving in n-methyl-2-pyrrolidone (NMP) vapors followed with an NMP bath washing for 1 hr. Two device configurations were used in which the SWNT alignment direction was transverse and parallel to the channel length (respectively current flow). The

devices were annealed at 300 ºC for 8 hours in vacuum (10^{-6} torr) and immediately transferred into a glove box for the photochemical reaction.

Photochemical reaction: $Cr(CO)_6$ (Sigma Aldrich 98%) was dissolved in degassed acetonitrile inside a glove box to obtain a solution with concentration of 1×10^{-3} M. Using a pipette, a drop (~0.1 mL) of the solution was cast onto the SWNT film surface, followed by irradiation with UVC light of 254 nm.

Fabrication of electro-optical switches with aligned SWNT thin films: Aligned SWNT film devices fabricated in the transverse configuration were annealed at 300 ºC for 8 hours in vacuum (10^{-6} torr) and transferred to a glove box. In these experiments the aligned SWNT thin film devices had a channel length of 100 μm and width in the range of 500 to 800 μm. The films were sealed using adhesive frames (Frame-SealTM, Bio-Rad Laboratories) and the chamber of the frame was filled with an acetonitrile solution of $Cr(CO)_6$ (0.05 mM) and ionic liquid (diethylmethyl(2-methoxyethyl)ammonium bis(trifluoromethylsulfonyl) imide, DEME-TFSI, IoLiTec, Inc.). The volumetric ratio of Cr reagent solution to DEME-TFSI was 85:15. A Pt wire (d = 25 μm, Alpha Aesar), inserted through the seal into the solution, was used to apply potential (top gate). A quartz substrate (2.54 cm x 2.54 cm x 1 mm; Ted Pella) served as an UV-transparent window. The potential applied between source (S) and drain (D) was 0.05 V (Keithley 236) and the gate voltage (VG) was 0.6 V (Keithley 2700). The data was collected with a custom LabView software.

Microscopy characterization: For the AFM scanning, glass substrates with transferred aligned SWNTs films were placed on the AFM stage to collect images in a tapping mode with Digital Instruments Nanoscope IIIA. For collecting AFM images of SWNT dispersions, a drop was cast on a freshly cleaved mica and dried in air. For the SEM imaging, aligned SWNTs were transferred onto a glass substrate and imaged with a Leo XB1540 Focused Ion Beam Mill SEM using in-lens mode in the cleanroom of the University of California, Riverside.

Spectroscopy characterization: Absorption spectra of films and dispersions of SWNTs were collected with a Varian Cary 5000 spectrophotometer. Spectra of aligned SWNTs were recorded on films transferred on a glass substrate. Raman spectra were recorded with a Nicolet Almega XR Dispersive Raman microscope using 532 nm laser excitation at 25% power source; laser spot size is 1 μm. The aligned SWNTs on glass substrates were rotated to the position parallel and perpendicular to the polarized electric field of the laser beam.

Resistance Measurement: The resistance of the films was monitored in-situ with a LabVIEW-controlled Keithley 236 source measure unit connected to the device set-up inside the glove box via an electrical feedthrough.

References

1. Li, W.; van Baren, J.; Berges, A.; Bekyarova, E.; Lui, C. H.; Bardeen, C. J., Shaping Organic Microcrystals Using Focused Ion Beam Milling. *Crystal Growth & Design* **2020,** *20* (3), 1583-1589.

2. Li, W.; Tierce, N. T.; Bekyarova, E.; Bardeen, C. J., Protection of Molecular Microcrystals by Encapsulation under Single-Layer Graphene. *ACS Omega* **2018,** *3*, 8129-8134.

3. Chen, M.; Li, G.; Li, W.; Stekovic, D.; Arkook, B.; Itkis, M. E.; Pekker, A.; Bekyarova, E.; Haddon, R. C., Large-scale cellulose-assisted transfer of graphene toward industrial applications. *Carbon* **2016,** *110*, 286-291.

4. Li, W.; Tian, H.; van Baren, J.; Berges, A.; Altaiary, M. M.; Liu, E.; Bekyarova, E.; Lui, C. H.; Liu, J.; Bardeen, C. J., Hexagonal Boron Nitride Encapsulation of Organic Microcrystals and Energy-Transfer Dynamics. *Journal of Physical Chemistry C* **2020,** *124* (38), 21170-21177.

5. Xu, Z.; Tian, H.; Khanaki, A.; Zheng, R.; Suja, M.; Liu, J., Large-Area Growth of Multilayer Hexagonal Boron Nitride on Polished Cobalt Foils by Plasma Assisted Molecular Beam Epitaxy. *Scientific Reports* **2017,** *7*, 43100/1-7.

6. Chen, M.; Li, W.; da Silveira Venzel, T. E.; Li, G.; Itkis, M. E.; Haddon, R. C.; Bekyarova, E., Effect of constructive rehybridization on transverse conductivity of aligned single-walled carbon nanotube films. *Materials Today* **2018,** *21* (9), 937-943.

7. He, X. W.; Gao, W. L.; Xie, L. J.; Li, B.; Zhang, Q.; Lei, S. D.; Robinson, J. M.; Haroz, E. H.; Doorn, S. K.; Wang, W. P.; Vajtai, R.; Ajayan, P. M.; Adams, W. W.; Hauge, R. H.; Kono, J., Wafer-scale Monodomain Films of Spontaneously Aligned Single-walled Carbon Nanotubes. *Nature Nanotechnology* **2016,** *11* (7), 633-638.

Chapter 3. Shaping Organic Microcrystals Using Focused Ion Beam Milling

We start with exploring the morphology effect on a basic carbon-based system—polyaromatic hydrocarbon (PAH) molecules. In physical chemistry world, one of the most interesting states of PAH molecules is when they crystalize into molecular crystals. Here, we develop a new approach to modify the bulk shape of molecular crystals with nm resolution using focused ion beam milling. Photophysical properties of shaped crystal is also studied.

Introduction

Molecular crystals are widely used in science for structure determination via x-ray or electron diffraction techniques. But organic crystals are starting to attract attention as functional materials in their own right. The molecular ordering and lack of grain boundaries in a single crystal can lead to very high charge and exciton mobilities, making them attractive candidates for field-effect transistors and photovoltaic cells.[1] [2] The unique mechanical properties of molecular crystals have also attracted attention, especially their ability to utilize thermal or photoinduced phase transitions to generate mechanical work or motion.[3-4] In the emerging field of functional molecular crystals, there are several levels of material engineering that need to be considered. First, there is the molecule itself, whose properties can be tuned using the methods of chemical synthesis. Second, the molecular packing can be modified using the tools of crystal engineering. Third, the morphology

(size, shape and orientation) of the crystal can be modified. This last phase of control is necessary for the incorporation of single crystals into practical devices but has proven challenging. Crystal growth is controlled by noncovalent self-assembly processes that are sensitive to both molecular-scale phenomena (nucleation and molecular interactions) and larger scale phenomena like mass transport and crystal-substrate attachment.

In order to gain some degree of control over molecular crystal shape, most workers adopt a "bottom-up" strategy in which environmental factors are used to influence the self-assembly process. These strategies include modifying solvent and surfactant growth conditions[5-8], surface functionalization[9-12], templated growth [13-15]or the use of highly nonequilibrium conditions like laser guided growth.[16-18] All these approaches have met with some success, but the field has yet to identify a general method that can guide molecules to self-assemble into a predetermined shape. In many cases, a relatively broad distribution of crystal sizes and orientations is obtained, and the crystals often retain their intrinsic habit, e.g. rectangular prisms, needles, or plates. Meanwhile, the inorganic community often utilizes "top-down" subtractive methods to generate arbitrary shapes in materials like silicon. Electron and photon-based lithography techniques utilize patterned illumination and etching to selectively remove sections of the parent crystal, leaving only the desired shape. More recently, focused ion beam (FIB) milling has been used to physically abrade away selected regions of the starting crystal. [19-22] Both electron beam lithography[23] and FIB milling[24] have the ability to create user-defined features on sub-10 nm lengthscales.

Given the advanced state of "top-down" nanofabrication techniques, we became interested in whether they could be applied to the problem of shape control in molecular crystals. Electron lithography and photolithography typically require coating the crystal with a resist polymer that can be patterned and redissolved. This strategy is difficult to implement with molecular crystals due to solubility constraints: the same solvent used to deposit the resist may also dissolve the crystal, leading to a mixed interfacial layer or loss crystallinity. FIB milling, on the other hand, utilizes the direct impact of ions to knock out material, without the need for intermediate chemical steps like polymer spin-coating or reactive etching. The operator can visualize the object in real time using electron microscopy to direct the milling beam. This method can in principle bypass chemical compatibility issues. However, there are several challenges in applying it to organic materials. First, most organic solids are insulators, so using electron microscopy to align and visualize the object during the milling process presents a challenge. Second, organic materials are prone to damage by energetic charged particles, both the electrons used for imaging and the atomic ions used for cutting. Third, a considerable amount of heat can be deposited by the energetic ions, which can induce melting or other phase changes in soft materials like organic crystals and polymers. These practical difficulties may explain the scarcity of FIB-milling results on organic solids. Although it has been used to cut patterns into a variety of polymers[25-28] and photonic structures into perovskite crystals[29-30], so far there has been no report of using FIB-milling to shape an organic molecular crystal.

In this chapter, we explore the use of FIB-milling to cut arbitrary two-dimensional shapes into crystal plates of the organic semiconductor molecule perylene (PER). The key step is

the application of an ultrathin gold coating that protects the crystal during ion exposure, followed by a KI/I_2 Au removal step that does not harm the organic. Using the FIB, we are able to completely remove selected portions of a single crystal, as well as write sub-micron features into single crystals. These proof-of-principle experiments represent an encouraging first step in the use of FIB-milling to create molecular crystals with user-defined shapes that could enable systematic studies of how crystal morphology affects function.

Results and Discussion

We chose the α-polymorph of crystalline PER as a model molecular crystal system to demonstrate the FIB-milling approach. PER is a polyaromatic hydrocarbon whose core structure has been used as the basis for molecules with applications as electron acceptors in solar cells, singlet fission chromophores, field effect transistors, and organic light-emitting diodes.[31] Its melting point is 255 °C, and the crystal also sublimes at moderate temperatures, so it is representative of the typical challenges that will be encountered for organic molecular crystals. Another advantage of PER crystals is their strong photoluminescence (PL) that arises from excimers that form in the α-polymorph.[32-34] This PL signal provides a facile way to characterize the crystal and assess damage and/or phase changes. The α-polymorph of PER grows in distinctive square or diamond shaped plates, ideal for testing two-dimensional (2D) FIB-milling techniques. The size and thickness of these plates depends on growth conditions. For the solvent evaporation method used here, the plates were typically 5-10 microns wide and 200-2000 nanometers thick.

As mentioned in the Introduction, it is impossible to directly image a molecular crystal inside a FIB-milling apparatus due to rapid charge accumulation in the poorly conducting organic. Our goal was to encapsulate the crystal under a conductive coating that was either transparent or could be easily removed. We first tried graphene as an encapsulating layer, as this 2D material can provide sufficient surface conductivity for SEM imaging while not perturbing the underlying crystal.[35] Unfortunately, even at the lowest electron beam energies, exposure to the electron imaging beam during the alignment and positioning procedure led to a loss of PL intensity of 80% or more in the absence of milling. In order to provide more protection for the crystal, we turned to an electron-beam evaporated Au coating. We found that a 4 nm Au layer preserved more than 90% of the crystal's original PL signal (see below) while providing sufficient surface conductivity to obtain high resolution SEM images.

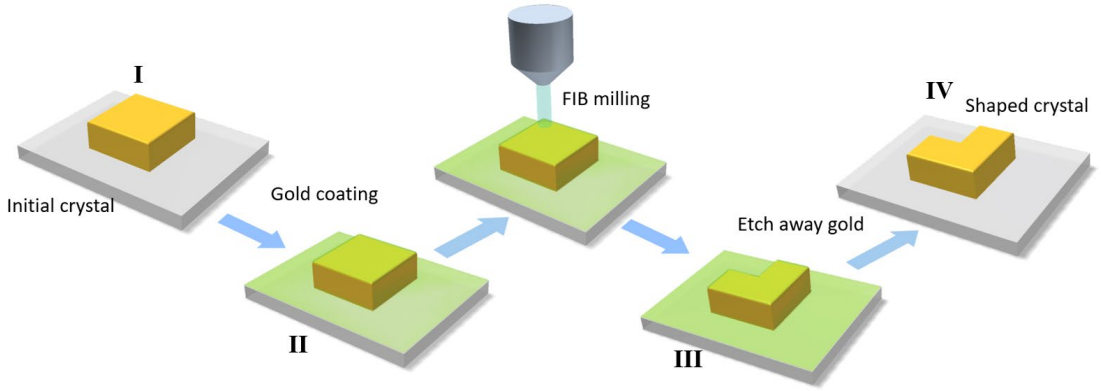

Figure 3.1. Schematic illustration of the FIB micro-machining process for molecular crystals. The PER crystal (I) is first coated with a 4 nm thick gold layer (shown as a green translucent coating). The coated sample (II) is mounted in the FIB chamber and milled into the designed shape. After milling, the shaped crystal (III) is dipped into a KI/I_2 etching solution to remove the gold layer. After rinsing with water, the shaped crystal (IV) is allowed to dry before characterization.

After Au coating, the crystal was placed in the FIB-SEM system and scanned using an electron beam. Once the target crystal was located by SEM imaging, a directional beam of high energy Ga^+ ions was used to remove sections of the crystal. The voltage was kept as low as possible to avoid potential damage from ions deflected into non-target areas of the crystal. We empirically found an etching rate of ~800 s/μm^3, given a 50-pA ion beam at 30 kV. Lower voltages resulted in an unacceptably low milling rate. After the milling process was complete, the shaped crystals could be re-imaged using SEM to confirm the desired shape. Finally, the crystal was removed from the FIB apparatus and the protective Au layer was dissolved using a commercial etching solution. Although Aqua Regia is the most commonly used etchant to remove Au, this strong oxidant would also react with the underlying organic. Instead, we used a commercial iodine-based etchant that left the organic intact. The entire process is schematically illustrated in Figure 3.1.

In Figure 3.2 we show some examples of FIB-milled PER crystals. The first two images show a microplate before (a) and after (b) the excision of a square region inside the plate. Figure 3.2c shows a crystal after a square has been milled out of the side. Note that the milled region extends past the crystal, and so some of the glass substrate was also removed, leaving a pit adjacent to the target crystal. In Figure 3.2d we show a square plate that has been cut in half by the FIB. Note that in all the fluorescence images, the edges of the crystals typically appear brighter than the interior regions. This is because PL that is emitted below the critical angle is trapped within the high-index crystal and waveguided to the edges, where it is scattered out.[36]

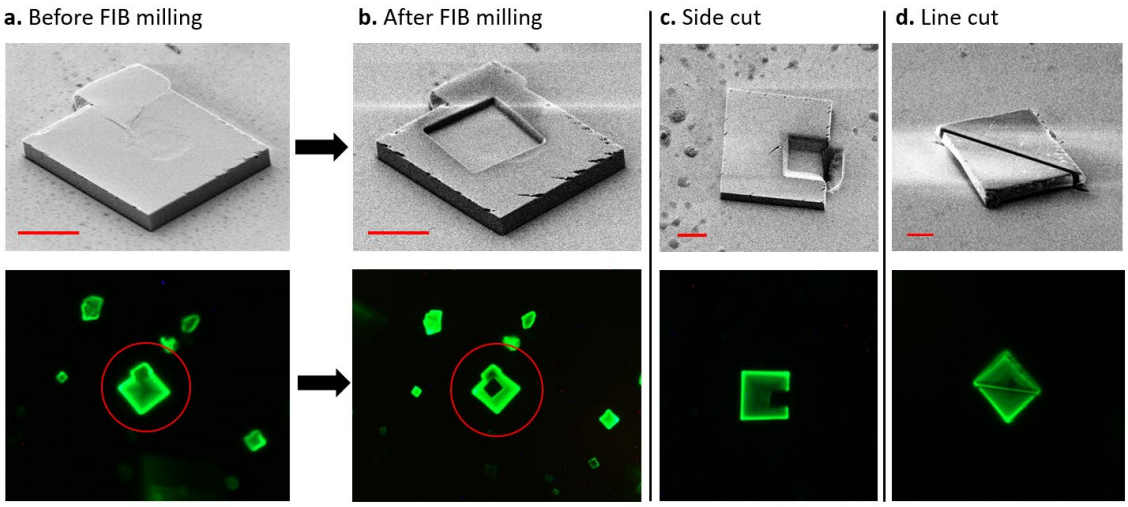

Figure 3.2. SEM (top) and fluorescence (bottom) images of FIB-milled PER crystals. A single PER crystal before a) and after b) FIB-milling of a square in the center of the crystal, resulting in a frame structure. c) a PER crystal with a rectangular cut on the side that extends into the substrate, d) a square crystal cut into two triangles. For all SEM images, the scale bar = 4 μm. The crystals in the fluorescence image are the same crystals in the SEM images above.

The resolution of the cutting can be assessed by measuring the full-width-half-maximum (FWHM) and depth of a single line drawn across a crystal face. Figure 3.3a shows a single cut across a PER crystal (FWHM=135±10 nm), while Figure 3.3b shows one across a silicon dioxide surface (FWHM = 130±10 nm). Both cuts have the same average depth of 40 nm. The FIB milling parameters for PER and silicon dioxide are the same to within the error, so it does not appear that softening of the organic limits the resolution of the milling, at least on the 100 nm lengthscale. Optimization of the crystal thickness and FIB parameters would hopefully reduce this width well below 100 nm.

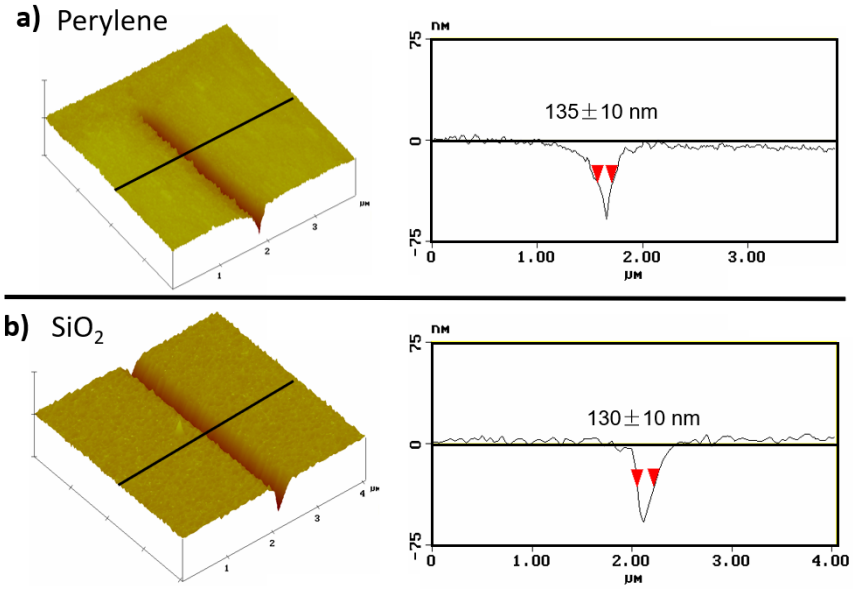

Figure 3.3. AFM surface scans of a) a PER crystal and b) a SiO2 substrate after a single cut using the FIB. For both images, the cross-section of the cut can be extracted, leading to similar full-width-half-maximum values of 135±10 nm and 130±10 nm for the two substrates.

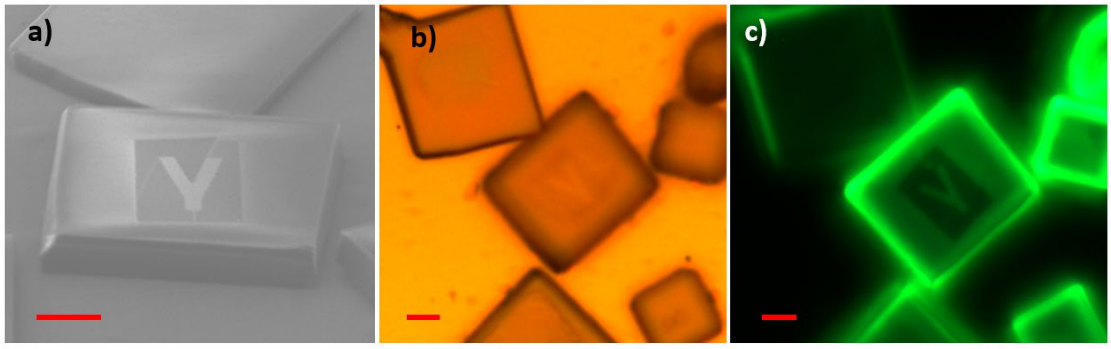

Figure 3.4. a) SEM image of a Y shape imprinted onto the surface of a PER crystal, with the surrounding material removed to a depth of 20 nm. Transmission (b) and fluorescence (c) microscopy images of the same crystal. For all images, the scale bar = 4 μm.

The shapes in Figure 3.2 rely on the complete removal of the crystal in specified regions along orthogonal directions. The FIB can also be programmed to cut more complex shapes with specified depths, rather than cutting completely through the crystal. To illustrate this capability, we programmed the FIB to remove material and leave the letter Y inside a

10×10 μm square PER crystal with a thickness of 2 μm. The Y-shape is analogous to a planar waveguide optical splitter structure used in photonic circuits.[37] The cutting speed parameters were adjusted to only remove the top 20 nm of crystal in a square around the Y shape. Figure 3.4a shows an SEM image of the outcome of this procedure, with the Y clearly imprinted in a square well cut in the interior of the larger crystal. This Y shape resides on top of the rest of the crystal, while the underlying PER foundation remains intact. This can be clearly seen in the optical microscopy image in Figure 3.4b, where the Y is barely visible on top of the yellow-orange crystal. The contrast becomes more pronounced in the fluorescence microscopy image in Figure 3.4c, where the Y emits green fluorescence while the underlying square that has been milled is dark. This dark background indicates that the exposed regions of the crystal experience significant PL quenching, even though the SEM and transmitted light microcopy images show that the underlying PER crystal is still intact. This is not surprising, since once the protective Au coating has been milled away, the organic will be exposed to high energy ions that are known to introduce both chemical and physical defects in polymers.[38-40] In Figure 3.5, a comparison of the roughness of the PER crystal surface before and after exposure to the milling beam showed a slight increase in mean roughness, from 0.6 nm to 1.2 nm, which may also be indicative of damage.

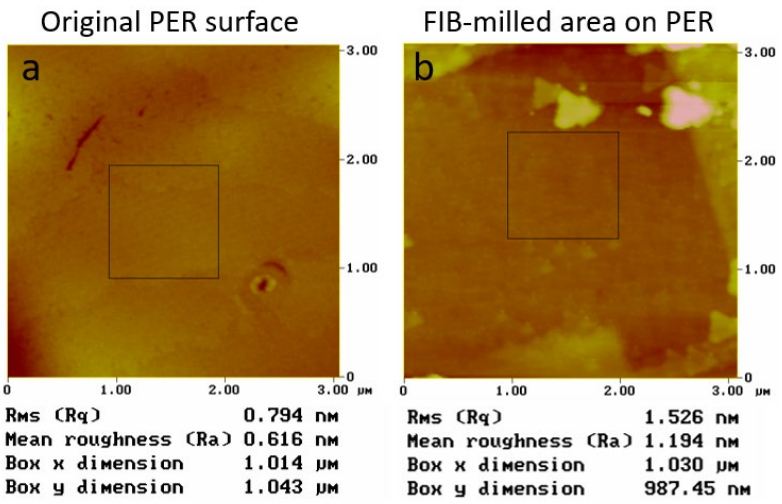

Figure 3.5. AFM roughness analysis of the Y-imprinted PER crystal (Figure 3.4) surface before (a) and after (b) FIB milling. The area in (b) is outside the Y shape, an area where the FIB beam removed material. The mean surface roughness increases from 0.6 nm to 1.2 nm after milling by the ion beam.

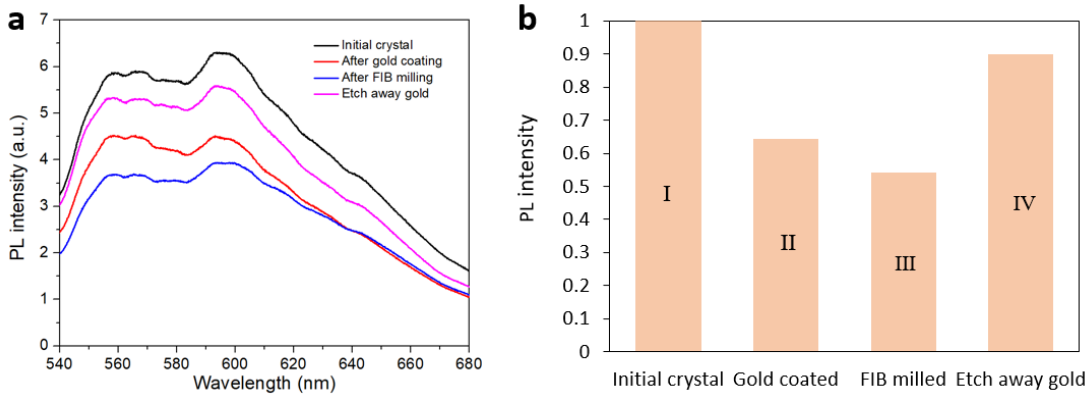

Figure 3.6. a) PL spectrum of a PER crystal at each step given in Figure 3.1. All the spectra are collected from a spot located within 2-4 µm of the FIB milling area. b) Comparison of the integrated PL intensity at each step given in Figure 3.1. After Au coating and FIB-milling, the PL intensity decreases by about 45%, but it recovers to 90% of its original value after the Au layer is etched away.

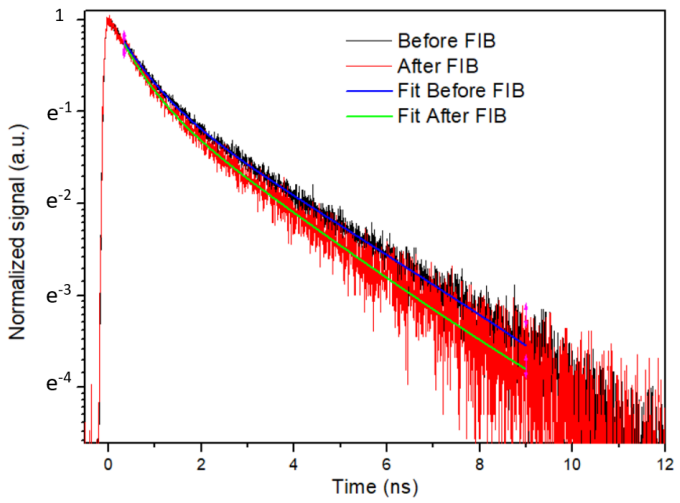

Figure 3.7. PL decays with biexponential fits before (black) and after (red) the PER crystal undergoes the FIB shaping process. After FIB milling, the average PL lifetime decreases slightly.

One important question is whether the regions of the crystal that are not directly exposed to the milling beam also sustain damage. In Figures 3.2 and 3.5, the crystal regions that have not been exposed to the ion beam appear to retain their full PL intensity, but we wanted to check this quantitatively. We used a confocal microscope to collect PL spectra from specific regions of a single crystal located 2-4 μm away from the milled region. In Figure 3.6a we show the PL spectrum of a single crystal taken at various points during the procedure shown in Figure 3.1. All four spectra share the same broad shape characteristic of the α-PER excimer. Figure 3.6b shows that the integrated PL intensity drops by 40% after the 4 nm Au layer is applied. This semitransparent layer can quench the excimer both through nonradiative energy transfer and by absorbing/reflecting the radiated photons. After milling, the PL signal dropped again by about 10%. However, this decrease could be due to the loss of material as well as chemical damage from the milling process. After removal of the Au, the PL recovered to 90% of the original level. Thus, the overall loss of

PL due to the milling procedure was about 10%. Experiments on other crystals consistently yielded an 8-12% decrease in the PL intensity.

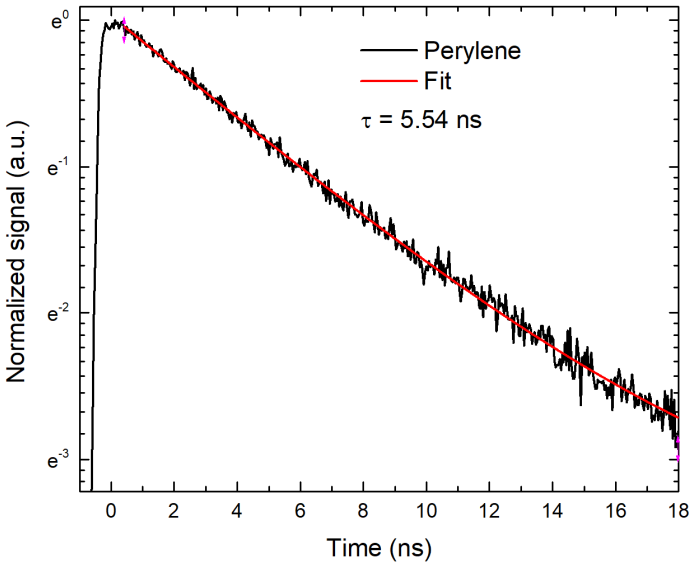

Figure 3.8. PL decays with biexponential fits of the original PER crystal excited by a 1 kHz laser. The signal is collected by a streak camera. The average lifetime here is 5.54 ns, which is longer than the result from single photon counting measurement using an 80 MHz laser.

$Ae^{-t/\tau_A} + Be^{-t/\tau_B}$	A	τA (ns)	B	τB (ns)	τ average (ns)
Before FIB	0.463	3.220	0.326	0.697	2.17
After FIB	0.449	2.730	0.301	0.588	1.87

Table 3.1. The lifetimes and pre-exponential factors used to fit the PL decays.

The PL decays of a crystal before and after the FIB-milling procedure had similar shapes, as shown in Figure 3.6. The decays are biexponential, of the form $Ae^{-t/\tau_A} + Be^{-t/\tau_B}$, and the lifetimes and pre-exponential factors are summarized in Table 1. The average lifetime, given by $\frac{A\tau_A + B\tau_B}{A+B}$, is proportional to the integrated fluorescence intensity and decreases from 2.17 ns to 1.87 ns. This 13% decrease is close to the 10% decrease in steady-state

intensity shown in Figure 3.5. Both the short and long decay times decrease in the exposed sample, consistent with quenching of the mobile excimer states by defects in the PER crystal. If the loss of PL intensity was merely due to the loss of material, with the surrounding PER crystal unaffected, then we would expect to see the same excimer lifetime from the exposed and unexposed portions. We note that the average PL lifetime of the PER crystals reported here is shorter than that reported by us previously[35], which we attribute to the use of a high repetition rate laser for these microscopy measurements. The high repetition rate and small spot size can lead to localized heating of the crystal, which will accelerate the PL decay. In Figure 3.8, we confirmed that when bulk measurements were done on the same crystals at a lower repetition rate (1 kHz) we obtained longer decays consistent with our earlier paper.

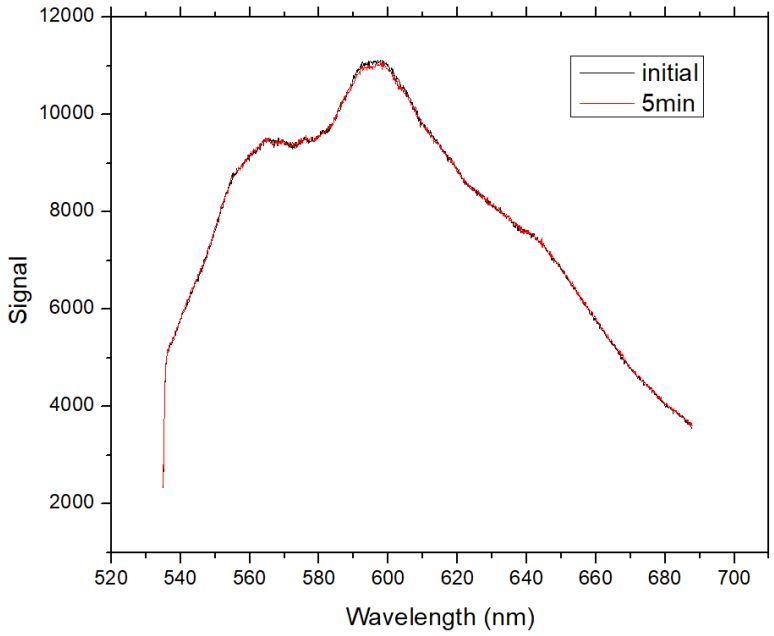

Figure 3.9. Photoluminescence intensity of the pure perylene crystal (without gold coating) before and after dipping into gold etchant.

The loss of PL intensity in the surrounding crystal regions may originate from several factors. For example, the I_2 in the etching solution may be incorporated into the PER crystal and lead to doping.[41-42] We tested for this possibility by exposing the crystals to the etching solution in the absence of Au coating or ion exposure. No measurable drop in PL intensity was observed for these samples as shown in Figure 3.9. However, if the crystals were coated with Au and then etched away without exposure to FIB milling, a 5% drop in PL was observed as shown in Figure 3.10. This result suggests that half of the observed PL loss can be attributed to effects from the coating itself, possibly due to diffusion of Au atoms into the organic phase.[43] The other 5% PL loss is presumably due to ion exposure during the FIB procedure. The process of locating and aligning the sample with the SEM/FIB beam causes the entire crystal to be exposed to charged particles, some of which penetrate the Au coating. Both of these sources of damage can be reduced by further optimization of the procedure. A thicker Au coating and more efficient alignment procedure should reduce the exposure of the organic to ions. Extending the etching period or heating the crystal may facilitate removal of Au atoms. However, the retention of 90% of the PL already represents an improvement relative to the 70% PL retention seen in perovskite thin films that are processed using gas-assisted FIB milling, and we did not make a systematic effort to improve the PL retention for this study. Finally, we should emphasize that a PL decrease of 10% does not necessarily mean that 10% of the crystal has been destroyed. Efficient energy migration in molecular crystals can amplify the effect of even low-density defects, leading to a substantial loss of PL.[44-46]

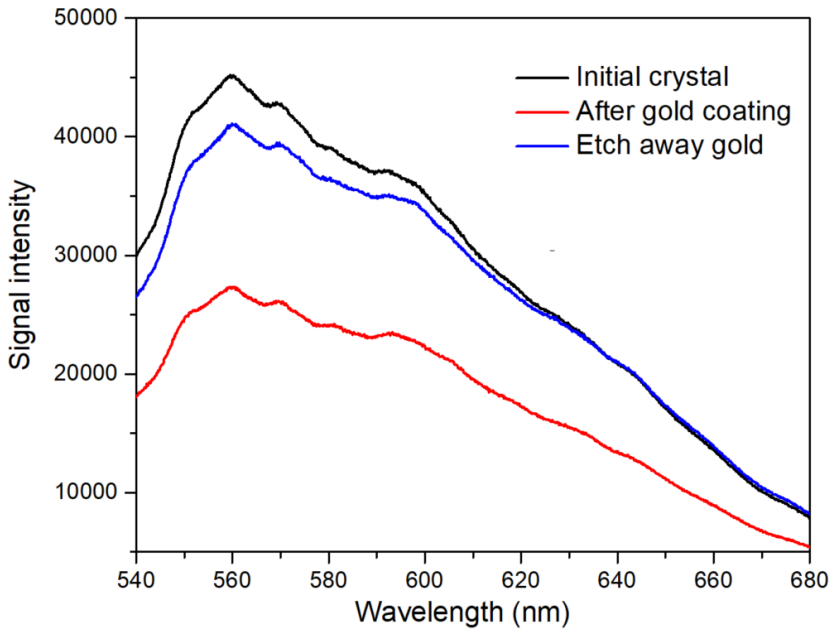

Figure 3.10. Photoluminescence intensity change of the Au-coated crystal without FIB exposure before and after the Au coating is etched away. This crystal was on the same substrate as a shaped crystal, but without direct exposure to ion beam.

Conclusion

The results in this article show that it is possible to apply the techniques of FIB-milling to shape molecular crystals. The use of an ultrathin Au coating and its removal using a KI/I2 etchant provides a gentle way to prepare the crystal for imaging in the FIB apparatus while protecting it from electron beam damage. Using this approach, we have milled features with a spatial resolution on the order of 130 nm while retaining 90% of the original PL intensity in the un-milled regions of the crystal. Even smaller features should be possible using more advanced FIB techniques and thinner crystals. While the top-down FIB method is not practical for mass-producing shaped microcrystals, it provides a new capability to create complex shapes in single crystals with high spatial resolution. This capability can

enable the exploration of how variations in crystal shape lead to different optical, electronic and mechanical properties. These insights can then guide the design of new materials that incorporate molecular crystal elements, for example waveguides or photomechanical actuators.

References

1. Reese, C.; Bao, Z., Organic single-crystal field-effect transistors. *Materials Today* **2007,** *10* (3), 20-27.

2. Najafov, H.; Lee, B.; Zhou, Q.; Feldman, L. C.; Podzorov, V., Observation of long-range exciton diffusion in highly ordered organic semiconductors. *Nature Materials* **2010,** *9* (11), 938-943.

3. Kim, T.; Zhu, L.; Al-Kaysi, R. O.; Bardeen, C. J., Organic photomechanical materials. *ChemPhysChem* **2014,** *15*, 400-414.

4. Naumov, P.; Chizhik, S.; Panda, M. K.; Nath, N. K.; Boldyreva, E., Mechanically Responsive Molecular Crystals. *Chemical Reviews* **2015,** *115*, 12440-12490.

5. Zhang, X.; Dong, C.; Zapien, J. A.; Ismathullakhan, S.; Kang, Z.; Jie, J.; Zhang, X.; Chang, J. C.; Lee, C.-S.; Lee, S.-T., Polyhedral Organic Microcrystals: From Cubes to Rhombic Dodecahedra. *Angewandte Chemie International Edition* **2009,** *48* (48), 9121-9123.

6. Lin, Z.-Q.; Sun, P.-J.; Tay, Y.-Y.; Liang, J.; Liu, Y.; Shi, N.-E.; Xie, L.-H.; Yi, M.-D.; Qian, Y.; Fan, Q.-L.; Zhang, H.; H. H. Hng; Ma, J.; Zhang, Q.; Huang, W., Kinetically Controlled Assembly of a Spirocyclic Aromatic Hydrocarbon into Polyhedral Micro/Nanocrystals. *ACS Nano* **2012,** *6*, 5309–5319.

7. Al-Kaysi, R. O.; Zhu, L.; Al-Haidar, M.; Al-Muhannah, M. K.; El-Boubbou, K.; Hamdan, T. M.; Bardeen, C. J., Chemical reaction method for growing photomechanical organic microcrystals. *CrystEngComm* **2015,** *17* (46), 8835-8842.

8. Peng, L.; Chen, Y.-N.; Dong, Y. Q.; He, C.; Wang, H., Surfactant-assisted self-assembled polymorphs of AIEgen di (4-propoxyphenyl) dibenzofulvene. *Journal of Materials Chemistry C* **2017,** *5* (3), 557-565.

9. Briseno, A. L.; Mannsfeld, S. C. B.; Ling, M. M.; Liu, S.; Tseng, R. J.; Reese, C.; Roberts, M. E.; Yang, Y.; Wudl, F.; Bao, Z., Patterning organic single-crystal transistor arrays. *Nature* **2006,** *444*, 913-917.

10. Schiek, M.; Balzer, F.; Al-Shamery, K.; Brewer, J. R.; Lutzen, A.; Rubahn, H. G., Organic molecular nanotechnology. *Small* **2008,** *4*, 176-181.

11. Wilkinson, F. S.; Norwood, R. F.; McLellan, J. M.; Lawson, L. R.; Patrick, D. L., Engineered growth of organic crystalline films using liquid crystal solvents. *Journal of the American Chemical Society* **2006,** *128*, 16468-16469.

12. Minemawari, H.; Yamada, T.; Matsui, H.; Tsutsumi, J.; Haas, S.; Chiba, R.; Kumai, R.; Hasegawa, T., Inkjet printing of single-crystal films. *Nature* **2011,** *475*, 364-367.

13. Ha, J.-M.; Wolf, J. H.; Hillmyer, M. A.; Ward, M. D., Polymorph Selectivity under Nanoscopic Confinement. *Journal of the American Chemical Society* **2004,** *126*, 3382-3383.

14. Jiang, Q.; Ward, M. D., Crystallization under Nanoscale Confinement. *Chemical Society Reviews* **2014,** *43*, 2066--2079.

15. Al-Kaysi, R. O.; Bardeen, C. J., General Method for the Synthesis of Crystalline Organic Nanorods using Porous Alumina Templates. *Chemical Communications* **2006**, 1224–1226.

16. Balzer, F.; Rubahn, H. G., Laser-controlled Growth of Needle-shaped Organic Nanoaggregates. *Nano Letters* **2002,** *2*, 747-750.

17. Okutsu, T.; Nakamura, K.; Haneda, H.; Hiratsuka, H., Laser-Induced Crystal Growth and Morphology Control of Benzopinacol Produced from Benzophenone in Ethanol/Water Mixed Solution. *Crystal Growth & Design* **2004,** *4*, 113-115.

18. Sugiyama, T.; Masuhara, H., Laser-Induced Crystallization and Crystal Growth. *Chemistry: An Asian Journal* **2011,** *6*, 2878 – 2889.

19. Giannuzzi, L. A.; Stevie, F. A., A Review of Focused Ion Beam Milling Techniques for TEM Specimen Preparation. *Micron* **1999,** *30*, 197-204.

20. Tseng, A. A., Recent Developments in Nanofabrication Using Focused Ion Beams. *Small* **2005,** *1*, 924-939.

21. Special Issue on "Focused Ion Beam Microscopy and Micromachining". *MRS Bulletin* **2007,** *32* (5).

22. Rajput, N. S.; Luo, X., FIB Micro-/Nano-Fabrication. In *Micro and Nano Technologies, Micromanufacturing Engineering and Technology*, Qin, Y., Ed. William Andrew Publishing: London, 2015; pp 61-80.

23. Manfrinato, V. R.; Zhang, L.; Su, D.; Duan, H.; Hobbs, R. G.; Stach, E. A.; Berggren, K. K., Resolution Limits of Electron-Beam Lithography toward the Atomic Scale. *Nano Letters* **2013,** *13*, 1555-1558.

24. Menard, L. D.; Ramsey, J. M., Fabrication of Sub-5 nm Nanochannels in Insulating Substrates Using Focused Ion Beam Milling. *Nano Letters* **2011,** *11*, 512-517.

25. Niihara, K.-i.; Kaneko, T.; Suzuki, T.; Sato, Y.; Nishioka, H.; Nishikawa, Y.; Nishi, T.; Jinnai, H., Nanoprocessing and Nanofabrication of a Structured Polymer Film by the Focused-Ion-Beam Technique. *Macromolecules* **2005,** *38*, 3048-3050.

26. Guan, L.; Peng, K.; Yang, Y.; Qiu, X.; ChenWang, The Nanofabrication of Polydimethylsiloxane Using a Focused Ion Beam. *Nanotechnology* **2009,** *20*, 145301/1-5.

27. Kochumalayil, J. J.; Meiser, A.; Soldera, F.; Possarta, W., Focused Ion Beam Irradiation – Morphological and Chemical Evolution in PMMA. *Surf. Interface Anal.* **2009,** *41*, 412–420.

28. Lee, C. C.; Proust, G.; Alici, G.; Spinks, G. M.; Cairney, J. M., Three-Dimensional Nanofabrication of Polystyrene by Focused Ion Beam. *J. Microscopy* **2012,** *248*, 129-139.

29. Alias, M. S.; Dursun, I.; Shi, D.; Saidaminov, M. I.; Diallo, E. M.; Priante, D.; Ng, T. K.; Bakr, O. M.; Ooi, B. S., Focused-Ion Beam Patterning of Organolead Trihalide Perovskite for Subwavelength Grating Nanophotonic Applications. *Journal of Vacuum Science & Technology B* **2015,** *33*, 051207/1-9.

30. Alias, M. S.; Yang, Y.; Ng, T. K.; Dursun, I.; Shi, D.; Saidaminov, M. I.; Priante, D.; Bakr, O. M.; Ooi, B. S., Enhanced Etching, Surface Damage Recovery, and Submicron Patterning of Hybrid Perovskites using a Chemically Gas-Assisted Focused-Ion Beam for Subwavelength Grating Photonic Applications. *Journal of Physical Chemistry Letters* **2016,** *7*, 137−142.

31. Zhan, X.; Facchetti, A.; Barlow, S.; Marks, T. J.; Ratner, M. A.; Wasielewski, M. R.; Marder, S. R., Rylene and Related Diimides for Organic Electronics. *Advanced Materials* **2011,** *23*, 268–284.

32. Walker, B.; Port, H.; Wolf, H. C., The Two-Step Excimer Formation in Perylene Crystals. *Chemical Physics* **1985,** *92*, 177-185.

33. Fujino, T.; Tahara, T., Femtosecond Fluorescence Up-Conversion Microscopy: Exciton Dynamics in α-Perylene Microcrystal. *Journal of Physical Chemistry B* **2003,** *107*, 5120-5122.

34. Pick, A.; Klues, M.; Rinn, A.; Harms, K.; Chatterjee, S.; Witte, G., Polymorph-Selective Preparation and Structural Characterization of Perylene Single Crystals. *Crystal Growth & Design* **2015,** *15*, 5495-5504.

35. Li, W.; Tierce, N. T.; Bekyarova, E.; Bardeen, C. J., Protection of Molecular Microcrystals by Encapsulation under Single-Layer Graphene. *ACS Omega* **2018,** *3*, 8129-8134.

36. Takazawa, K., Understanding the Emission Pattern Produced by Focused Laser Beam Excitation of Perylene Square Single Crystals. *Chemical Physics Letters* **2017,** *667*, 284-289.

37. Prajzler, V.; Maštera, R.; Špirková, J.; Jeřábek, V., Compact Multimode Polymer Optical 1×2 Y Splitters with Large Core Planar Waveguide. *Journal of Optics* **2014,** *43*, 310–316.

38. Kim, S.; Park, M. J.; Balsara, N. P.; Liu, G.; Minor, A. M., Minimization of Focused Ion Beam Damage in Nanostructured Polymer Thin Films. *Ultramicroscopy* **2011,** *111*, 191–199.

39. Allen, F. I.; Velez, N. R.; Thayer, R. C.; Patel, N. H.; Jones, M. A.; Meyers, G. F.; Minor, A. M., Gallium, Neon and Helium Focused Ion Beam Milling of Thin Films Demonstrated for Polymeric Materials: Study of Implantation Artifacts. *Nanoscale* **2019,** *11*, 1403–1409.

40. Orthacker, A.; Schmied, R.; Chernev, B.; Froch, J. E.; Winkler, R.; Hobisch, J.; Trimmel, G.; Plank, H., Chemical Degradation and Morphological Instabilities During Focused Ion Beam Prototyping of Polymers. *Physical Chemistry Chemical Physics* **2014,** *16*, 1658-1666.

41. Uchida, T.; Akamatu, H., Organic Semiconductors with High Conductivity. III. Perylene-Iodine Complex. *Bulletin of the Chemical Society of Japan* **1961,** *34*, 1015-1020.

42. Yao, Y.; Peng, S.-a.; Huang, X.-n.; Zhang, D.-y.; Shi, J.-y.; Jin, Z., A Uniform Stable P-type Graphene Doping Method with a Gold Etching Process. *Nanotechnology* **2019,** *30*, 405205/1-6.

43. Cho, J. H.; Kim, D. H.; Jang, Y.; Lee, W. H.; Ihm, K.; Han, J.-H.; Sukmin Chung; Cho, K., Effects of Metal Penetration into Organic Semiconductors on the Electrical Properties of Organic Thin Film Transistors. *Applied Physics Letters* **2006,** *89*, 132101/1-3.

44. Powell, R. C.; Soos, Z. G., Singlet exciton energy transfer in organic solids. *Journal of Luminescence* **1975,** *11*, 1-45.

45. Tomura, M.; Takahasi, Y., Migration of Excimer Energy in Pyrene Crystal. *Journal of the Physical Society of Japan* **1971,** *31*, 797 -801.

46. Gregg, B. A.; Sprague, J.; Peterson, M. W., Long-Rangle Singlet Energy Transfer in Perylene Bis(phenethylimide) Films. *Journal of Physical Chemistry B* **1997,** *101*, 5362-5369.

Chapter 4. Protection of Molecular Microcrystals by Encapsulation under Single Layer Graphene

In this chapter, we shift our focus on the crystal morphology from the bulk shape to the surface. By encapsulating the bulk crystal under an impermeable atomic carbon blanket—graphene, we successfully passivate the crystal surface, making the encapsulated crystal robust against harsh environment, such as organic solvent and high temperature.

Introduction

Two-dimensional (2D) materials have attracted attention from researchers due to their novel physical properties, like ultrahigh carrier mobilities, thermal conductivity, and mechanical toughness.[1-2] As a prototypical 2D material, graphene has been the subject of extensive study. This atomically thin membrane allows photons, electrons and even protons to pass through but is impermeable to other chemical species, even those as Small as atomic helium.[3-6] This impermeability has raised interest in the application of graphene as a protective coating, e.g. to prevent corrosion of an underlying metal.[7] Typically, these coatings consist of many overlapping flakes of graphene, so there is not complete encapsulation, but rather a slowing of the diffusion as the reactive species navigate around the sheets.

Reports of complete encapsulation of objects using graphene are relatively rare. Several groups have used graphene to encapsulate liquid samples for electron microscopy experiments [8-10], but these methods are challenging to implement, since they rely on using

a pair of sheets to sandwich a liquid droplet. Ideally one would develop a method whereby individual microscale objects on a solid support can be "shrink-wrapped" by an atomically thin sheet of graphene, making them impervious to chemical attack while still allowing optical and/or electrical access. The encapsulation of metal nanowires between graphene and plastic using hot lamination suggests that such an approach is feasible.[11] However, a more general encapsulation method using milder conditions on an inorganic surface would be desirable for organics. Ideally, the graphene would make an atomically tight seal with an inert substrate like glass.

Crystals composed of conjugated organic molecules make a good test system for graphene encapsulation. These crystals possess interesting electronic and photophysical properties[12], with those based on polycyclic aromatic hydrocarbons being of special interest.[13-14] They tend to be sensitive to the presence of impurities, like O_2 or organic contaminants, which can degrade their electronic properties. Organic crystals also dissolve when exposed to organic solvents and sublime away when exposed to high vacuum or elevated temperatures. Current protection strategies include isolating them under vacuum or an inert atmosphere and encapsulating them between glass plates sealed with epoxy. In both cases, the crystal becomes inaccessible to electrical or optical probes that require close sample contact, like scanning probe microscopies.

This chapter describes a method to encapsulate single microcrystals composed of the prototypical conjugated organic molecule perylene (PER) beneath monolayer graphene. While graphene has been used previously as a substrate for organic crystal growth[15-16], its

use as an encapsulation layer is relatively unexplored. We used PER as a test crystal because its α-polymorph tends to grow in a signature square shape and produces a strong visible photoluminescence signal. These characteristics allow us to optically detect the presence of these crystals underneath the graphene sheet and assess how they respond to solvent exposure and elevated temperatures. The effect of the graphene layer on the PER excimer dynamics can be measured by the photoluminescence (PL) decay. Our results demonstrate that a 2D monolayer can completely encapsulate a molecular crystal and turn it into a sample that is robust with respect to air and solvent exposure, as well as high temperatures. This new capability to protect fragile crystals should open the door to routine characterization of these fragile semiconductors using microscopy techniques with nanometer resolution[17], as well as new ways to interface them with other materials.

Results and Discussion

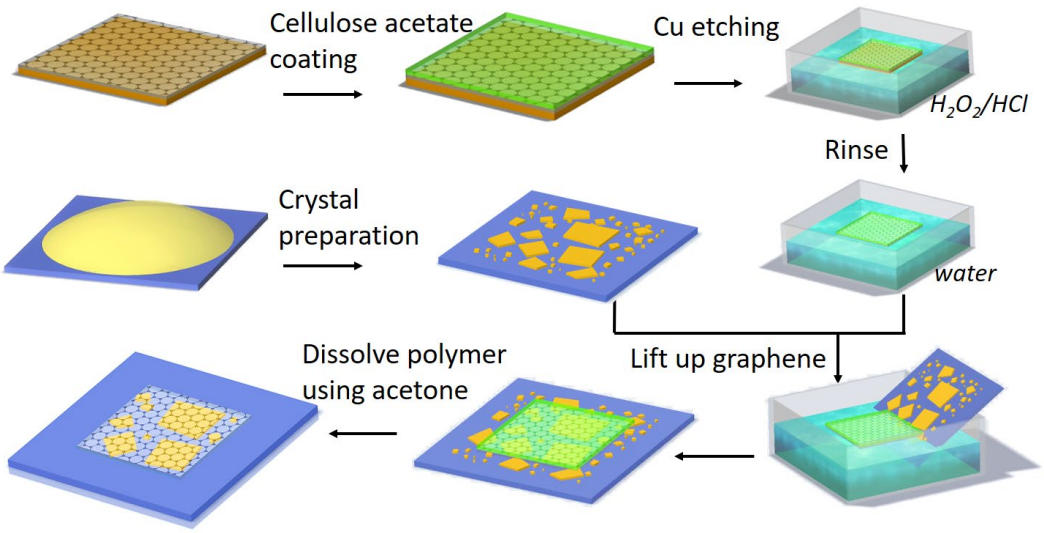

Figure 4.1. Schematic illustration of the graphene encapsulation process for molecular microcrystals.

The procedure for coating PER microcrystals with graphene is outlined in Figure 4.1 and described in detail in the Experimental chapter.[18] Briefly, large area single-layer graphene sheets grown on a Cu foil substrate by chemical vapor deposition are purchased from a commercial vendor. A several micron thick layer of cellulose acetate polymer is spin cast on top of the graphene, and then the Cu is dissolved using a solution of HCl/H_2O_2. After the Cu layer is completely etched away, the solution is replaced with clean water and the graphene-polymer layer is floated on the water surface. A glass substrate, on top of which random PER microcrystals have been grown by solvent evaporation, is then dipped into the water and positioned underneath the supported graphene. It is then lifted up with the graphene layer on top. The end result is a sample consisting of the glass substrate with PER crystals underneath a blanket of graphene with the polymer support layer on top. The final

step involves dissolving away the polymer supporting layer by rinsing with acetone. The presence of graphene can be readily discerned by its modified reflectivity, and it is easy to see breaks and holes in the coating. Most of the original PER microcrystals are dissolved away by the acetone rinse, but in regions containing intact graphene sheets, the underlying PER crystals can be readily imaged using optical, electron, and atomic force microscopy methods.

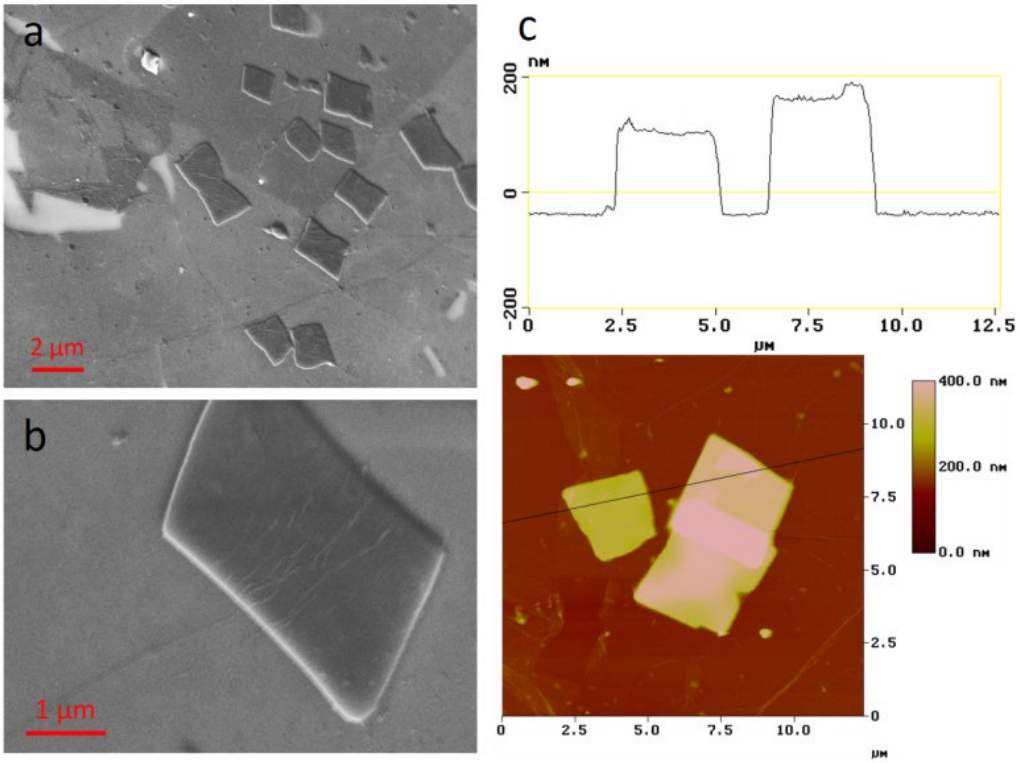

Figure 4.2. a), b) SEM images of graphene covered PER crystals on glass with low and high magnification. Note that the continuation of the graphene wrinkles from the substrate surface across the PER crystal in b) provides visual evidence the encapsulation. c) AFM image of graphene covered perylene crystals with cross section analysis. The typical diameter of the covered crystals is around 2 µm and the thickness is around 150 nm.

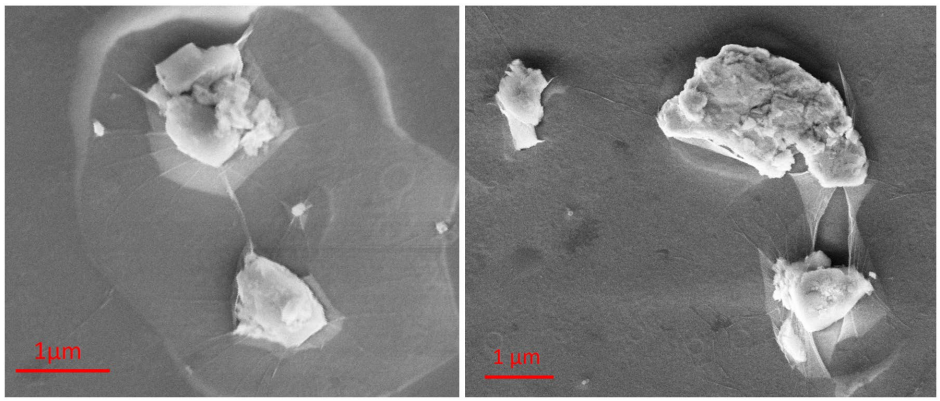

Figure 4.3. SEM images of graphene covering irregularly shaped debris particles. Note that the graphene is ruptured in the right-hand panel.

Figures 4.2a and 4.1.2b show SEM images of PER crystals under single-layer graphene. Note that this imaging was done without a metal coating, since graphene's high conductivity prevents charging of the low conductivity organic crystal and enables electron microscopy to be performed under vacuum without further treatment. In Figure 4.2b, one can see a wrinkle in the graphene sheet that continues from the substrate across the edge and onto the crystal surface. This wrinkling was the exception; in almost all other cases close adhesion of the graphene sheet to the crystal and glass surfaces led to a conformal coating. There is no sign of "tenting" in which the graphene sheet detaches from the surface and is free-floating between the crystal and surface. Tenting was observed for taller or more irregularly shaped objects, like inorganic dust particles that adhered to the substrate surface (Figure 4.3). The conformal nature of the encapsulation was confirmed using atomic force microscopy (AFM). Figure 4.2c shows an AFM image of a pair of encapsulated crystals, while Figure 4.2d shows the height profile of the crystals taken along the axis shown in Figure 4.2c. The profile image in Figure 4.2d illustrates the size variation in the PER crystal plates, which typically ranged from 100 to 200 nm thick. The images also show how the

graphene conforms to the crystal, following the sharp crystal edge down to the substrate surface.

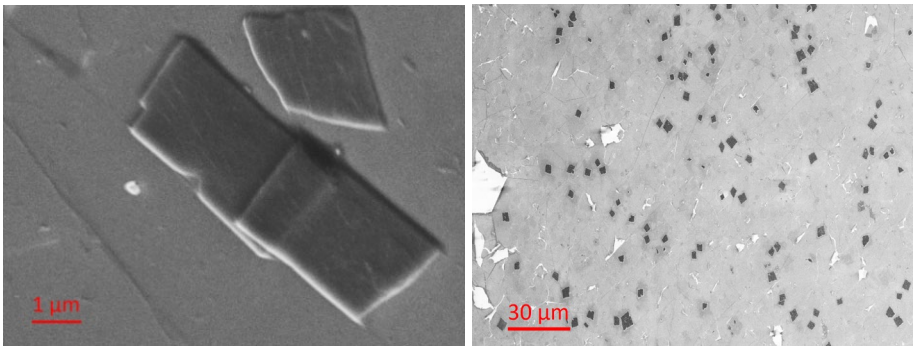

Figure 4.4. SEM images of graphene encapsulated perylene crystals. The crystals are black quadrilateral shapes in the right-hand panel. The gray area is the graphene sheet. The white area is the uncoated glass substrate.

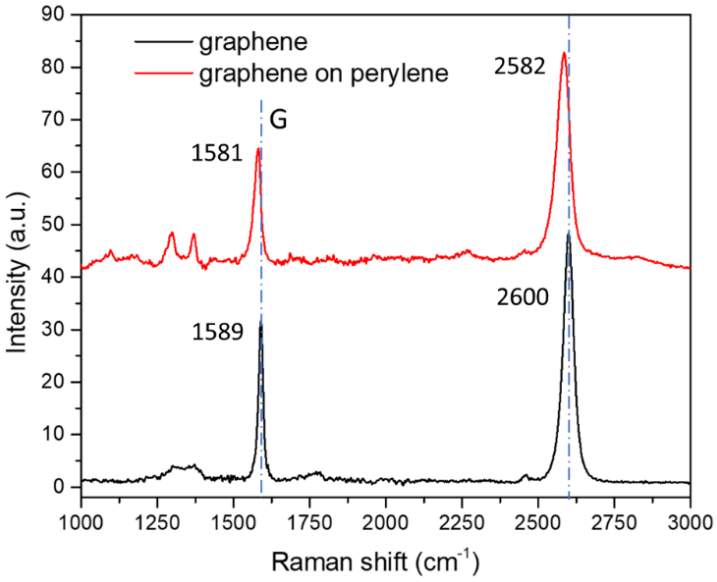

Figure 4.5. Raman spectra of graphene films on glass substrate (black) and on top of a PER crystal (red). The excitation wavelength is 780 nm. Both spectra show the characteristic graphene peaks: G- and 2D-peaks. Red shifts for both G (-8 cm^{-1}) and 2D (-18 cm^{-1}) peak are observed for the graphene on top of the PER crystal, along with additional peaks at 1297 cm^{-1} and 1369 cm^{-1} from the PER.

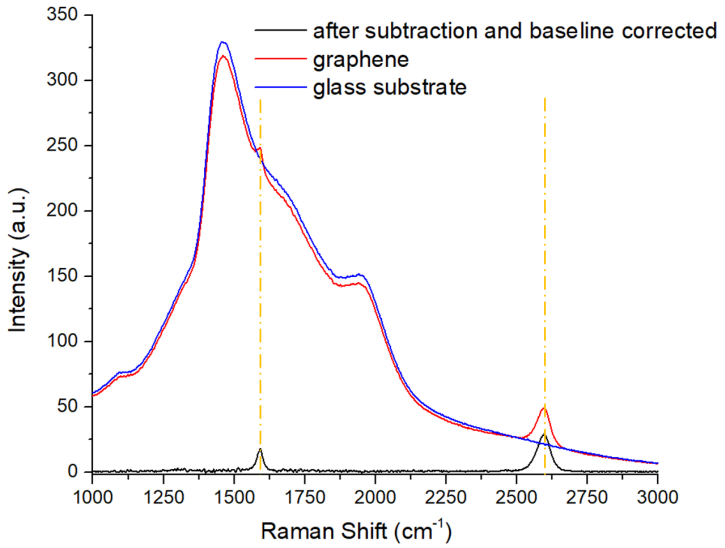

Figure 4.6. Raw Raman spectra of the graphene on the clean glass substrate with no PER (red) and the glass substrate by itself (blue). The excitation wavelength is 780 nm. The black line is the graphene spectrum after subtracting the glass spectrum and correcting the baseline. All measurements are collected under same conditions (laser power, exposure time and collection time). Subtraction and baseline correction do not affect the peak positions.

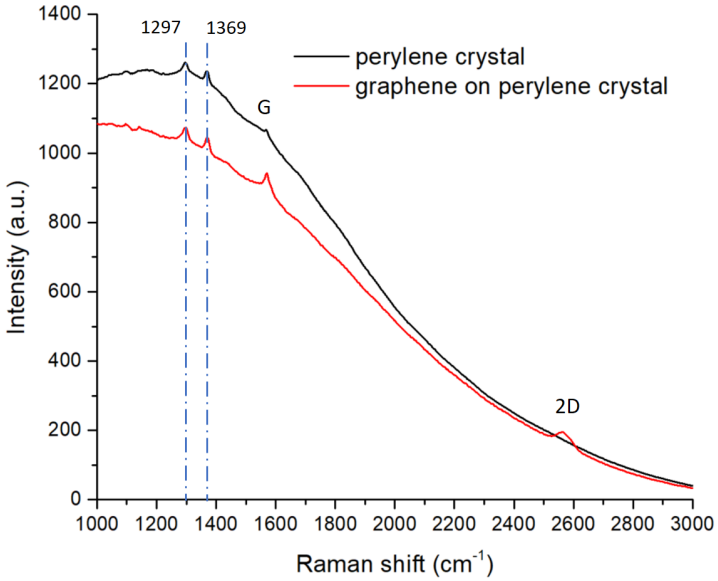

Figure 4.7. Raman spectra of a bare PER crystal (black) and a graphene-coated PER crystal (red). The extra peaks at 1297 cm^{-1} and 1369 cm^{-1} in the red spectrum as compared to the graphene spectra in Figure 4.5 are from the PER crystal underneath and correspond to in-plane C=C stretching frequencies of the PER aromatic rings.

Raman spectroscopy is a standard method to evaluate the quality of graphene layers.[19] Figure 4.5 compares the Raman spectra of graphene on top of both the SiO2 substrate and on top of a PER crystal. Both Raman spectra show the signature G peak in the range 1580-1590cm^{-1} and the 2D peak at around 2600 cm^{-1}. The G/2D peak intensity ratio ($I_G/I_{2D} < 1$) indicates monolayer coverage. The Small amplitude of the D peak at 1300 cm-1 for the graphene layer on SiO2 shows that it is largely free of defects.[19] The Raman spectrum on the PER does not appear to have an enhanced D peak intensity, suggesting that it has the same low defect level, but two additional peaks at 1297 and 1369 cm^{-1} also appear on top of this feature. These peaks are also prominent in the Raman spectrum of PER microcrystals (Figures 4.6 and 4.7) and originate from the PER double bond stretches.[20-21] It is interesting that the PER and graphene Raman signals are of comparable strength. The 780 nm excitation wavelength is far from the PER absorption at 500 nm but still resonant with the semi-metallic graphene. The very strong Raman signal of the delocalized electrons in graphene more than compensates for its lower mass fraction in this sample.

The exact positions of the G and 2D peaks can provide information about the state of the graphene. In pristine graphene the G peak is located at 1580 cm^{-1}. The G peak of our graphene on glass is located at 1589 cm^{-1}, consistent with doping by exposure to ambient O2 after preparation in air.[22-23] The Raman spectrum of graphene on top of PER exhibits a slight downshift in both the G (-8 cm^{-1}) and 2D (-18 cm^{-1}) peaks relative to those of graphene on SiO2. Larger PER crystals resulted in larger downshifts of the Raman peaks, with the largest crystal shifting the G peak all the way to 1570 cm^{-1} (Figure 4.8). These

larger G peak shifts were accompanied by larger 2D peak shifts, up to 25 cm^{-1}. These shifts were robust with respect to background subtraction and data reduction methods.

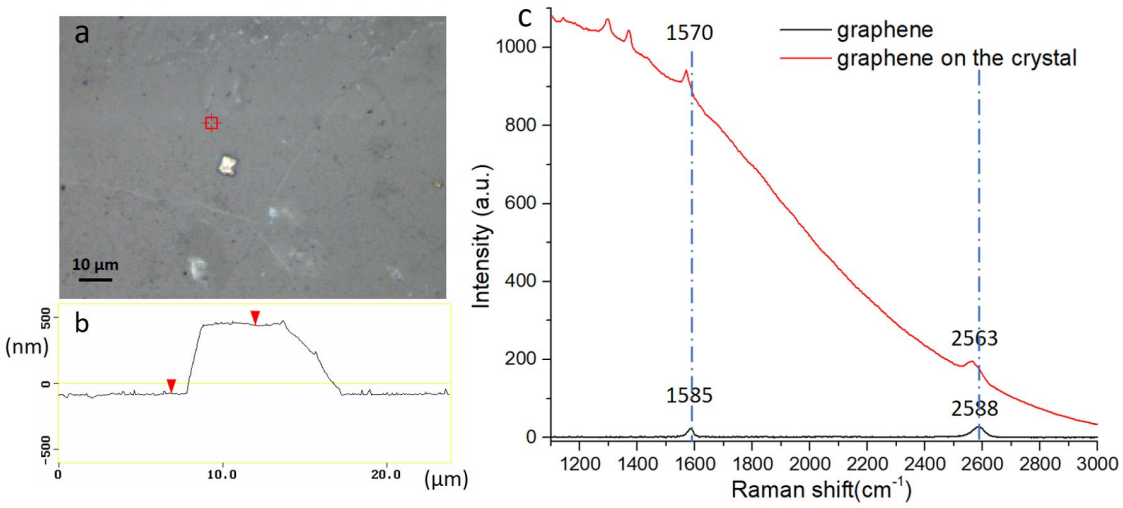

Figure 4.8. a) Optical microscopy image of a large (~6 μm diameter) PER crystal with graphene encapsulation. b) AFM cross section analysis shows that the crystal thickness is about 500 nm. c) Raman spectra of graphene films near the large PER crystal (black) and on the perylene crystal (red). Due to the fluorescence signal from PER crystal, the red spectrum still has a large background signal even after subtracting the glass substrate signal. However, the positions of G and 2D peaks are well-defined. The G peak is red-shifted 15 cm^{-1} to 1570 cm^{-1} and the 2D peak is shifted by 25 cm^{-1}. Note that the position of the graphene reference peaks (taken at a spot near the large crystal) are slightly different from those in Figure 4.3 in the text. This may reflect lower doping levels for this sample, or some local strain due to the presence of large crystal about 10 microns away.

There are several factors that can lead to shifting Raman peaks in graphene. Both n- and p-doping typically lead to an upshift of the G band Raman frequencies[24], but this is the opposite of what we observe. Given that the graphene sheet is already p-doped due to oxygen exposure, one possibility is that the organic crystal removes charge carriers or O_2 from the graphene sheets. Such an undoping process would be expected to shift the G peak back to 1580 cm^{-1}, but not below. The fact that we observe shifts of both G and 2D peaks to positions well below those of pristine graphene suggests that the more likely culprit is

strain as the graphene stretches to accommodate the underlying crystal. The shifts in both G and 2D peaks are consistent with a strain of approximately 0.5% on a crystal with the thickness about 150 nm, based on previous measurements on stretched sheets of graphene.[25-26] This stretching would explain the conformal nature of the coating deduced from the images in Figure 4.2 and is consistent with the "shrink-wrap" concept. The Raman shifts provide evidence that the interaction of graphene with the underlying crystal induces a slight stretching but no dramatic changes in electronic structure or defect density. It is possible, however, that the graphene sheet experiences higher localized strain at the crystal edges, which could lead to larger effects on its electronic properties.[27]

PER is a highly soluble Small molecule that sublimes easily, but the graphene-glass encapsulation stabilizes the microcrystals under a variety of conditions. The samples can be left on the benchtop, under room light, for days without any change in PL brightness. The encapsulated crystals survive immersion in a variety of organic solvents (acetone, tetrahydrofuran, toluene, methanol and methylene chloride) for more than 1 day without change. Unprotected crystals dissolved within 1 min under the same conditions. When heated to 100°C in air, unprotected crystals sublimed away within 40 min, but encapsulated crystals resisted sublimation up to 250°C, close to PER's melting point of 278°C. At higher temperatures, the PER melted and then rapidly disappeared. Comparisons of graphene-protected and unprotected PER crystals after exposure to solvent and elevated temperatures are shown in Figure 4.9. The fact that the graphene sheet provides protection from solvent dissolution and sublimation is evidence that the graphene makes an atomically tight seal with the glass substrate that completely prevents penetration by solvent molecules as well

as escape of the PER molecules at elevated temperatures. The encapsulation only failed when the PER itself could diffuse (after melting) or if the graphene did not remain intact. Objects with large height variations tended to rupture the graphene (Figure 4.3), allowing solvent penetration and dissolution.

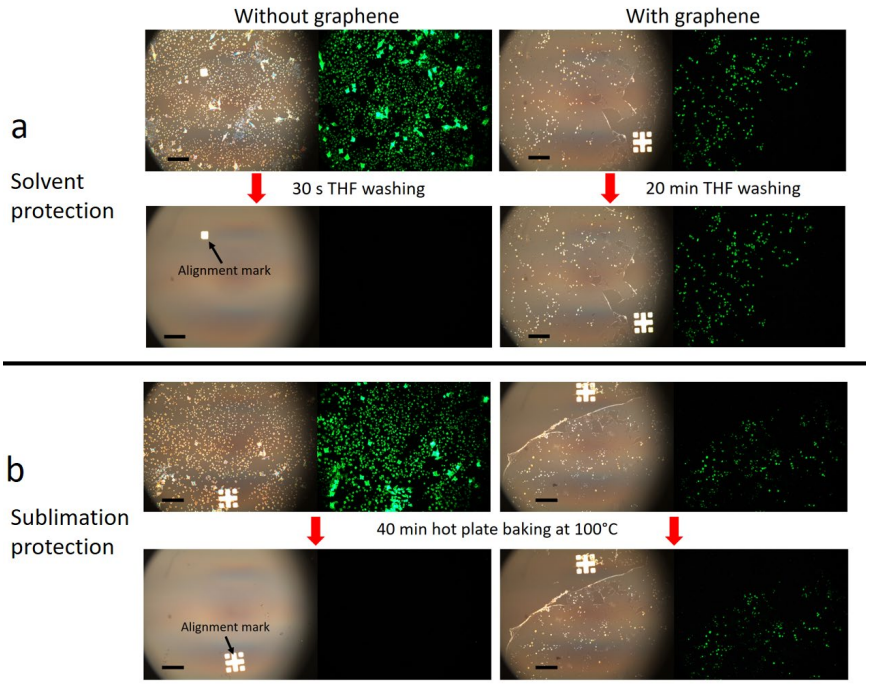

Figure 4.9. Transmitted and fluorescence microscopy images showing the effect of monolayer graphene encapsulation on the stability of PER microcrystals. The substrates are standard microscope slides with gold alignment marks. a) Before and after washing with THF. 30s washing resulted in 100% dissolution of unprotected crystals, while 20-min THF washing had no effect on protected crystals. b) Before and after heating at 100°C for 40 min. The unprotected crystals sublime completely but the protected crystals remain intact. Scale bars = 50 µm.

Graphene is not a completely inert coating, since it is a semimetal that may be expected to affect the electronic properties of the crystal. For example, it is likely to quench molecular excitons due to either energy[28-30] or electron transfer.[31-32] Although the precise distance dependence and mechanism of the PL quenching remain a subject of active investigation, the characteristic distance has been estimated to extend up to 60 nm.[33] To investigate the

possibility of PL quenching, the excimer lifetime of the PER microcrystals was measured using time-resolved PL experiments. The PL spectra with and without graphene encapsulation are similar, showing the Y (550 nm) and E (600 nm) peaks as observed in α-PER crystals (Figure 4.10).[34] The Y peak in our samples is more pronounced than for typical bulk crystals[35-36], as often observed for nanocrystalline samples with higher defect densities.[37-38]

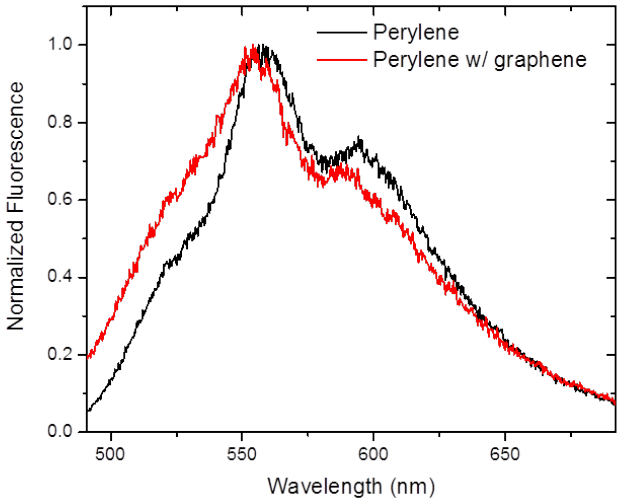

Figure 4.10. PL spectra of PER (black) and PER coated by graphene (red) integrated over a 100 ns time window. Both Y (~550 nm) and E (~600 nm) peaks are present in both samples at comparable intensities. The Small shifts in peak positions between PER and graphene-coated PER (from 558 nm to 555 nm and from 595 nm to 590 nm) probably result from Small alignment changes before the streak camera monochromator.

The PL decays of the two samples are identical, as shown in Figure 4.11a, although the signal level of the encapsulated sample is considerably lower due to the scarcity of surviving crystals. We note that these PER crystals grown from solution, have a more rapid PL decay than sublimation grown crystals from zone-refined PER.[34] It is likely that the PL decay is accelerated by the presence of defects in our solution-grown PER crystals. But the important point is that there is no detectable PL quenching by the graphene overlayer.

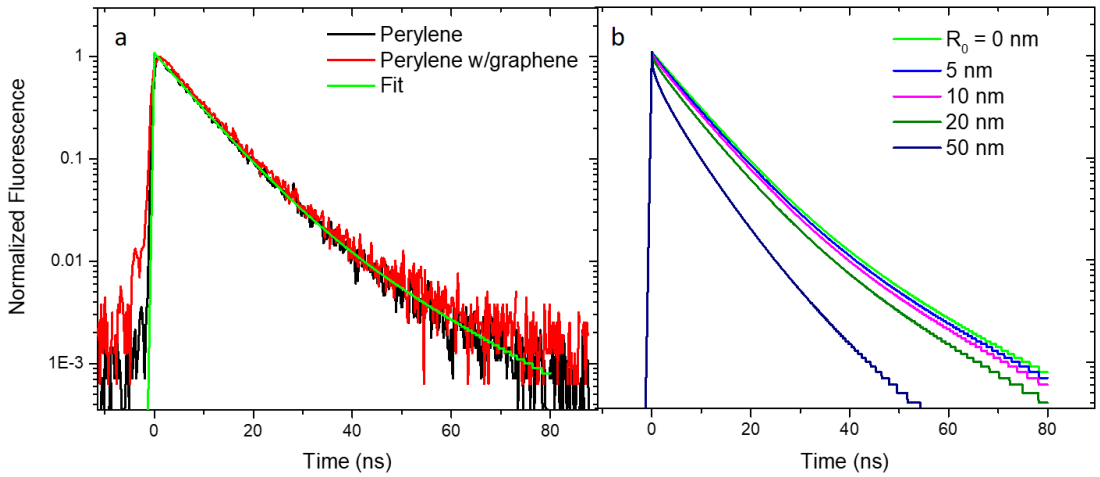

Figure 4.11. a) Time-resolved photoluminescence of PER (black) and graphene-coated PER crystals (red) excited at 400nm. The lifetime of crystalline PER is unchanged when coated with graphene. b) Calculated PL decays for different R0 values for the graphene quenching function described in the text for a 150 nm thick crystal. When R0≥20 nm, there is a noticeable deviation from the intrinsic PER decay.

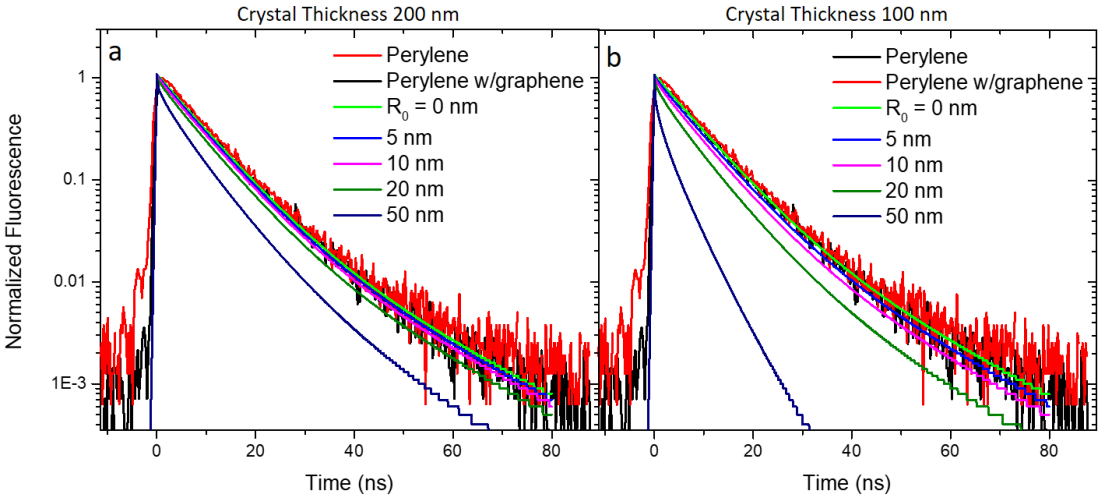

Figure 4.12. PL decays of PER microcrystals (black) and graphene-coated PER microcrystals (red), along with calculated decays for 200 nm (a) and 100 nm (b) crystal thicknesses. A MATLAB program was used to numerically calculate the quenching effect as *R* is increased. This was done using the following equation: $PL(t,k) \approx [A_1 e^{\frac{-(t-t_0)}{\tau_1} - \left(\frac{k}{R0}\right)^{-4} * t} + A_2 e^{\frac{-(t-t_0)}{\tau_1} - \left(\frac{k}{R0}\right)^{-4} * t}]$. Here k is the distance from the graphene quenching layer and is iterated from 0 to L, the crystal thickness. The plotted PL decays are obtained from the following equation: $PL_{tot}(t) = \frac{1}{L} * \sum_{k=0}^{L} PL(t,k)$. It can be seen that the quenching effect becomes more pronounced as R_0 is increased and L is decreased.

Even though there is no detectable change in the PL decay, it is likely that excitons near the top surface of the crystal, near the graphene layer, are quenched. We can place an approximate upper bound on the quenching radius of the graphene by using a simple model to analyze the PL decay. We assume an average crystal thickness of 150 nm and that the quenching rate of the 2D graphene sheet is given by $k_{quench} = \frac{R_0^4}{R^4}$, where R_0 is the critical distance for a dipole interacting with a 2D energy acceptor.[39-40] The experimental PL decay is parameterized as a biexponential with amplitudes $A_1 = 0.925$ and $A_2 = 0.075$ and decay times $\tau_1 = 7.5$ ns and $\tau_2 = 17.4$ ns. The functional form of the PL decay is then the product of the intrinsic biexponential and the quenching term,

$$PL(t) \approx [A_1 e^{-\frac{t}{\tau_1}} + A_2 e^{-\frac{t}{\tau_1}}] \times e^{-k_{quench} t} \quad (1)$$

In Figure 4.11b, we compare the PL decays calculated assuming different values of R_0 and summing up the contributions of Equation (1) for all R values in a 150 nm thick crystal. For R_0=20 nm, the deviation of the calculated decay from the intrinsic decay should be observable. Similar results are obtained for crystal thicknesses of 100 nm and 200 nm (Figure 4.12). The fact that this deviation is not experimentally observed allows us to estimate a conservative upper bound of $R_0 \leq 20$ nm. This limit is consistent with a value of $R_0 \sim 10$ nm extracted from distance-dependent quenching of a Rhodamine dye on top of graphene[41] and suggests that only excitons in the top layer of the PER crystal are quenched by the graphene.

The ability to observe electronic perturbations due to graphene will depend on the nature of the organic sample. In PER, the effect of the graphene quenching may be more easily observed for thinner crystals that have a larger fraction of molecules close to the surface, or for higher quality crystals that can support longer exciton diffusion lengths. Different types of crystals may have significant electronic interactions with the graphene layer, for example charge transfer. Surface sensitive measurements of the electronic properties will likely be sensitive to the graphene-organic interaction. A second issue is that the method of preparation exposes the sample to water during the graphene lift up. While the graphene clearly prevents access by molecules outside the encapsulation layer, it can also trap impurities or water molecules inside the layer with the crystal. The stability of the graphene encapsulated sample will allow such effects to be studied for samples that might be sensitive to the presence of such extrinsic chemical species.

Conclusions

In summary, we have demonstrated that it is possible to create robust molecular crystal samples that are fully encapsulated beneath a monolayer of graphene. The graphene layer provides complete protection from a variety of solvents and prevents sublimation of the crystal at elevated temperatures. Raman measurements show that the graphene layer is only slightly perturbed by the underlying crystal, while time-resolved PL measurements show no detectable quenching of the PER excimers by the graphene. The fact that graphene can make a tight seal with glass suggests that this method can be extended to other 2D encapsulating materials, for example hexagonal boron nitride, whose large bandgap would preclude any possibility of energy transfer. This technique may also make it possible to

interface organic crystals with other materials that have incompatible processing conditions, like metal electrodes created by focused ion beam deposition under high vacuum or polymers cast from solvents that would normally dissolve the crystal. The ability to keep organic solids crystal intact under such processing conditions raises the possibility of fabricating an organic-organic heterojunction to study energy and/or charge transfer across a 2D membrane.

References

1. Novoselov, K. S.; Fal'ko, V. I.; Colombo, L.; Gellert, P. R.; Schwab, M. G.; Kim, K., A Roadmap for Graphene. *Nature* **2012,** *490*, 192-200.

2. Butler, S. Z.; Hollen, S. M.; Cao, L.; Cui, Y.; Gupta, J. A.; Gutierrez, H. R.; Heinz, T. F.; Hong, S. S.; Huang, J.; Ismach, A. F.; Johnston-Halperin, E.; Kuno, M.; Plashnitsa, V. V.; Robinson, R. D.; Ruoff, R. S.; Salahuddin, S.; Shan, J.; Shi, L.; Spencer, M. G.; Terrones, M.; Windl, W.; Goldberger, J. E., Progress, Challenges, and Opportunities in Two-Dimensional Materials Beyond Graphene. *ACS Nano* **2013,** *7*, 2898–2926.

3. Bunch, J. S.; Verbridge, S. S.; Alden, J. S.; Zande, A. M. v. d.; Parpia, J. M.; Craighead, H. G.; McEuen, P. L., Impermeable Atomic Membranes from Graphene Sheets. *Nano Letters* **2008,** *8*, 2458-2462.

4. Berry, V., Impermeability of Graphene and its Applications. *Carbon* **2013,** *62*, 1-10.

5. Hu, S.; Lozada-Hidalgo, M.; Wang, F. C.; Mishchenko, A.; Schedin, F.; Nair, R. R.; W.Hill, E.; Boukhvalov, D. W.; Katsnelson, M. I.; Dryfe, R. A. W.; Grigorieva, I. V.; Wu, H. A.; Geim, A. K., Proton Transport through One-Atom-Thick Crystals. *Nature* **2014,** *516*, 227-230.

6. Kaplan, A.; Yuan, Z.; Benck, J. D.; Rajan, A. G.; Chu, X. S.; Wang, Q. H.; Strano, M. S., Current and Future Directions in Electron Transfer Chemistry of Graphene. *Chemical Society Reviews* **2017,** *46*, 4530--4571.

7. Nine, M. J.; Cole, M. A.; Tran, D. N. H.; Losic, D., Graphene: a Multipurpose Material for Protective Coatings. *Journal of Materials Chemistry A* **2015,** *3*, 12580–12602.

8. Mohanty, N.; Fahrenholtz, M.; Nagaraja, A.; Boyle, D.; Berry, V., Impermeable Graphenic Encasement of Bacteria. *Nano Letters* **2011,** *11*, 1270–1275.

9. Yuk, J. M.; Park, J.; Ercius, P.; Kim, K.; Hellebusch, D. J.; Crommie, M. F.; Lee, J. Y.; Zettl, A.; Alivisatos, A. P., High-Resolution EM of Colloidal Nanocrystal Growth Using Graphene Liquid Cells. *Science* **2012,** *336*, 61-64.

10. Chen, Q.; Smith, J. M.; Park, J.; Kim, K.; Ho, D.; Rasool, H. I.; Zettl, A.; Alivisatos, A. P., 3D Motion of DNA-Au Nanoconjugates in Graphene Liquid Cell Electron Microscopy. *Nano Letters* **2013,** *13*, 4556−4561.

11. Deng, B.; Hsu, P.-C.; Chen, G.; Chandrashekar, B. N.; Liao, L.; Ayitimuda, Z.; Wu, J.; Guo, Y.; Lin, L.; Zhou, Y.; Aisijiang, M.; Xie, Q.; Cui, Y.; Liu, Z.; Peng, H., Roll-to-Roll Encapsulation of Metal Nanowires between Graphene and Plastic Substrate for High-Performance Flexible Transparent Electrodes. *Nano Letters* **2015,** *15*, 4206-4213.

12. Podzorov, V., *Organic Single Crystals (Special Issue)*. 2013; Vol. 38.

13. Anthony, J. E., The Larger Acenes: Versatile Organic Semiconductors. *Angewandte Chemie International Edition* **2008,** *47*, 452 – 483.

14. Rieger, R.; Mullen, K., Forever Young: Polycyclic Aromatic Hydrocarbons as Model Cases for Structural and Optical Studies. *Journal of Physical Organic Chemistry* **2010,** *23*, 315-325.

15. Lee, C.-H.; Schiros, T.; Santos, E. J. G.; Kim, B.; Yager, K. G.; Kang, S. J.; Lee, S.; Yu, J.; Watanabe, K.; Taniguchi, T.; James Hone ; Kaxiras, E.; Nuckolls, C.; Kim, P., Epitaxial Growth of Molecular Crystals on van der Waals Substrates for High-Performance Organic Electronics. *Advanced Materials* **2014,** *26*, 2812-2817.

16. Zhang, Y.; Diao, Y.; Lee, H.; Mirabito, T. J.; Johnson, R. W.; Puodziukynaite, E.; John, J.; Carter, K. R.; Emrick, T.; Mannsfeld, S. C. B.; Briseno, A. L., Intrinsic and Extrinsic Parameters for Controlling the Growth of Organic Single-Crystalline Nanopillars in Photovoltaics. *Nano Letters* **2014,** *14*, 5547-5554.

17. Schuck, P. J.; Weber-Bargioni, A.; Ashby, P. D.; Ogletree, D. F.; Schwartzberg, A.; Cabrini, S., Life Beyond Diffraction: Opening New Routes to Materials Characterization with Next-Generation Near-Field Approaches. *Advanced Functional Materials* **2013,** *23*, 2539-2553.

18. Chen, M.; Li, G.; Li, W.; Stekovic, D.; Arkook, B.; Itkis, M. E.; Pekker, A.; Bekyarova, E.; Haddon, R. C., Large-Scale Cellulose-Assisted Transfer of Graphene Toward Industrial Applications. *Carbon* **2016,** *110*, 286-291.

19. Ferrari, A. C.; Basko, D. M., Raman Spectroscopy as a Versatile Tool for Studying the Properties of Graphene. *Nature Nanotechnology* **2013,** *8*, 235-246.

20. Matsunuma, S.; Akamatsu, N.; Kamisuki, T.; Adachi, Y.; Maeda, S.; Hirose, C., S_n<-- S_1 and S_1-->S_0 Resonance CARS Spectra of Perylene in the S_1 State. *Journal of Chemical Physics* **1988,** *88*, 2956-2961.

21. Shinohara, H.; Yamakita, Y.; Ohno, K., Raman Spectra of Polycyclic Aromatic Hydrocarbons. Comparison of Calculated Raman Intensity Distributions with Observed Spectra for Naphthalene, Anthracene, Pyrene, and Perylene. *Journal of Molecular Structure* **1998,** *442*, 221-234.

22. Ryu, S.; Liu, L.; Berciaud, S.; Yu, Y. J.; Liu, H.; Kim, P.; Flynn, G. W.; Brus, L. E., Atmospheric Oxygen Binding and Hole Doping in Deformed Graphene on a SiO_2 Substrate. *Nano Letters* **2010,** *10*, 4944-4951.

23. Piazza, A.; Giannazzo, F.; Buscarino, G.; Fisichella, G.; Magna, A. L.; Roccaforte, F.; Cannas, M.; Gelardi, F. M.; Agnello, S., Effect of Air on Oxygen p-Doped Graphene on SiO_2. *Physica Status Solidi A* **2016,** *213*, 2341-2344.

24. Das, A.; Pisana, S.; Chakraborty, B.; Piscanec, S.; Saha, S. K.; Waghmare, U. V.; Novoselov, K. S.; Krishnamurthy, H. R.; Geim, A. K.; Ferrari, A. C.; Sood, A. K., Monitoring Dopants by Raman Scattering in an Electrochemically Top-Gated Graphene Transistor. *Nature Nanotechnology* **2008,** *3*, 210-215.

25. Huang, M.; Yan, H.; Chen, C.; Song, D.; Heinz, T. F.; Hone, J., Phonon Softening and Crystallographic Orientation of Strained Graphene Studied by Raman Spectroscopy. *Proceedings of the National Academy of Sciences* **2009,** *106*, 7304-7308.

26. Corro, E. D.; Taravillo, M.; Baonza, V. G., Nonlinear Strain Effects in Double-Resonance Raman Bands of Graphite, Graphene, and Related Materials. *Physical Review B* **2012,** *85*, 033407/1-5.

27. Wu, Y.; Zhai, D.; Pan, C.; Cheng, B.; Taniguchi, T.; Watanabe, K.; Sandler, N.; Bockrath, M., Quantum Wires and Waveguides Formed in Graphene by Strain. *Nano Letters* **2017,** *18*, 64-69.

28. Kasry, A.; Ardakani, A. A.; Tulevski, G. S.; Menges, B.; Copel, M.; Vyklicky, L., Highly Efficient Fluorescence Quenching with Graphene. *Journal of Physical Chemistry C* **2012,** *116*, 2858−2862.

29. Ajayi, O. A.; Anderson, N. C.; Cotlet, M.; Petrone, N.; Gu, T.; Wolcott, A.; Gesuele, F.; Hone, J.; Owen, J. S.; Wong, C. W., Time-Resolved Energy Transfer from Single Chloride-Terminated Nanocrystals to Graphene. *Applied Physics Letters* **2014,** *104*, 171101/1-5.

30. Raja, A.; Montoya-Castillo, A.; Zultak, J.; Zhang, X.-X.; Ye, Z.; Roquelet, C.; Chenet, D. A.; Zande, A. M. v. d.; Huang, P.; Jockusch, S.; Hone, J.; Reichman, D. R.; Brus, L. E.; Heinz, T. F., Energy Transfer from Quantum Dots to Graphene and MoS_2: The Role of Absorption and Screening in Two-Dimensional Materials. *Nano Letters* **2016,** *16*, 2328-2333.

31. Liu, Y.; Liu, C. Y.; Liu, Y., Investigation on Fluorescence Quenching of Dyes by Graphite Oxide and Graphene. *Applied Surface Science* **2011,** *257*, 5513–5518.

32. Kim, H.-J.; Sung, J.; Chung, H.; Choi, Y. J.; Kim, D. Y.; Kim, D., Covalently Functionalized Graphene Composites: Mechanistic Study of Interfacial Fluorescence Quenching and Recovery Processes. *Journal of Physical Chemistry C* **2015,** *119*, 11327−11336.

33. Goncalves, H.; Bernardo, C.; Moura, C.; Ferreira, R. A. S.; Andre, P. S.; Stauber, T.; Belsley, M.; Schellenberg, P., Long Range Energy Transfer in Graphene Hybrid Structures. *Journal of Physics D* **2016,** *49*, 3315102/1-6.

34. Walker, B.; Port, H.; Wolf, H. C., The Two-Step Excimer Formation in Perylene Crystals. *Chemical Physics* **1985,** *92*, 177-185.

35. Nishimura, H.; Yamaoka, T.; Mizuno, K.; Iemura, M.; Matsui, A., Luminescence of Free and Self-trapped Excitons in α and β-Perylene Crystals. *Journal of the Physical Society of Japan* **1984,** *53*, 3999-4008.

36. Pick, A.; Klues, M.; Rinn, A.; Harms, K.; Chatterjee, S.; Witte, G., Polymorph-Selective Preparation and Structural Characterization of Perylene Single Crystals. *Crystal Growth & Design* **2015,** *15*, 5495-5504.

37. Fujino, T.; Tahara, T., Femtosecond Fluorescence Up-Conversion Microscopy: Exciton Dynamics in α-Perylene Microcrystal. *Journal of Physical Chemistry B* **2003,** *107*, 5120-5122.

38. Ishino, H.; Iwai, S.; Iwamoto, S.; Okumura, T.; Nishimoto, T.; Nair, S. V.; Kobayashi, T.; Tokunaga, E., Absorption and Emission Spectra of Molecular Excitons in Single Perylene Nanocrystals. *Physical Review B* **2011,** *84*, 041303/1-4.

39. Swathi, R. S.; Sebastian, K. L., Long Range Resonance Energy Transfer from a Dye Molecule to Graphene has (Distance)$^{-4}$ Dependence. *Journal of Chemical Physics* **2009,** *130*, 086101/1-3.

40. Wang, Y.; Kurunthu, D.; Scott, G. W.; Bardeen, C. J., Fluorescence Quenching in Conjugated Polymers Blended with Reduced Graphitic Oxide. *Journal of Physical Chemistry C* **2010,** *114*, 4153–4159.

41. Gaudreau, L.; Tielrooij, K. J.; Prawiroatmodjo, G. E. D. K.; Osmond, J.; Abajo, F. J. G. d.; Koppens, F. H. L., Universal Distance-Scaling of Nonradiative Energy Transfer to Graphene. *Nano Letters* **2013,** *13*, 2030-2035.

Chapter 5. Hexagonal Boron Nitride Encapsulation of Organic Microcrystals and Energy Transfer Dynamics

In this chapter, in order to minimize the quenching effect at the interface between the protective layer and PAHs, graphene is replaced with insulating few-layer h-BNs as the encapsulating layer for molecular crystals. The energy transfer dynamics at the PAH/graphene as well as PAH/hBN interfaces are further studied and compared.

Introduction

Two dimensional (2D) materials like graphene are an area of intense research interest due to their unique electronic, mechanical, and optical properties.[1-2] In addition to their intrinsic properties, 2D materials can be combined with other materials to function as ultrathin membranes that can be either permeable or impermeable.[3-7] As an example of the application of impermeable membranes, monolayer graphene has been used as a conformal coating to encapsulate and protect nanowires[8], perovskites[9], other 2D layers[10], and single organic microcrystals.[11] This conductive coating enabled the crystals to be visualized directly using electron microscopy, protected them from solvent attack, and prevented sublimation at elevated temperatures. In principle, the single atom thick coating would enable routine characterization of exciton dynamics in the crystal using near-field optical and scanning probe microscopy techniques under ambient conditions. Graphene encapsulation, however, has one major drawback: as a semi-metal, graphene is expected to perturb the electronic states and photophysical behavior of the underlying crystal, at least near the surface.

If our goal is to study the intrinsic exciton dynamics of an organic crystal, an electronically inert coating must be used. Hexagonal boron nitride (h-BN) is a 2D material whose large bandgap (>5 eV)[12] should allow easy optical access while avoiding energy and electron transfer processes that can quench electronic excited states. It has been used successfully to encapsulate and protect other 2D materials[13-15], metal surfaces[16], and layered perovskites.[17]

However, h-BN's weaker mechanical properties and higher propensity to fracture[18-19] make it more challenging to use it to encapsulate a 3-dimensional object like a molecular crystal. We were not sure whether h-BN's susceptibility to structural defects and fracture during the encapsulation process would prevent its use for protective encapsulation of single crystals.

In this chapter, we examine the ability of different h-BN samples to cover single perylene (PER) microcrystals. We characterize the sample morphology and chemical stability using electron, optical, and atomic force microscopies. To determine the interaction of the 2D material with the underlying organic chromophores, a polymer film assay is used to characterize the fluorescence quenching ability of both graphene and h-BN. The most surprising result is that solution-transferred h-BN is not photophysically inert but instead has an effective Forster quenching radius of 2.9 nm, as compared to 14.6 nm for graphene. However, the fluorescence quenching can be completely avoided by using dry transfer methods. Both the source of h-BN and its method of transfer determine its ability to act as an inert coating and avoid fluorescence quenching. Encapsulation of organic solids using

multi-layer h-BN is feasible, but attention must be paid to preparation conditions and the nature of the h-BN sample.

Results and Discussion

Plate-like PER microcrystals in the α crystal polymorph form[20], grown by solvent evaporation on a glass substrate, have been previously shown to be amenable to graphene encapsulation. The crystals were encapsulated under h-BN using the same wet transfer process developed in our previous paper.[11] When this method was used for CVD-grown graphene, a high yield of encapsulated PER microcrystals was obtained. But when used for the CVD-grown monolayer and bilayer h-BN, no PER crystals survived after exposure to acetone. Optical microscopy revealed that h-BN layers were present on the glass slide, but they could not prevent dissolution of the organic crystals, suggesting that they had a high density of holes that allowed the solvent to penetrate.

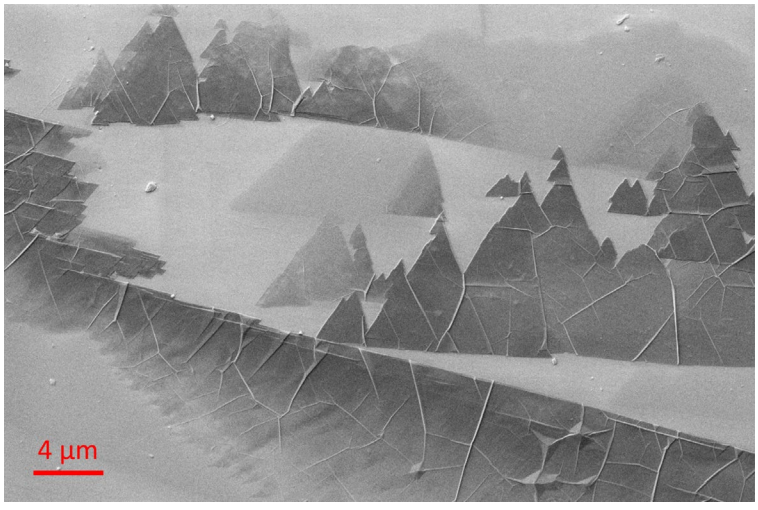

Figure 5.1. SEM of h-BN layers on a glass substrate without any metal coating.

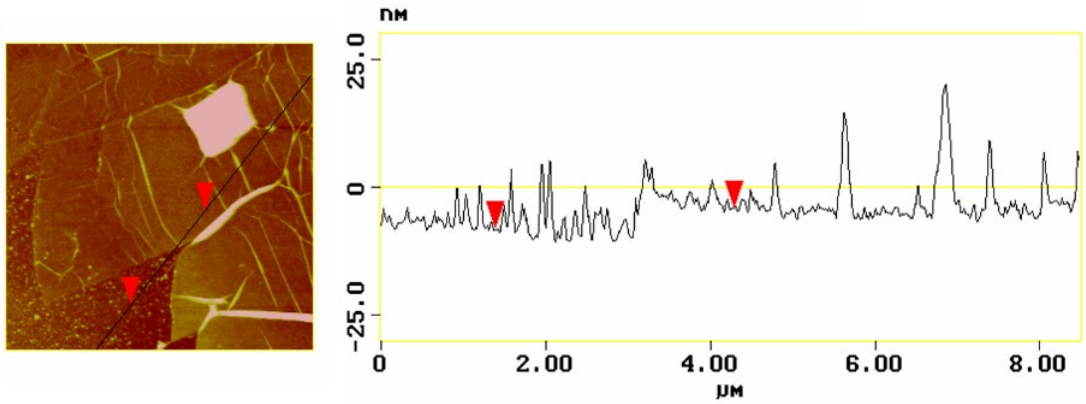

Figure 5.2. AFM image and scan profile of transferred MBE-grown h-BN is around 4 nm, corresponding to 10 layers of h-BN.

In order to determine whether different forms of h-BN could be used in the wet-transfer encapsulation process, we turned to multilayer h-BN grown by molecular beam epitaxy (MBE) onto a metal foil. These h-BN samples have been shown to cover large areas with mechanically intact h-BN up to 10 layers thick (Figures 5.1 and 5.2).[21] Using this MBE-grown h-BN and the same wet transfer method, we could demonstrate successful encapsulation. Figure 5.3 summarizes the results of this series of experiments. The square PER crystals can be directly imaged using SEM without a conductive coating. Similar to graphene, the high carrier mobility in h-BN prevents surface charge build up in the low-conductivity organic at low electron beam voltages (< 5 kV).[11] Also similar to graphene, AFM images reveal that the h-BN adheres as a conformal coating, with the sharp edges of the underlying crystal clearly visible. The ability of h-BN to conformally encapsulate the PER crystals was somewhat surprising in light of the fact that the MBE-grown h-BN has multiple layers, which would tend to reduce its flexibility.[18]

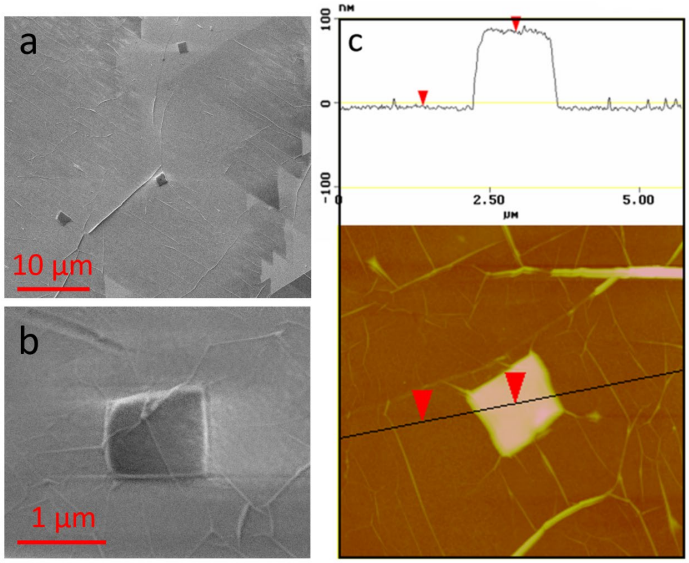

Figure 5.3. Characterization of MBE-grown h-BN encapsulated PER crystals. a) SEM image of multiple PER crystals (dark spots) under h-BN; b) SEM image of single PER crystal showing wrinkles in h-BN layer; c) AFM scanning image and cross-section of a single encapsulated PER crystal, also showing the wrinkles of the h-BN layer that extend onto the top of the crystal. The typical crystal size is around 2 μm^2 with 100 nm height.

Successful encapsulation was confirmed by the fact that the encapsulated PER crystals were unaffected by solvent exposure or elevated temperatures. Figure 5.4 shows fluorescence microscopy images of PER microcrystals that have been encapsulated under MBE-grown h-BN. Neither immersion in tetrahydrofuran for 30 minutes, nor heating to 140ºC in air had a noticeable effect on the PER fluorescence intensity. Without encapsulation, the microcrystals vanished within 5 minutes under the same conditions. These measurements confirm that MBE-grown h-BN can function as a protective covering for the organic crystals, similar to monolayer graphene. The main difference is that the yield of encapsulated crystals is about 95% lower than that for CVD-grown monolayer graphene, possibly due to a larger number of holes resulting from defects and/or fracture during the transfer process.

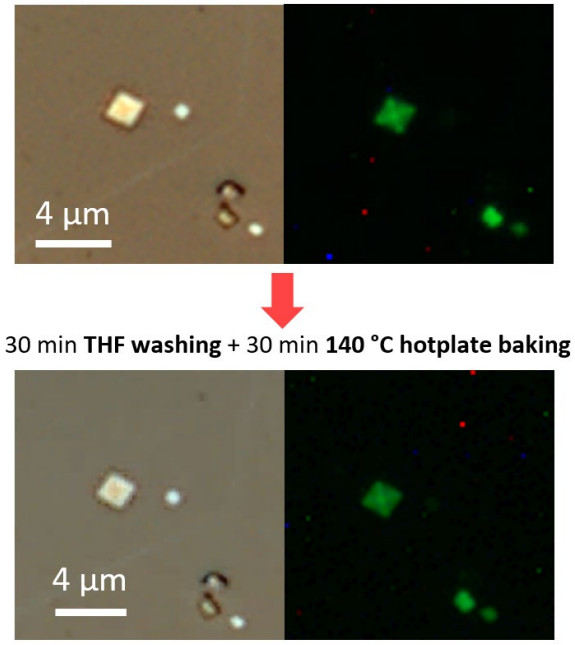

Figure 5.4. Reflectance and fluorescence microscopy images showing how encapsulation by MBE-grown h-BN enhances the stability of PER microcrystals. Encapsulated crystals can survive 30-minute THF bath washing plus 30-minute hotplate baking at 140 °C without significant loss of fluorescence intensity.

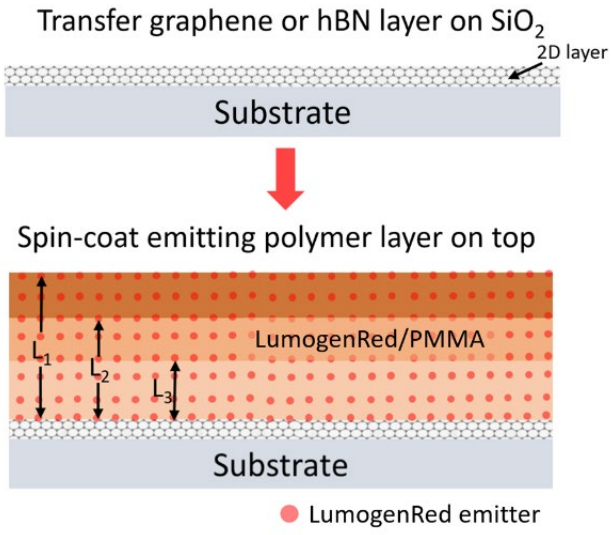

Figure 5.5. a) Schematic of the 2D layer/emitting polymer sample used to extract the fluorescence quenching radius of graphene and h-BN. LumogenRed/PMMA emitting layers with different thicknesses (L) were spin coated onto the 2D layers and the average fluorescence lifetime depends on L and the quenching radius R_0.

After demonstrating that h-BN encapsulation can provide chemical protection, we next had to determine whether it was electronically inert, since the goal was to have an ultrathin coating that did not interact with the organic crystal through energy or charge transfer. One way to assess the presence of such interactions is to look for fluorescence quenching by the 2D layer. Previously, we found that the overall fluorescence decays of single PER crystals were unaffected by the presence of a graphene overlayer.[11] Those measurements probed relatively thick (>100 nm) crystals, however, and could not rule out quenching of a surface layer of up to 20 nm by the graphene. Given the difficulty of growing PER crystals with thicknesses <20 nm[22], where fluorescence quenching would become apparent, we turned to a different strategy to assess how the 2D layers interact with molecular excited states.

Figure 5.5 outlines our experimental approach to measure surface quenching by a 2D layer. Instead of using a molecular crystal, we used a spin-cast polymer film consisting of PMMA doped with the dye molecule Lumogen Red (LR). The thickness of the polymer film can be controlled by the concentration of the precursor solution and the spin coating conditions.[23] The concentration of the dye was kept low enough (< 1 mM[24]) to prevent intermolecular energy migration within the film. Under these conditions, each dopant was quenched individually by the 2D material on the surface without the complicating factor of energy migration that might amplify the quenching effect. The time-dependent excited state population of a molecule at distance R from the quenching layer, $N_{ex}(R,t)$ subject to a distance dependent quenching rate $k_q(R)$, is given by[25]

$$N_{ex}(R,t) = N_0 \exp\left[-k_{fl}t - k_q(R)t\right] \tag{1}$$

k_{fl} is the intrinsic molecular fluorescence decay rate in the absence of quenching, and $k_q(R)$ is assumed to result from Forster electronic energy transfer from a dipole to a 2D surface and is given by the equation[26]

$$k_q(R) = \left(\frac{R_0}{R}\right)^4 \tag{2}$$

To calculate the fluorescence signal S(t) for the dye/polymer film, we sum over all possible distances R from the top quenching layer,

$$S(t) = \sum_{R=0}^{L} N_{ex}(R,t) \tag{3}$$

For this summation, R was stepped in 0.1 nm increments from 0 to the film thickness L. R_0 was a single parameter that was be varied to simulate the S(t) curves for different values of L. In this way we could extract a self-consistent value for the quenching radius R0 from the experimental fluorescence decays.

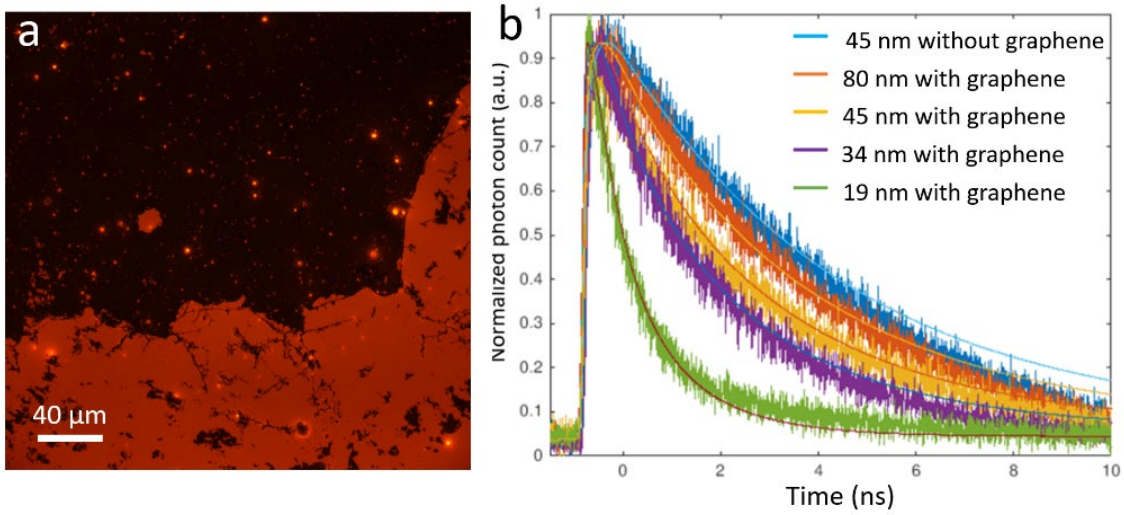

Figure 5.6. a) Fluorescence microscope image of LumogenRed (LR)/PMMA layer (L=30 nm) on top of single layer graphene. The LR/PMMA composite is evenly spin coated onto the substrate, but only the top half contains graphene. The area on top of graphene shows significant fluorescence quenching as compared to bare glass (bright orange). b) Thickness dependence of photoluminescence lifetime of LR/PMMA layer on graphene. The PL decay becomes faster with decreasing emitting layer thickness. Fits using Equation (3) with R_0 = 14.9 nm are overlaid with the data.

Figure 5.6a shows a fluorescence microscope image of an LR/PMMA film spin coated on top of a graphene layer that had been placed on a glass surface using the wet transfer method, i.e. lift-off from an aqueous solution. The regions with no graphene coverage appeared red due to the characteristic LR emission, while the regions with graphene appeared dark, suggesting strong fluorescence quenching. The time-resolved fluorescence decays shown in Figure 5.6b confirm that the graphene layer leads to detectable fluorescence quenching even in 80 nm thick polymer films, consistent with previous work.[27] For a 19 nm thick film, the fluorescence was almost completely absent. Also shown in Figure 5.6b are decay curves calculated using Equations (1)-(3) with R_0 = 14.6±1.0 nm. The calculated curves do a good job of reproducing the experimental trends. The value of the quenching radius R_0 is large relative to typical molecular Forster radii but

in line with values reported for energy donors like quantum dots, where values range from 8-20 nm.[28-30] It is likely that the detailed spectroscopic properties of the energy donor (LR in our case) play a role in determining the overall quenching radius, just as they do in other Forster energy transfer systems, but we did not attempt to model the fluorescence quenching in terms of molecular properties.

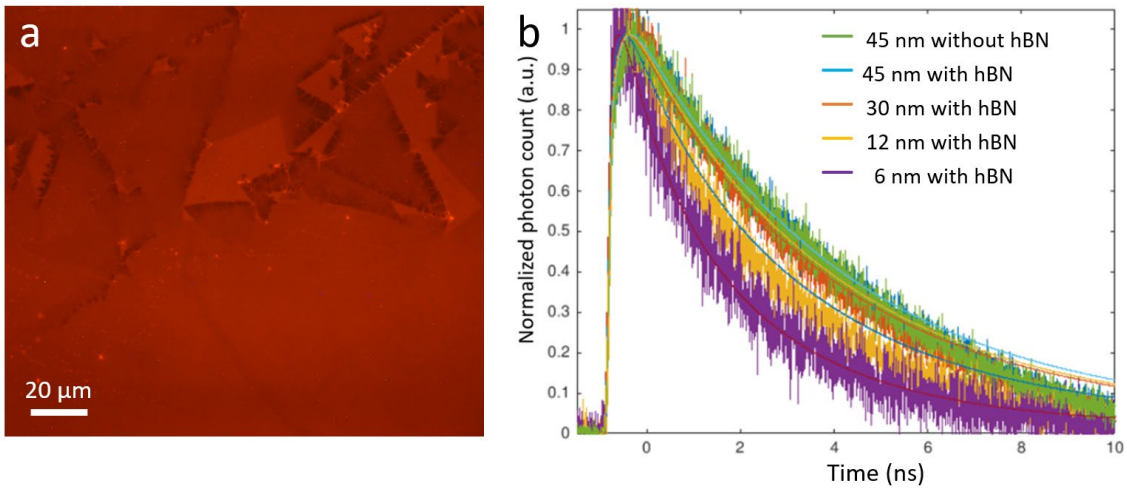

Figure 5.7. a) Fluorescence microscope image of LR/PMMA layer (L=15 nm) on top of an MBE h-BN layer. The area covered with h-BN (visible as triangular outlines) shows slight fluorescence quenching; b) Thickness dependence of photoluminescence lifetime of LR/PMMA layer on MBE-grown h-BN using the wet transfer method. The PL decay becomes faster with decreasing emitting layer thickness. Fits using Equation (3) with R_0 = 2.9 nm are overlaid with the data.

The fact that the polymer-dye method gave reasonable values for graphene was encouraging. We then spin-coated an LR/PMMA film on top of an MBE-grown h-BN layer that had been placed on a glass surface using the wet transfer method. In Figure 5.7a, a fluorescence microscope image of the LR/PMMA film shows that the presence of the h-BN diminished but did not extinguish the red fluorescence. Time-resolved measurements confirmed that the effect of the h-BN on the LR/PMMA fluorescence lifetime was much

less pronounced than with graphene. Figure 5.7b shows the fluorescence decays of various thickness LR/PMMA films with the MBE-grown h-BN on top. As with graphene, there was a systematic decrease in lifetime as the polymer thickness decreased and more LR molecules found themselves close to the surface. Also shown are the decay curves calculated for R_0 = 2.9 nm, which do a good job of reproducing the observed trend with thickness.

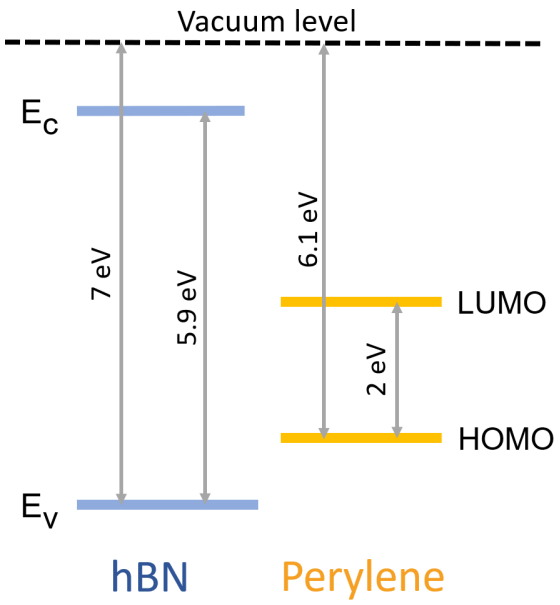

Figure 5.8. Band diagram of h-BN and perylene[31-33].

The R_0 for these h-BN layers was about 5× Smaller than that of graphene, but it was surprising to see any quenching at all. H-BN's large bandgap of 5.9 eV should prevent direct energy transfer. Its low-lying valence band and high conduction band should likewise preclude electron transfer to or from the excited LR molecule (Figure 5.8).[31, 34] Furthermore, any fluorescence quenching based on electron transfer would be expected to be very short-range, typically < 1nm. The relatively large distances observed here are consistent with through-space energy transfer as assumed in our model. For graphene, this

is expected since it is a semimetal that has a high density of states that can accept energy from a wide variety of luminescent donors. For pristine h-BN, however, there should be no acceptor states in the 2.0 eV energy range.

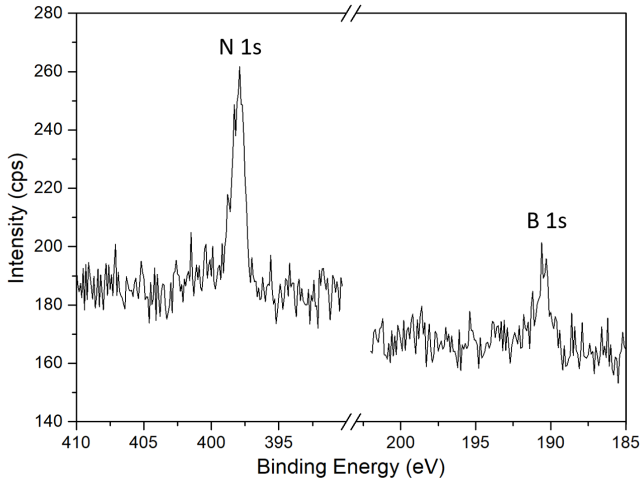

Figure 5.9. XPS analysis of B 1s and N 1s of wet-transferred MBE h-BN.

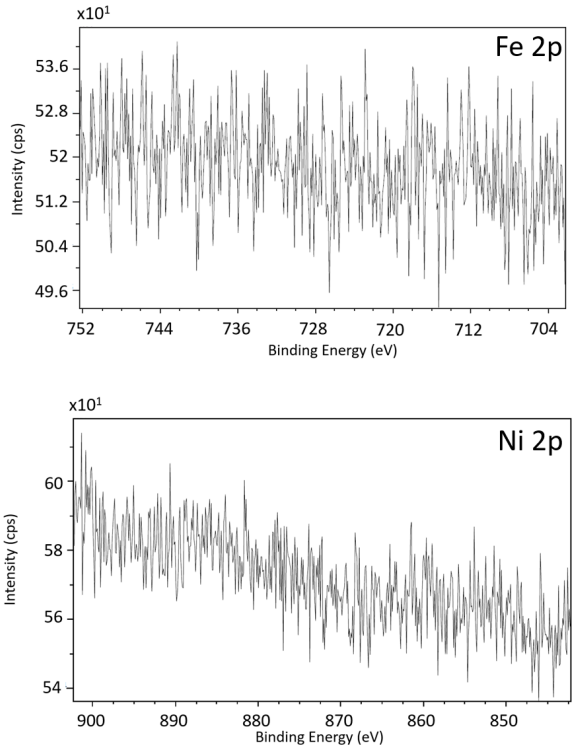

Figure 5.10. XPS analysis of Fe 2p and Ni 2p in the wet-transferred MBE-grown h-BN. No feature from Fe or Ni is detected.

Here we consider two possible origins of the energy accepting states that quench the LR fluorescence. The first possibility is that chemical impurities left over from the transfer process act as energy acceptors. The wet transfer method used here has the advantage of being able to transfer large areas of 2D materials quickly and reproducibly.[35] But the solvent and ions may become trapped between the 2D layer and the crystal. However, we could not find any evidence that extrinsic chemical species, for example Ni ions, were responsible for the fluorescence quenching. X-ray photoelectron spectroscopy measurements on coated substrates failed to reveal any detectable signature of Ni or any other elements besides B and N (Figures 5.9 and 5.10). After dissolution of the Ni substrate, the h-BN was subjected to repeated solvent replacements to remove any residual species left over from the etching process, but the amount of fluorescence quenching was insensitive to the number of times the transfer solvent was exchanged in the h-BN rinsing step.

A second possibility is that defects in the h-BN itself are responsible for the quenching. Recent studies have shown that most h-BN samples contain defects that luminesce in this energy range with nanosecond lifetimes and high quantum yields.[36-38] It is not unreasonable to expect that the strong radiative rate of the defect is accompanied by a strong absorption as well. These defects, whose exact structure is a topic of active investigation, could also act as energy acceptors for the excited LR molecules. Note that all that is required is a concentration of absorbing defect states – they do not have to be emissive and in fact may be completely different from the luminescent defects that are more commonly studied. These defects may be present when the h-BN is grown, or they may be introduced during

the sample processing. For example, the floating, lift-off, and subsequent solvent dissolution of the polymer layer can all induce transient stress in the 2D layer and create defects along the way.

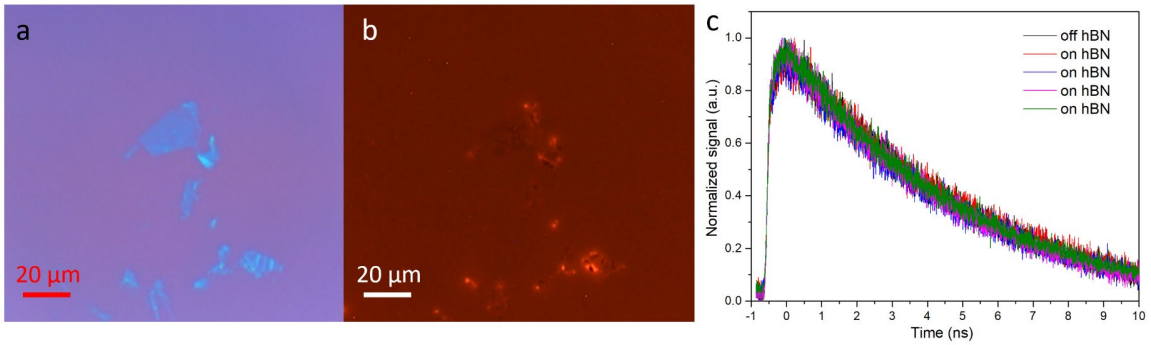

Figure 5.11. a, b) Reflectance and fluorescence microscopy images of an LR/PMMA layer (L=10 nm) on exfoliated MBE-grown h-BN placed on glass using the dry-transfer method. c) Photoluminescent decays of LR/PMMA layer both on and off the h-BN. The bright spots are from the aggregation of polymer on the edge and wrinkles of the h-BN flakes. They are avoided during the fluorescence measurement.

If the LR fluorescence is being quenched by defect states in the h-BN, then changing the method of preparation to reduce defect density should reduce the fluorescence quenching as well. Dry transfer methods provide the gentlest way to transfer 2D materials [39-40], but they are more labor intensive, producing Smaller flakes that must be individually positioned and deposited. The h-BN flakes produced in this way are usually too Small for complete crystal encapsulation, but it was possible to examine whether they quenched the fluorescence. The fluorescence lifetime was measured at various locations in LR/PMMA films that had been spin-coated on top of several h-BN flakes. None of the decays in Figure 5.11 show measurable quenching of the LR fluorescence, whether on top of the h-BN or not. This result suggests that the defects that lead to fluorescence quenching are indeed introduced via the wet transfer method and can be avoided by using dry transfer. Recently

developed methods for the growth and transfer of large h-BN flakes with diameters on the order of 100 microns[41-42] may make it possible to completely cover a single crystal and seal to the surrounding substrate, so that full encapsulation under inert h-BN can be achieved.

Conclusion

The results reported here show that, like graphene, ultrathin layers of h-BN can be used to fully encapsulate single organic crystals. Successful encapsulation depends on the quality of the h-BN and we found that only multi-layer MBE-grown h-BN could fully protect the crystals from dissolution and sublimation. Investigation of the effects of these 2D coatings on the fluorescence signal of thin dye/polymer films revealed that the wet transfer method likely produces structural defects in the h-BN that act as fluorescence quenching sites. This quenching could be avoided by the use of a dry transfer method, which we hope will enable the encapsulation of single crystals under a truly inert, transparent coating. The results of this work represent a step forward in our efforts to integrate 2D materials with molecular crystals in order to create new platforms for the measurement of their electronic properties.

References

1. Butler, S. Z.; Hollen, S. M.; Cao, L.; Cui, Y.; Gupta, J. A.; Gutierrez, H. R.; Heinz, T. F.; Hong, S. S.; Huang, J.; Ismach, A. F.; Johnston-Halperin, E.; Kuno, M.; Plashnitsa, V. V.; Robinson, R. D.; Ruoff, R. S.; Salahuddin, S.; Shan, J.; Shi, L.; Spencer, M. G.; Terrones, M.; Windl, W.; Goldberger, J. E., Progress, Challenges, and Opportunities in Two-Dimensional Materials Beyond Graphene. *ACS Nano* **2013,** *7*, 2898–2926.

2. Zhuang, X.; Mai, Y.; Wu, D.; Zhang, F.; Feng, X., Two-Dimensional Soft Nanomaterials: A Fascinating World of Materials. *Advanced Materials* **2015,** *27*, 403–427.

3. Berry, V., Impermeability of Graphene and its Applications. *Carbon* **2013,** *62*, 1-10.

4. Bunch, J. S.; Verbridge, S. S.; Alden, J. S.; Zande, A. M. v. d.; Parpia, J. M.; Craighead, H. G.; McEuen, P. L., Impermeable Atomic Membranes from Graphene Sheets. *Nano Letters* **2008,** *8*, 2458-2462.

5. Dervin, S.; Dionysiou, D. D.; Pillai, S. C., 2D Nanostructures for Water Purification: Graphene and Beyond. *Nanoscale* **2016,** *8*, 15115–15131.

6. Prozorovska, L.; Kidambi, P. R., State-of-the-Art and Future Prospects for Atomically Thin Membranes from 2D Materials. *Advanced Materials* **2018,** *30*, 1801179/1-24.

7. Wang, S.; Yang, L.; He, G.; Shi, B.; Li, Y.; Wu, H.; Zhang, R.; Nunes, S.; Jiang, Z., Two-Dimensional Nanochannel Membranes for Molecular and Ionic Separations. *Chemical Society Reviews* **2020,** *49*, 1071--1089.

8. Deng, B.; Hsu, P.-C.; Chen, G.; Chandrashekar, B. N.; Liao, L.; Ayitimuda, Z.; Wu, J.; Guo, Y.; Lin, L.; Zhou, Y.; Aisijiang, M.; Xie, Q.; Cui, Y.; Liu, Z.; Peng, H., Roll-to-Roll Encapsulation of Metal Nanowires between Graphene and Plastic Substrate for High-Performance Flexible Transparent Electrodes. *Nano Letters* **2015,** *15*, 4206-4213.

9. Shen, X.; Wang, M.; Zhou, F.; Qiu, B.; Cai, L.; Liu, Y.; Zhen, Z.; Chai, Y., Improved Air-Stability of an Organic–Inorganic Perovskite with Anhydrously Transferred Graphene. *Journal of Materials Chemistry C* **2018,** *6*, 8663--8669.

10. Xia, K.; Jian, M.; Wang, C.; Yin, Z.; Zhang, M.; Wang, H.; Yang Wu; Zhang, Y., Seamless Graphene-Seal-Wrap as a Removable Protective Cover for Two-Dimensional Materials. *ACS Materials Lett.* **2020,** *2*, 215−219.

11. Li, W.; Tierce, N. T.; Bekyarova, E.; Bardeen, C. J., Protection of Molecular Microcrystals by Encapsulation under Single-Layer Graphene. *ACS Omega* **2018,** *3*, 8129−8134.

12. Cassabois, G.; Valvin, P.; Gil, B., Hexagonal Boron Nitride is an Indirect Bandgap Semiconductor. *Nat. Photonics* **2016,** *10*, 262-266.

13. Petrone, N.; Chari, T.; Meric, I.; Wang, L.; Shepard, K. L.; Hone, J., Flexible Graphene Field-Effect Transistors Encapsulated in Hexagonal Boron Nitride. *ACS Nano* **2015,** *9*, 8953–8959.

14. Gwan-Hyoung Lee; Cui, X.; Kim, Y. D.; Arefe, G.; Zhang, X.; Lee, C.-H.; Ye, F.; Watanabe, K.; Taniguchi, T.; Kim, P.; Hone, J., Highly Stable, Dual-Gated MoS_2 Transistors Encapsulated by Hexagonal Boron Nitride with Gate-Controllable Contact, Resistance, and Threshold Voltage. *ACS Nano* **2015,** *9*, 7019–7026.

15. Chen, X.; Wu, Y.; Wu, Z.; Han, Y.; Xu, S.; Wang, L.; Ye, W.; Han, T.; He, Y.; Cai, Y.; Wang, N., High-Quality Sandwiched Black Phosphorus Heterostructure and its Quantum Oscillations. *Nature Communications* **2015,** *6*, 7315/1-6.

16. Liu, Z.; Gong, Y.; Zhou, W.; Ma, L.; Yu, J.; Idrobo, J. C.; Jung, J.; MacDonald, A. H.; Vajtai, R.; Lou, J.; Ajayan, P. M., Ultrathin High-Temperature Oxidation-Resistant Coatings of Hexagonal Boron Nitride. *Nature Communications* **2013,** *4*, 2541/1-8.

17. Fang, H.-H.; Yang, J.; Tao, S.; Adjokatse, S.; Machteld E. Kamminga; Ye, J.; Blake, G. R.; Even, J.; Loi, M. A., Unravelling Light-Induced Degradation of Layered Perovskite Crystals and Design of Efficient Encapsulation for Improved Photostability. *Advanced Functional Materials* **2018,** *28*, 1800305/1-11.

18. Falin, A.; Cai, Q.; Santos, E. J. G.; Scullion, D.; Qian, D.; Zhang, R.; Yang, Z.; Huang, S.; Watanabe, K.; Taniguchi, T.; Barnett, M. R.; Chen, Y.; Ruoff, R. S.; Li, L. H., Mechanical Properties of Atomically Thin Boron Nitride and the Role of Interlayer Interactions. *Nature Communications* **2017,** *8*, 15815/1-9.

19. Mallick, G.; Elder, R. M., Graphene/Hexagonal Boron Nitride Heterostructures: Mechanical Properties and Fracture Behavior from Nanoindentation Simulations. *Applied Physics Letters* **2018,** *113*, 121902/1-5.

20. Pick, A.; Klues, M.; Rinn, A.; Harms, K.; Chatterjee, S.; Witte, G., Polymorph-Selective Preparation and Structural Characterization of Perylene Single Crystals. *Crystal Growth & Design* **2015,** *15*, 5495-5504.

21. Xu, Z.; Tian, H.; Khanaki, A.; Zheng, R.; Suja, M.; Liu, J., Large-Area Growth of Multilayer Hexagonal Boron Nitride on Polished Cobalt Foils by Plasma Assisted Molecular Beam Epitaxy. *Scientific Reports* **2017,** *7*, 43100/1-7.

22. Lei, Y.; Liao, Q.; Fu, H.; Yao, J., Phase- and Shape-Controlled Synthesis of Single Crystalline Perylene Nanosheets and Its Optical Properties. *Journal of Physical Chemistry C* **2009,** *113*, 10038–10043.

23. Walsh, C. B.; Franses, E. I., Ultrathin PMMA Films Spin-Coated from Toluene Solutions. *Thin Solid Films* **2003,** *429*, 71-76.

24. Colby, K. A.; Burdett, J. J.; Frisbee, R. F.; Zhu, L.; Dillon, R. J.; Bardeen, C. J., Electronic Energy Migration on Different Time Scales: Concentration Dependence of the Time-Resolved Anisotropy and Fluorescence Quenching of Lumogen Red in Poly(methyl methacrylate). *Journal of Physical Chemistry A* **2010,** *114*, 3471–3482.

25. Piland, G. B.; Burdett, J. J.; Hung, T.-Y.; Chen, P.-H.; Lin, C.-F.; Chiu, T.-L.; Lee, J.-H.; Bardeen, C. J., Dynamics of Molecular Excitons Near a Semiconductor Surface Studied by Fluorescence Quenching of Polycrystalline Tetracene on Silicon. *Chemical Physics Letters* **2014,** *601*, 33–38.

26. Swathi, R. S.; Sebastian, K. L., Long Range Resonance Energy Transfer from a Dye Molecule to Graphene has (Distance)$^{-4}$ Dependence. *Journal of Chemical Physics* **2009,** *130*, 086101/1-3.

27. Goncalves, H.; Bernardo, C.; Moura, C.; Ferreira, R. A. S.; Andre, P. S.; Stauber, T.; Belsley, M.; Schellenberg, P., Long Range Energy Transfer in Graphene Hybrid Structures. *Journal of Physics D* **2016,** *49*, 315102/1-6.

28. Kasry, A.; Ardakani, A. A.; Tulevski, G. S.; Menges, B.; Copel, M.; Vyklicky, L., Highly Efficient Fluorescence Quenching with Graphene. *Journal of Physical Chemistry C* **2012,** *116*, 2858−2862.

29. Liu, Y.; Liu, C. Y.; Liu, Y., Investigation on Fluorescence Quenching of Dyes by Graphite Oxide and Graphene. *Applied Surface Science* **2011,** *257*, 5513–5518.

30. Raja, A.; Montoya-Castillo, A.; Zultak, J.; Zhang, X.-X.; Ye, Z.; Roquelet, C.; Chenet, D. A.; Zande, A. M. v. d.; Huang, P.; Jockusch, S.; Hone, J.; Reichman, D. R.; Brus, L. E.; Heinz, T. F., Energy Transfer from Quantum Dots to Graphene and MoS_2: The Role of Absorption and Screening in Two-Dimensional Materials. *Nano Letters* **2016,** *16*, 2328-2333.

31. Pookpanratana, S. J.; Goetz, K. P.; Bittle, E. G.; Haneef, H.; Youa, L.; Hackera, C. A.; Robeye, S. W.; Jurchescu, O. D.; Ovsyannikov, R.; Giangrisostomi, E., Electronic Properties and Structure of Single Crystal Perylene. *Organic Electronics* **2018,** *61*, 157-163.

32. Shi, Y.; Hamsen, C.; Jia, X.; Kim, K. K.; Reina, A.; Hofmann, M.; Hsu, A. L.; Zhang, K.; Li, H.; Juang, Z.-Y., Synthesis of few-layer hexagonal boron nitride thin film by chemical vapor deposition. *Nano Letters* **2010,** *10* (10), 4134-4139.

33. Mahvash, F.; Paradis, E.; Drouin, D.; Szkopek, T.; Siaj, M., Space-charge limited transport in large-area monolayer hexagonal boron nitride. *Nano Letters* **2015,** *15* (4), 2263-2268.

34. Mahvash, F.; Paradis, E.; Drouin, D.; Szkopek, T.; Siaj, M., Space-Charge Limited Transport in Large-Area Monolayer Hexagonal Boron Nitride. *Nano Letters* **2015,** *15*, 2263−2268.

35. Chen, M.; Li, G.; Li, W.; Stekovic, D.; Arkook, B.; Itkis, M. E.; Pekker, A.; Bekyarova, E.; Haddon, R. C., Large-Scale Cellulose-Assisted Transfer of Graphene Toward Industrial Applications. *Carbon* **2016,** *110*, 286-291.

36. Jungwirth, N. R.; Fuchs, G. D., Optical Absorption and Emission Mechanisms of Single Defects in Hexagonal Boron Nitride. *Physical Review Letters* **2017,** *119*, 057401/1-6.

37. Grosso, G.; Moon, H.; Lienhard, B.; Ali, S.; Efetov, D. K.; Furchi, M. M.; Jarillo-Herrero, P.; Ford, M. J.; Aharonovich, I.; Englund, D., Tunable and High-Purity Room Temperature Single-Photon Emission from Atomic Defects in Hexagonal Boron Nitride. *Nature Communications* **2017,** *8*, 705/1-8.

38. Exarhos, A. L.; Hopper, D. A.; Grote, R. R.; Alkauskas, A.; Bassett, L. C., Optical Signatures of Quantum Emitters in Suspended Hexagonal Boron Nitride. *ACS Nano* **2017,** *11*, 3328−3336.

39. Castellanos-Gomez, A.; Buscema, M.; Molenaar, R.; Singh, V.; Janssen, L.; Zant, H. S. J. v. d.; Steele, G. A., Deterministic Transfer of Two-Dimensional Materials by All-Dry Viscoelastic Stamping. *2D Materials* **2014,** *1*, 011002/1-9.

40. Kinoshita, K.; Moriya, R.; Onodera, M.; Wakafuji, Y.; Masubuchi, S.; Watanabe, K.; Taniguchi, T.; Machida, T., Dry release Transfer of Graphene and Few-Layer h-BN by Utilizing thermoplasticity of Polypropylene Carbonate. *npj 2D Materials and Applications* **2019**, 22/1-8.

41. Chen, T.-A.; Chuu, C.-P.; Tseng, C.-C.; Wen, C.-K.; Wong, H.-S. P.; Pan, S.; Li, R.; Chao, T.-A.; Chueh, W.-C.; Zhang, Y.; Fu, Q.; Yakobson, B. I.; Chang, W.-H.; Li, L.-J., Wafer-Scale Single-Crystal Hexagonal Boron Nitride Monolayers on Cu (111). *Nature* **2020,** *579*, 219-223.

42. Liu, F.; Wu, W.; Bai, Y.; Chae, S. H.; Li, Q.; Wang, J.; Hone, J.; Zhu, X.-Y., Disassembling 2D Van der Waals Crystals into Macroscopic Monolayers and Reassembling into Artificial Lattices. *Science* **2020,** *367*, 903–906.

Chapter 6. Effect of Constructive Rehybridization on Transverse Conductivity of Aligned Single-Walled Carbon Nanotube Films

After polyaromatic molecules and graphene, we turn our attention to another low dimensional carbon materials in this chapter. During this project, we study and further engineer the morphology of single-walled carbon nanotube (SWNT) thin films. By controlling the filtration speed to filter out the SWNT from suspension, SWNTs can deposition on the polymer filter with different film topologies. Fast filtration produced random SWNT film while slow filtration achieved well-aligned SWNT arrays depositing on polymer film. Organometallic functionalization is then carried out on aligned SWNT films, and we observe spatially anisotropic conductivity changes, which is very different from the result on random SWNT film. The aligning of SWNTs bring the properties of the macroscopic film closer to the individual carbon nanotube.

Introduction

Single-walled carbon nanotubes (SWNTs) have excellent electronic properties, which make them attractive candidates for next-generation electronics and optoelectronics [1-4]. Whereas individual SWNT devices have been demonstrated, their practical utilization in electronic circuits remains a challenge. High quality, thin films of random SWNTs have been considered as an alternative solution, however the outstanding SWNT properties are largely diminished in macroscopically assembled thin films due to the intertube junction resistance, which significantly exceeds that of individual SWNTs [5-8]. Recent advances in the alignment of SWNTs made possible the preparation of films of densely packed parallel

SWNTs [9-15] and this stimulated a growing interest in their electronic properties and utilization in electronic devices [16-20]. In fact, the anisotropic electrical and thermal properties of aligned SWNTs have long been a topic of interest [21-23]. In such films the conductivity along the alignment direction (parallel conductivity) is much higher as compared with the direction perpendicular to the SWNT axis (transverse conductivity). The large anisotropy can be explained with a simple model assuming that the film resistance is dominated by the intertube junctions: for a given SWNT film length there are dramatically less tube-tube contacts in parallel versus perpendicular direction due to the very large aspect ratio of the SWNTs (~10^3). Thus, seamlessly interconnecting the SWNTs post-alignment would have a dramatic effect on the degree of electrical anisotropy. Bridging graphene surfaces, and in particular carbon nanotubes, has been successfully accomplished using covalent chemistry. Although this chemistry has proven to be useful for development of advanced electronic applications, including molecular switches [24-25], the covalent bond formation to the carbon atoms of the graphene lattice results in a change of the hybridization from sp^2 to sp^3 [26-30] and therefore it causes a decrease of the conductivity. The ability to form a bond to the sidewalls of carbon nanotubes without significant rehybridization is critical for the electronic and optoelectronic applications of these materials. Very few chemistries offer preserved hybridization, examples include cycloaddition [31-33] and organometallic reactions [34-35]. The ability of the organometallic bond to form without significant rehybridization is the key to the usefulness of this new mode of bonding in electrically connecting carbon materials based on the benzenoid ring system. We have classified this type of bonding as constructive rehybridization, in which

the extended π-electronic structure of graphene is complexed with a transition metal and the degree of rehybridization at the site of complexation is insufficient to saturate the conjugated electronic band structure [36-37].

Here we utilize aligned SWNT thin films that consist of a statistical mixture of semiconducting and metallic (2:1) SWNTs to insert chromium atoms between a pair of parallel SWNTs and interconnect them. This mode of bonding dramatically reduces the electrical resistance of the films in direction perpendicular to the SWNT axis, while it has negligible effect on the conductivity parallel to the SWNT alignment. We suggest that the chromium atoms coordinate to the benzenoid rings of adjacent SWNTs to covalently link them via hexahapto bond. The study demonstrates that this type of bonding is feasible in homogeneous dense aligned SWNT films. The hexahapto bond preserves the geometric and electronic structure of individual SWNTs [35] while extending the dimensionality from 1D to quasi 2D.

Films of aligned semiconducting SWNTs with improved intertube junctions have potential applications as the active constituents in high performance electronics and advanced optoelectronics. Other areas of interests are quantum computing and magnetic nanodevices as some of these graphene-transition metal compounds are magnetic [38] and the aligned SWNTs offer a platform for the assembly of ordered magnetic systems. The hexahapto bonding of atomic chromium [Cr(0)] to graphene surfaces may complement existing technologies that employ ion-selective sensors for environmental monitoring [39-43].

The reversible nature of the graphene–hexahapto complexation [44] is further explored for the reversible chemical engineering of the transport properties of aligned SWNTs and preparation of atomic switches. This was accomplished by turning on an SWNT array by a photochemical complexation with transition metals and turning it off by electric field.

Results and Discussion

Aligned SWNT thin films provide an ideal platform to study the nature of the interaction between transition metal atoms and graphitic surfaces, due to the densely packed individual SWNTs and the giant anisotropy of electrical resistance in directions parallel and perpendicular to the nanotube alignment. In this work, we prepared aligned SWNT thin films and explored the effect of bridging the adjacent carbon nanotubes with Cr atoms on the film conductivity in transverse and parallel directions.

We have pursued the organometallic chemistry of carbon nanotubes in solution phase [34, 45-46] and in solid state [36, 47-48] reactions and have shown that this leads to the formation of covalent bis(η^{6}-SWNT)M bonds (M = Cr, Mo, W, V, Mn). Previous studies utilize random networks of SWNT thin films, in which the transport properties are dominated by the carbon nanotube junctions and our experiments showed that the covalent hexahapto-bonds formed by chromium to the sidewalls of the SWNTs are very effective in reducing the nanotube junction resistance and increasing the film conductivity [36, 48]. If achieved in aligned SWNT films this mode of bonding would have a profound effect on the degree of electrical anisotropy and we anticipated that hexahapto bond formation is feasible in homogeneous and sufficiently dense films of aligned SWNTs in which the distance between adjacent SWNTs approaches the van der Walls distance of 3.15 Å [49]; a stable

molecular structure in the bis(benzene) chromium complex is associated with a distance of 3.226 Å between two benzene rings [50].

Homogeneous, dense, preferentially aligned SWNT thin films were prepared by slow filtration [15] as shown in Figure 6.1a-c. The SWNT dispersions, used for the film preparation, contained individual SWNTs as evidenced by the absorption spectrum which exhibits sharp and well resolved electronic absorption bands and the AFM imaging (Figure 6.1 d-f).

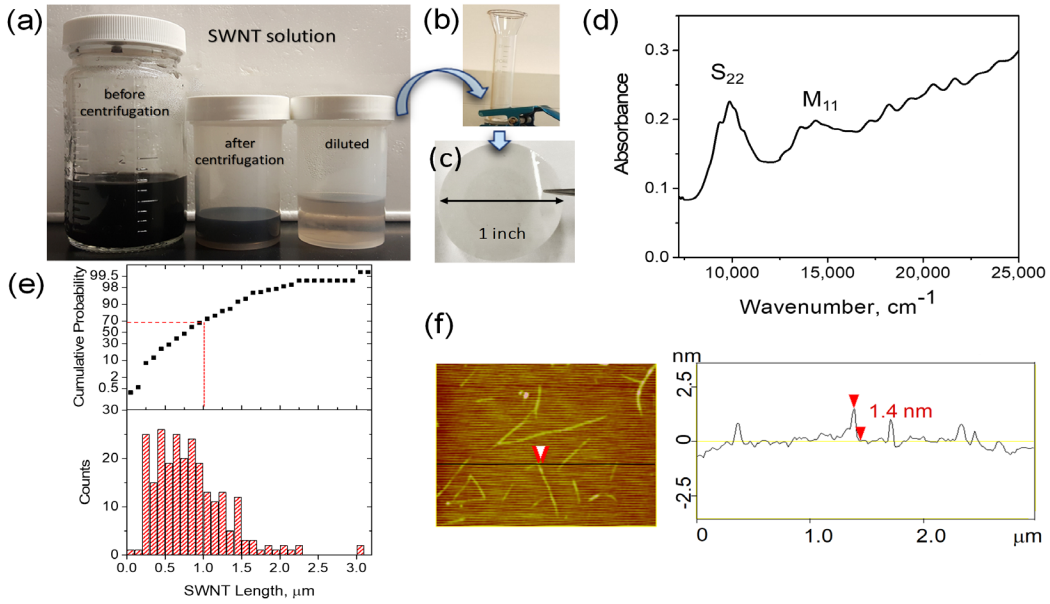

Figure 6.1. Aligned SWNT film preparation: a) Aqueous dispersions of electric arc-discharge SWNTs used for preparation of aligned SWNT films. b) Filtration apparatus for film preparation c) a photograph of aligned SWNT thin film on filtration membrane. d) Absorption spectrum of SWNT dispersion e) Distribution of SWNT length estimated from AFM images. f) AFM image and height profile of SWNTs present in the dispersions used for film preparation.

The length of the SWNTs varies in the range of 0.5 to 4 µm (Figure 6.1e) and the average diameter is ~1.4 nm (Figure 6.1f), in good agreement with the average diameter of arc-produced SWNTs [51-52].

The alignment of the SWNT thin films was assessed with AFM and SEM; typical images shown in Figure 6.2a,b illustrate that the SWNTs are relatively well aligned and exist in Small bundles (average bundle size 5-7 nm). Further spectroscopic characterization confirmed the SWNT alignment, which resulted in polarization dependent absorption and Raman spectra as illustrated in Figure 6.2c, d. For these measurements the SWNT films were rotated to align the electric field of the incident light parallel and perpendicular to the nanotube alignment direction.

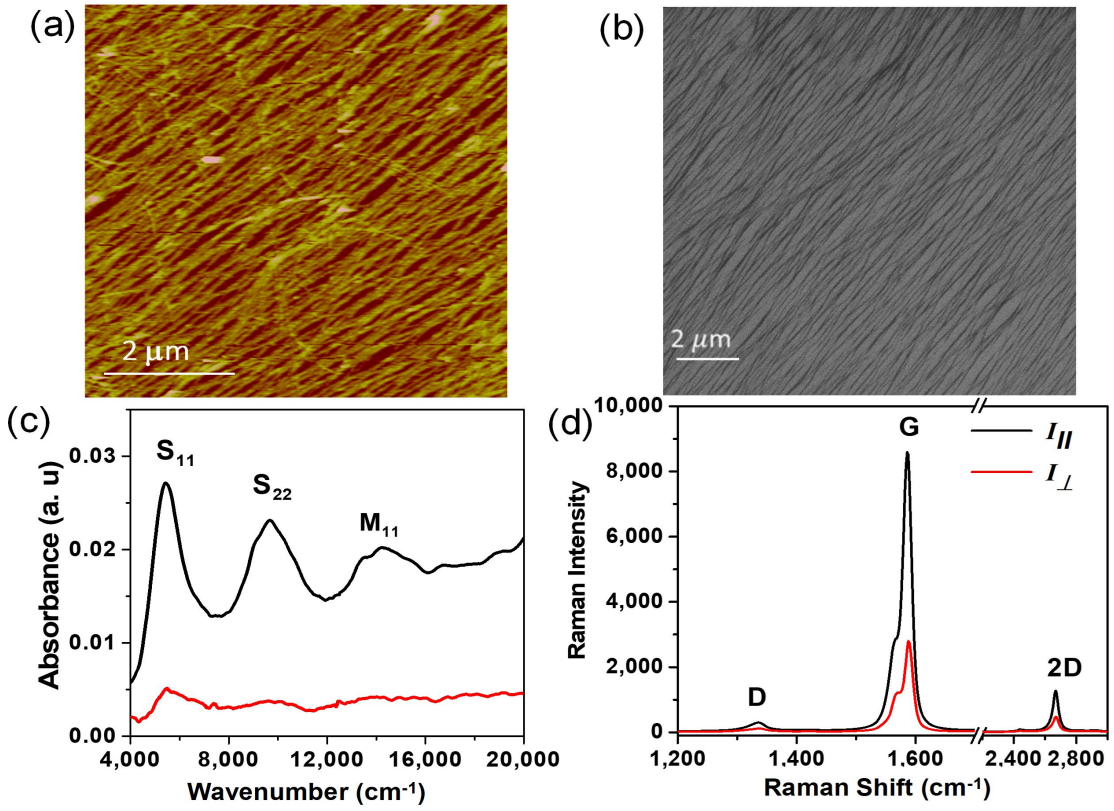

Figure 6.2. Characterization of aligned SWNT films: a) AFM and b) SEM images of densely packed aligned SWNTs. c) Absorption spectra of aligned SWNTs recorded with the incident light beam parallel (black) and perpendicular (red) to the SWNT alignment direction (d) Raman spectra of aligned SWNTs collected with the polarization direction of the incident laser beam parallel (black) and perpendicular (red) to the nanotube alignment direction.

For the absorption measurements baseline corrections for the bare glass substrate were performed in both directions. The first two interband transitions of semiconducting nanotubes (S_{11} and S_{22}) and the first interband transition of metallic nanotubes (M_{11}) are strongly suppressed in the perpendicular direction as compared to the parallel polarization (Figure 6.2c). The largest Raman intensity in the spectra of aligned SWNT films is observed when the polarization of the laser beam was along the SWNT axes and the absorption/emission of light is highly suppressed for light polarized perpendicular to the nanotube axis, producing a very weak signal [53-55]. The intensity of the G-peak in the parallel direction ($I_{//}$) is 3 times larger than that obtained in perpendicular direction ($I_{\perp}$), confirming the high degree of alignment of the SWNTs [15].

We prepared two sets of devices (Figure 6.3a) in which the SWNT films were placed in two distinct orientations: (i) parallel aligned SWNT films, in which the SWNTs span the channel length for measurement of the parallel conductivity (current flows along the SWNT axis) and (ii) transverse aligned SWNT films, in which the tubes are aligned along the width of the electrodes for the transverse conductivity measurement (current flows across the individual nanotubes).

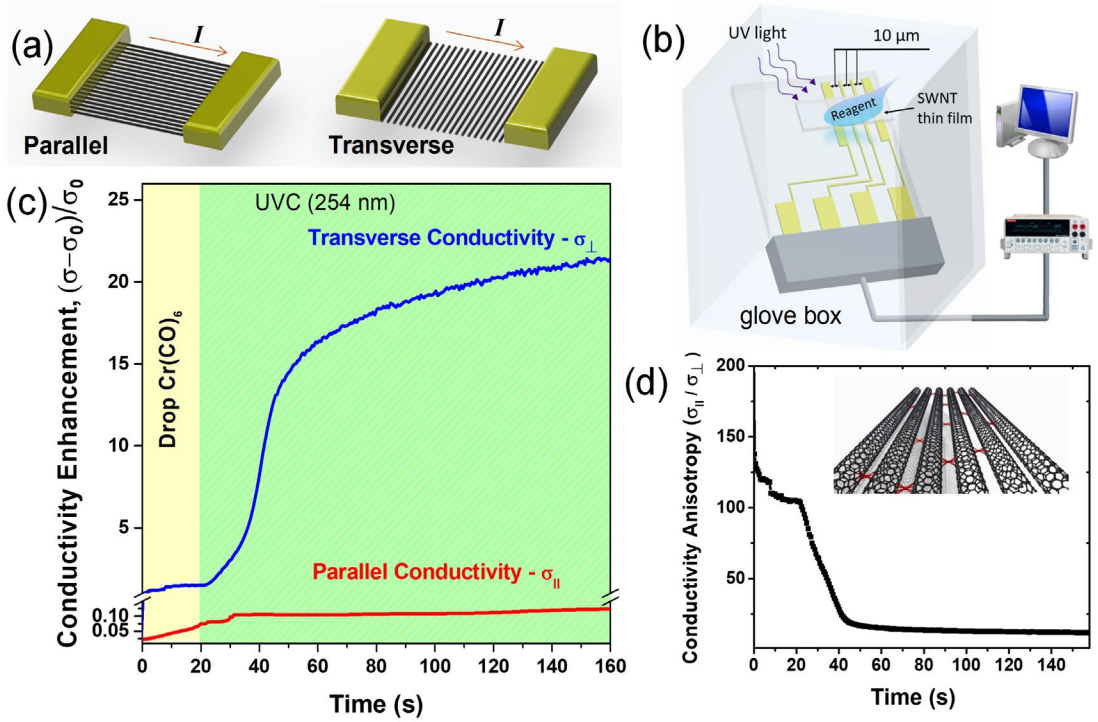

Figure 6.3. Effect of hexahapto bonds of chromium on the conductivity of aligned SWNTs. a) Schematics of the device configurations used for measurement of transverse and parallel conductivities; the dimensions are not to scale. b) Experimental set-up for the photochemical reaction between aligned SWNT films and $Cr(CO)_6$. c) Enhancement of aligned SWNT thin film conductivities (transverse and parallel) on photochemical reaction with $Cr(CO)_6$. d) Electrical anisotropy as a function of reaction time. The inset shows a schematic of the formation of atomic interconnects (red) between pairs of aligned SWNTs, (η^6-SWNT)Cr(η^6-SWNT).

The measured transverse conductivity of aligned pristine SWNT films (thicknesses τ in the range of 0.5 nm to 1 nm) after thermal annealing varied between 1 and 30 S/cm. In the parallel direction the aligned SWNT films exhibited conductivity of ~270 to 1500 S/cm. Thus, the electrical anisotropy of the aligned SWNTs in our experiments varied in the range of 50 to about 270, depending on the degree of alignment. To interconnect the aligned SWNTs we used a photochemical route that is known to generate bishexahapto bonds between the Cr atoms and the graphitic surfaces of SWNTs [46]. A drop of $Cr(CO)_6$ solution

in acetonitrile was placed on the surface of the film, which was then exposed to short-wavelength light, UVC of 254 nm. The change of the film resistance was followed by *in-situ* measurement with the experimental setup shown schematically in Figure 6.3b.

Upon irradiation of the films with UVC light of 254 nm, the resistance of the films decreased and the trend of conductivity enhancement of the aligned SWNT films in the two alignment directions is shown in Figure 6.3c. The transverse conductivity, $\sigma_{\perp}$, of one film increased dramatically from 1 S/cm to 22 S/cm, producing a conductivity enhancement of more than more 20 times (2100%), whereas nearly no enhancement was recorded for the aligned SWNT film with parallel device configuration (conductivity increase of ~10%). The dramatic increase of the transverse conductivity combined with the moderate increase of parallel conductivity leads to a reduced electrical anisotropy of the aligned SWNT thin films, which decreases from >100, in pristine films, to less than 10 after interconnecting the SWNTs with Cr atoms (Fig. 5.3d). The effect of interconnecting aligned SWNTs on the electrical anisotropy of the films can be further enhanced by optimization of the alignment homogeneity, tube density and channel length.

The increase of SWNT film conductivity can be explained by the formation of covalent bishexahapto bonds between the Cr atoms and the graphitic surfaces of the nanotubes (η^6-SWNT)Cr(η^6-SWNT) as shown in Figure 6.3d (inset). Because this mode of bonding preserves the electronic structure of SWNTs (constructive rehybridization), it bridges the individual SWNTs at the atomic scale leading to improved inter-tube junction resistance and it has been shown to effectively operate in random networks of SWNTs [46, 48, 56-59]. As

discussed in our previous work [46, 48, 56-59] the formation of the hexahapto constructive covalent bonds between the sidewalls of a pair of individual SWNTs is both kinetically and thermodynamically favorable due to the fact that the van der Waals distance (3.15 Å) between adjacent SWNTs is close to the length of the hexahapto bond formed between Cr and the benzene ligands in bisbenzene chromium (3.226 Å). Furthermore, the formation of bishexahapto coordination will lower the energy of the system and satisfy the 18-electron rule required for a stable complex [36, 46, 60].

We next discuss the effect of the improved intertube junctions on the conductivity of aligned SWNT thin films in parallel and transverse directions. We first consider the transport mechanism in direction parallel to the SWNT axis. From the AFM measurements (Figure 6.1e) we estimate that more than 30% of the SWNTs have a length of >1 μm and about 10% of the tubes have length between 1.5 and 3 μm. In these experiments the channel length is 10 μm and assuming SWNT length of 2 μm we estimate that the formation of a conducting path between the electrodes requires about 5 nanotubes, i.e. 4 junctions. Further, our experiments involve SWNT thin films with a density of 300 tubes/μm or higher, which is far beyond the critical density needed for percolation transport [17]. Thus, because the films are comprised of a statistical mixture of metallic and semiconducting SWNTs, there is a reasonably high probability of all-metallic SWNT conducting paths in our devices. The contact resistance between metallic SWNTs is known to be Small [7, 61] and interconnecting random networks of metallic SWNTs with Cr atoms leads to a moderate conductivity increase (<<1) [48]. It is also important to note that the aligned SWNTs contain Small bundles (5-7 nm diameter) and these bundles are long enough to span the 10

μm long channel of our devices, i.e. the current in parallel direction may be carried by a single bundle.

In the transverse direction the current tunnels through more than thousands of junctions (7,000 junctions assuming individual SWNTs with an average diameter of 1.4 nm; ~ 1,400 junctions assuming SWNT bundles with an average diameter of 7 nm); thus, improvement of these junctions dramatically increases the film conductivity.

The presented analysis sheds light into the observed changes of parallel and transverse conductivity of aligned SWNT films in the present device configuration. There are very few (or no) junctions involved in the current transport along the direction of SWNT alignment in contrast to thousands of junctions in transverse direction. The reported results are manifestation of the constructive conductive nature of the bond formed between the Cr atoms and the graphitic SWNT surfaces. The hexahapto bridging of SWNTs is distinct from (i) the classic covalent bond, which introduces sp^3 centers in the SWNT walls and serves as a scattering center leading to conductivity decay in both directions, and (ii) ionic doping (charge transfer) [62-63], which increases the conductivity in parallel direction with little effect on the transverse conductivity.

The developed opto-electronic devices are distinctly different from previously reported approaches in which the optical modulation of carbon nanotubes relies on control (selection) of the carbon nanotube band structure [64] or functionalization with photoactive molecules - chromophores and photosensitive polymers [65]. This novel approach opens

opportunities for design of advance atomic and molecular optoelectronic switches based on carbon nanotubes.

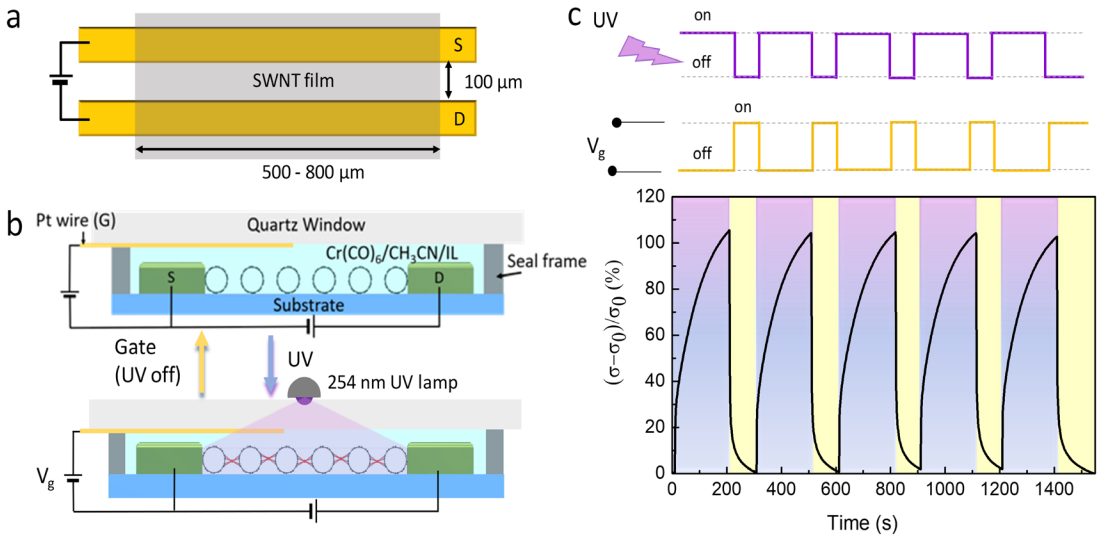

Figure 6.4. Electro-optical switch based on hexahapto-bridged aligned SWNT thin films. a) Device geometry showing the aligned SWNT film on gold contacts before encapsulation b) Schematics illustrating the experimental set-up and the device details: The transverse aligned SWNT film is encapsulated with a solution of Cr reagent and ionic liquid, and a Pt-wire is used to apply potential (top gate). The aligned SWNT film is switched on by irradiation with UV light and turned off by applying gate voltage. c) Change of device conductivity upon UV irradiation and gating.

We demonstrate that the organometallic interconnected aligned SWNTs can be used as optoelectronic devices with a reliable and reversible conductance switching. Because the conductivity of the aligned SWNT thin films in transverse configuration changes dramatically when adjacent nanotubes are atomically bridged with Cr, the ability to reverse the complexation offers a route to engineer a switch. The concept is based on the fact that the formation of the (η^{6}-SWNT)Cr(η^{6}-SWNT) complex is associated with the stable 18-electron electronic configuration. Adding extra electrons to the conduction band (lowest unoccupied molecular orbital, LUMO) is anticipated to destabilize the bond and

electrically decouple the nanotubes. Thus, the aligned transverse SWNT channel can be reversibly switched between a high-conductivity state (ON) using UV light and a low-conductivity state (OFF) by applying a gate potential. For fabrication of a switch, aligned SWNT thin film was placed on a glass substrate with pre-pattered gold, Au, contacts (Figure 6.4a) and sealed with a solution of a Cr-precursor and ionic liquid, IL (Figure 6.4b). The use of ionic liquid as a dielectric affords significantly enhanced charge modulation as compared to solid-state dielectric, due to the large double layer capacitance that occurs at the interface of the film with the IL [66-68]. Applying a positive potential to the Pt-wire results in accumulation of negative ions at its surface and positive ions at the SWNT film surface, with the later acting as ultimately close-laying gate.

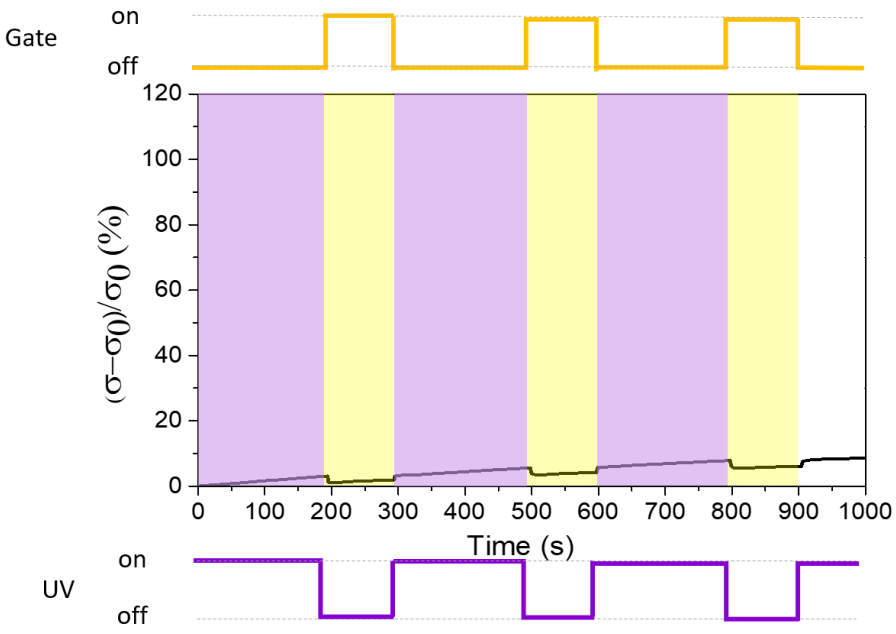

Figure 6.5. Change of conductivity under UV light and gating of aligned SWNT device with ionic liquid: (diethylmethyl(2-methoxyethyl)ammonium bis(trifluoromethylsulfonyl) imide, DEME-TFSI. UV light is 254 nm, source-drain voltage is 0.05 V and gate potential is 0.6 V.

For these experiments the aligned SWNTs were interconnected by exposure to UV light (254 nm) for about 10 min, after which the light was turned off and a gate voltage of +0.6 V was applied. The film electro-optical performance was then tested by in-situ measurement of the response of the SWNT channel resistance during exposure to UV light and gate potential, respectively. Figure 6.4c shows that the conductivity of the device is reversibly modulated by irradiation with UV light (254 nm) and gate potential. The conductivity increases by ~ 100% under UV light and decreases to its initial value when applying gate potential of +0.6 V (Figure 6.4c). The switch between the high-conductivity (on) and low-conductivity states (off) was reversible and stable. As discussed above, the increase of conductivity upon UV light irradiation is due to interconnecting the aligned SWNTs with Cr atoms (facilitated electron transport in transverse direction), whereas the decrease of conductivity during applying gate potential is assigned to reversing the hexahapto bonds. The positive gate potential shifts the Fermi level of the SWNTs increasing the electron population and destabilizing the overlap of the SWNT π-orbitals with the metal d-orbitals. It is important to note that UV irradiation of the SWNT thin film devices fabricated only with IL (without the addition of the Cr-reagent) resulted in negligible change of resistance as shown in Figure 6.5.

Conclusion

In summary, we demonstrated that bis-hexahapto-metal bonds can effectively bridge the surfaces of aligned single-walled carbon nanotube (SWNT) thin films. The formed atomic scale interconnects exert a dramatic effect on the transverse transport properties of SWNT thin films leading to a conductivity increase by a factor of ~20, while preserving the

conductivity in parallel direction. The dramatically different effect of the organometallic chemistry on the electrical conductivity of aligned SWNT films confirms the covalent nature (constructive rehybridization) of the bonds formed between the Cr atoms and SWNT surfaces. This type of bond provides a means to engineer a reliable and stable opto-electronic switch and we demonstrate a transverse-aligned SWNT device, which can be turned on by UV light and off by gate potential. This approach to optically modulate the electronic properties would advance the application of SWNTs in electronics and optoelectronics.

Thin films of interconnected aligned SWNTs may find applications in advanced electronics, opto-electronics and sensor technology. Furthermore, the aligned graphitic surfaces covalently functionalized with transition metals offer a platform for the assembly of ordered magnetic systems [38], which are of potential interest for quantum computing and magnetic nanodevices [69].

References

1. McEuen, P. L., Single-wall carbon nanotubes. *Physical World* **2000,** *13* (6), 31-36.

2. Avouris, P., Molecular Electronics with Carbon Nanotubes. *Accounts of Chemical Research* **2002,** *35*, 1026-1034.

3. Baughman, R. H.; Zakhidov, A. A.; de Heer, W. A., Carbon nanotubes - the Route Toward Applications. *Science* **2002,** *297* (5582), 787-792.

4. Lieber, C. M., Nanoscale Science and Technology: Building a Big Future from Small Things. *MRS Bulletin* **2003,** *28* (7), 486-491.

5. Fuhrer, M. S.; Nygard, J.; Shih, L.; Forero, M.; Yoon, Y.-G.; Mazzoni, M. S. C.; Choi, H. J.; Ihm, J.; Louie, S. G.; Zettl, A.; McEuen, P. L., Crossed Nanotube Junctions. *Science* **2000,** *288*, 494-497.

6. Bekyarova, E.; Itkis, M. E.; Cabrera, N.; Zhao, B.; Yu, A.; Gao, J.; Haddon, R. C., Electronic Properties of Single-Walled Carbon Nanotube Networks. *Journal of the American Chemical Society* **2005,** *127*, 5990-5995.

7. Topinka, M. A.; Rowell, M. W.; Goldhaber-Gordon, D.; McGehee, M. D.; Hecht, D. S.; Gruner, G., Charge Transport in Interpenetrating Networks of Semiconducting and Metallic Carbon Nanotubes. *Nano Letters* **2009,** *9* (5), 1866-1871.

8. Hu, L.; Hecht, D. S.; Grüner, G., Carbon Nanotube Thin Films: Fabrication, Properties, and Applications. *Chemical Reviews* **2010,** *110* (10), 5790-5844.

9. Yu, G. H.; Cao, A. Y.; Lieber, C. M., Large-area Blown Bubble Films of Aligned Nanowires and Carbon Nanotubes. *Nature Nanotechnology* **2007,** *2* (6), 372-377.

10. Li, X.; Zhang, L.; Wang, X.; Shimoyama, S.; Sun, X.; Seo, W. S.; Dai, H., Langmuir-Blodgett Assembly of Densely Aligned Single-Walled Carbon Nanotubes from Bulk Materials. *Journal of the American Chemical Society* **2007,** *129*, 4890.

11. Kinoshita, M.; Steiner, M.; Engel, M.; Small, J. P.; Green, A. A.; Hersam, M. C.; Krupke, R.; Mendez, E. E.; Avouris, P., The Polarized Carbon Nanotube Thin Film LED. *Optics Express* **2010,** *18*, 25738-25745.

12. Cao, Q.; Han, S. J.; Tulevski, G. S.; Zhu, Y.; Lu, D. D.; Haensch, W., Array of Single-Walled Carbon Nanotubes with Full Surface Coverage for High-Performance Electronics. *Nature Nanotech.* **2013,** *8*, 180-86.

13. Engel, M.; Steiner, M.; Sundaram, R.; Krupke, R.; Green, A. A.; Hersam, M. C.; Avouris, P., Spatially Resolved Electrostatic Potential and Photocurrent Generation in Carbon Nanotube Array Devices. *ACS Nano* **2012,** *6*, 7303-7310.

14. Park, S.; Pitner, G.; Giri, G.; Koo, J. H.; Park, J.; Kim, K.; Wang, H.; Sinclair, R.; Wong, H. S. P.; Bao, Z., Large-Area Assembly of Densely Aligned Single-Walled Carbon Nanotubes Using Solution Shearing and Their Application to Field-Effect Transistors. *Advanced Materials* **2015,** *27* (16), 2656-2662.

15. He, X. W.; Gao, W. L.; Xie, L. J.; Li, B.; Zhang, Q.; Lei, S. D.; Robinson, J. M.; Haroz, E. H.; Doorn, S. K.; Wang, W. P.; Vajtai, R.; Ajayan, P. M.; Adams, W. W.; Hauge, R. H.; Kono, J., Wafer-scale Monodomain Films of Spontaneously Aligned Single-walled Carbon Nanotubes. *Nature Nanotechnology* **2016,** *11* (7), 633-638.

16. Kang, S. J.; Kocabas, C.; Ozel, T.; Shim, M.; Pimparkar, N.; Alam, M. A.; Rotkin, S. V.; Rogers, J. A., High-Performance Electronics Using Dense, Perfectly Aligned Arrays of Single-Walled Carbon Nanotubes. *Nature Nanotech.* **2007,** *2*, 230.

17. Engel, M.; Small, J. P.; Steiner, M.; Freitag, M.; Green, A. A.; Hersam, M. C.; Avouris, P., Thin Film Nanotube Transistors Based on Self-Assembled, Aligned, Semiconducting Carbon Nanotube Arrays. *ACS Nano* **2008,** *2*, 2445-2452.

18. Cubukcu, E.; Degirmenci, F.; Kocabas, C.; Zimmler, M. A.; Rogers, J. A.; Capasso, F., Aligned carbon nanotubes as polarization-sensitive, molecular near-field detectors. *Proceedings of the National Academy of Sciences* **2009,** *106* (8), 2495-2499.

19. Xie, X.; Islam, A. E.; Wanab, M.; Ye, L.; Ho, X.; Alam, M. A.; Rogers, J. A., Electroluminescence in Aligned Arrays of Single-Wall Carbon Nanotubes with Asymmetric Contacts. *ACS Nano* **2012,** *6*, 7981-7988.

20. Brady, G. J.; Way, A. J.; Safron, N. S.; Evensen, H. T.; Gopalan, P.; Arnold, M. S., Quasi-ballistic Carbon Nanotube Array Transistors with Current Density Exceeding Si and GaAs. *Science Advances* **2016,** *2* (9).

21. De Heer, W. A.; Bacsa, W. S.; Chatelain, A.; Gerfin, T.; Humphreybaker, R.; Forro, L.; Ugarte, D., Aligned Carbon Nanotube Films - Production and Optical and Electronic-Properties. *Science* **1995,** *268* (5212), 845-847.

22. Hone, J.; Llaguno, M. C.; Nemes, N. M.; Johnson, A. T.; Fischer, J. E.; Walters, D. A.; Casavant, M. J.; Schmidt, J.; Smalley, R. E., Electrical and Thermal Transport Properties of Magnetically Aligned Single Wall Carbon Nanotube Films. *Applied Physics Letters* **2000,** *77* (5), 666-668.

23. Fischer, J. E.; Zhou, W.; Vavro, J.; Liaguno, M. C.; Guthy, G.; Haggenmueller, R.; Casavant, M. J.; Walters, D. E.; Smalley, R. E., Magnetically Aligned Single Wall Carbon Nanotube Films: Preferred Orientation and Anisotropic Transport Properties. *Journal of Applied Physics* **2003,** *93*, 2157-2163.

24. Jia, C. C.; Migliore, A.; Xin, N.; Huang, S. Y.; Wang, J. Y.; Yang, Q.; Wang, S. P.; Chen, H. L.; Wang, D. M.; Feng, B. Y.; Liu, Z. R.; Zhang, G. Y.; Qu, D. H.; Tian, H.; Ratner, M. A.; Xu, H. Q.; Nitzan, A.; Guo, X. F., Covalently bonded single-molecule junctions with stable and reversible photoswitched conductivity. *Science* **2016,** *352* (6292), 1443-1445.

25. Guo, X. F.; Small, J. P.; Klare, J. E.; Wang, Y. L.; Purewal, M. S.; Tam, I. W.; Hong, B. H.; Caldwell, R.; Huang, L. M.; O'Brien, S.; Yan, J. M.; Breslow, R.; Wind, S. J.; Hone, J.; Kim, P.; Nuckolls, C., Covalently bridging gaps in single-walled carbon nanotubes with conducting molecules. *Science* **2006,** *311* (5759), 356-359.

26. Niyogi, S.; Hamon, M. A.; Hu, H.; Zhao, B.; Bhowmik, P.; Sen, R.; Itkis, M. E.; Haddon, R. C., Chemistry of Single-Walled Carbon Nanotubes. *Accounts of Chemical Research* **2002,** *35*, 1105-1113.

27. Bahr, J. L.; Tour, J. M., Covalent chemistry of single-wall carbon nanotubes. *Journal of Materials Chemistry* **2002,** *12* (7), 1952-1958.

28. Hirsch, A., Functionalization of Single-Walled Carbon Nanotubes. *Angewandte Chemie International Edition* **2002,** *41* (11), 1853-1859.

29. Tasis, D.; Tagmatarchis, N.; Bianco, A.; Prato, M., Chemistry of Carbon Nanotubes. *Chemical Reviews* **2006,** *106* (3), 1105-1136.

30. Sarkar, S.; Bekyarova, E.; Haddon, R. C., Covalent Chemistry in Graphene Electronics. *Materials Today* **2012,** *15*, 276-285.

31. Tagmatarchis, N.; Prato, M., Functionalization of Carbon Nanotubes via 1,3-Dipolar Cycloadditions. *Journal of Materials Chemistry* **2004,** *14* (4), 437-439.

32. Lee, Y. S.; Marzari, N., Cycloaddition functionalizations to preserve or control the conductance of carbon nanotubes. *Physical Review Letters* **2006,** *97* (11).

33. Setaro, A.; Adeli, M.; Glaeske, M.; Przyrembel, D.; Bisswanger, T.; Gordeev, G.; Maschietto, F.; Faghani, A.; Paulus, B.; Weinelt, M.; Arenal, R.; Haag, R.; Reich, S., Preserving pi-conjugation in covalently functionalized carbon nanotubes for optoelectronic applications. *Nature Communications* **2017,** *8*.

34. Sarkar, S.; Niyogi, S.; Bekyarova, E.; Haddon, R. C., Organometallic Chemistry of Extended Periodic π-Electron Systems: Hexahapto–Chromium Complexes of Graphene and Single-Walled Carbon Nanotubes. *Chemical Science* **2011,** *2*, 1326-1333.

35. Bekyarova, E.; Niyogi, S.; Sarkar, S.; Tian, X.; Chen, M.; Moser, M. L.; Ayub, K.; Mitchell, R. H.; Haddon, R. C., Stereochemical Effect of Covalent Chemistry on the

Electronic Structure and Properties of the Carbon Allotropes and Graphene Surfaces. *Synthetic Metals* **2015,** *210*, 80-84.

36. Wang, F.; Itkis, M. E.; Bekyarova, E.; Tian, X.; Sarkar, S.; Pekker, A.; Kalinina, I.; Moser, M.; Haddon, R. C., Effect of First Row Transition Metals on the Conductivity of Semiconducting Single-Walled Carbon Nanotube Networks. *Applied Physics Letters* **2012,** *100*, 223111.

37. Bekyarova, E.; Sarkar, S.; Wang, F.; Itkis, M. E.; Kalinina, I.; Tian, X.; Haddon, R. C., Effect of Covalent Chemistry on the Electronic Structure and Properties of Carbon Nanotubes and Graphene. *Accounts of Chemical Research* **2013,** *46*, 65-76.

38. Avdoshenko, S. M.; Ioffe, I. N.; Cuniberti, G.; Dunsch, L.; Popov, A. A., Organometallic Complexes of Graphene: Toward Atomic Spintronics Using a Graphene Web. *ACS Nano* **2011,** *5*, 9939-9949.

39. Gupta, V. K.; Agarwal, S.; Saleh, T. A., Chromium Removal by Combining the Magnetic Properties of Iron Oxide with Adsorption Properties of Carbon Nanotubes. *Water Research* **2011,** *45* (6), 2207-2212.

40. Khani, H.; Rofouei, M. K.; Arab, P.; Gupta, V. K.; Vafaei, Z., Multi-walled Carbon Nanotubes-ionic Liquid-carbon Paste Electrode as a Super Selectivity Sensor: Application to Potentiometric Monitoring of Mercury Ion(II). *Journal of Hazardous Materials* **2010,** *183* (1-3), 402-409.

41. Gupta, V. K.; Nayak, A.; Agarwal, S.; Singhal, B., Recent Advances on Potentiometric Membrane Sensors for Pharmaceutical Analysis. *Combinatorial Chemistry & High Throughput Screening* **2011,** *14* (4), 284-302.

42. Gupta, V. K.; Jain, A. K.; Kumar, P.; Agarwal, S.; Maheshwari, G., Chromium(III)-selective Sensor based on Tri-o-thymotide in PVC Matrix. *Sensors and Actuators B: Chemical* **2006,** *113* (1), 182-186.

43. Gupta, V. K.; Mergu, N.; Kumawat, L. K.; Singh, A. K., A Reversible Fluorescence "off-on-off" Sensor for Sequential Detection of Aluminum and Acetate/Fluoride Ions. *Talanta* **2015,** *144*, 80-89.

44. Sarkar, S.; Zhang, H.; Huang, J.-W.; Wang, F.; Bekyarova, E.; Lau, C. N.; Haddon, R. C., Organometallic Hexahapto Functionalization of Single Layer Graphene as a Route to High Mobility Graphene Devices. *Advanced Materials* **2013,** *25*, 1131-1136.

45. Kalinina, I.; Bekyarova, E.; Sarkar, S.; Wang, F.; Itkis, M. E.; Tian, X.; Niyogi, S.; Jha, N.; Haddon, R. C., Hexahapto-Metal Complexes of Single-Walled Carbon Nanotubes. *Macromolecular Chemistry and Physics* **2012,** *213*, 1001-1019.

46. Pekker, A.; Chen, M.; Bekyarova, E.; Haddon, R. C., Photochemical Generation of Bis-hexahapto Chromium Interconnects Between the Graphene Surfaces of Single-Walled Carbon Nanotubes. *Materials Horizons* **2015,** *2*, 81-85.

47. Wang, F.; Itkis, M. E.; Bekyarova, E.; Sarkar, S.; Tian, X.; Haddon, R. C., Solid-State Bis-Hexahapto-Metal Complexation of Single-Walled Carbon Nanotubes. *Journal of Physical Organic Chemistry* **2012,** *25* (7), 607-610.

48. Tian, X.; Moser, M. L.; Pekker, A.; Sarkar, S.; Ramirez, J.; Bekyarova, E.; Itkis, M. E.; Haddon, R. C., Effect of Atomic Interconnects on Percolation in Single-Walled Carbon Nanotube Thin Film Networks. *Nano Letters* **2014,** *14*, 3930-3937.

49. Thess, A.; Lee, R.; Nikolaev, P.; Dai, H.; Petit, P.; Robert, J.; Xu, C.; Lee, Y. H.; Kim, S. G.; Rinzler, A. G.; Colbert, D. T.; Scuseria, G. E.; Tomanek, D.; Fischer, J. E.; Smalley, R. E., Crystalline Ropes of Metallic Carbon Nanotubes. *Science* **1996,** *273*, 483-487.

50. Haaland, A., The Molecular Structure of Gaseous Dibenzene Chromium, $(C_6H_6)_2Cr$. *Acta Chemica Scandinavica* **1965,** *19*, 41-46.

51. Wang, F.; Itkis, M. E.; Haddon, R. C., Enhanced Electromodulation of Infrared Transmittance in Semitransparent Films of Large Diameter Semiconducting Single-Walled Carbon Nanotubes. *Nano Letters* **2010,** *10*, 937-942.

52. Liu, H. P.; Nishide, D.; Tanaka, T.; Kataura, H., Large-scale Single-chirality Separation of Single-wall Carbon Nanotubes by Simple Gel Chromatography. *Nature Communications* **2011,** *2*, 309(8).

53. Ajiki, H.; Ando, T., Aharonov-Bohm Effect in Carbon Nanotubes. *Physica B* **1994,** *201*, 349-352.

54. Gommans, H. H.; Alldredge, J. W.; Tashiro, H.; Park, J.; Magnuson, J.; Rinzler, A. G., Fibers of Aligned Single-walled Carbon Nanotubes: Polarized Raman Spectroscopy. *Journal of Applied Physics* **2000,** *88* (5), 2509-2514.

55. Jorio, A.; Pimenta, M. A.; Souza, A. G.; Saito, R.; Dresselhaus, G.; Dresselhaus, M. S., Characterizing Carbon Nanotube samples with Resonance Raman Scattering. *New Journal of Physics* **2003,** *5*.

56. Sarkar, S.; Moser, M. L.; Tian, X.; Zhang, X. J.; Al-Hadeethi, Y. F.; Haddon, R. C., Metals on Graphene and Carbon Nanotube Surfaces: From Mobile Atoms to Atomtronics to Bulk Metals to Clusters and Catalysts. *Chemistry of Materials* **2014,** *26* (1), 184-195.

57. Moser, M. L.; Tian, X.; Pekker, A.; Sarkar, S.; Bekyarova, E.; Itkis, M. E.; Haddon, R. C., Hexahapto-Lanthanide Interconnects Between the Conjugated Surfaces of Single-Walled Carbon Nanotubes. *Dalton Transactions* **2014,** *43*, 7379-7382.

58. Moser, M. L.; Pekker, A.; Tian, X.; Bekyarova, E.; Itkis, M. E.; Haddon, R. C., Effect of Lanthanide Metal Complexation on the Properties and Electronic Structure of Single-Walled Carbon Nanotube Films. *ACS Applied Materials & Interfaces* **2015,** *7*, 28013-28018.

59. Kalinina, I.; Al-Hadeethi, Y. F.; Bekyarova, E.; Zhao, C.; Wang, Q.; Zhang, X.; Al-Zahrani, A.; Al-Agel, F.; Al-Marzouki, F.; Haddon, R. C., Solution-phase Synthesis of Chromium-functionalized Single-Walled Carbon Nanotubes. *Materials Letters* **2015,** *142*, 312-316.

60. Chen, M.; Tian, X.; Li, W.; Bekyarova, E.; Li, G.; Moser, M.; Haddon, R. C., Application of Organometallic Chemistry to the Electrical Interconnection of Graphene Nanoplatelets. *Chemistry of Materials* **2016,** *28* (7), 2260-2266.

61. Nirmalraj, P. N.; Lyons, P. E.; De, S.; Coleman, J. N.; Boland, J. J., Electrical Connectivity in Single-Walled Carbon Nanotube Networks. *Nano Letters* **2009,** *9*, 3890-3895.

62. Lee, R. S.; Kim, H. J.; Fischer, J. E.; Thess, A.; Smalley, R. E., Conductivity Enhancement in Single-Walled Carbon Nanotube Bundles Doped with K and Br. *Nature* **1997,** *388*, 255-257.

63. Rao, A. M.; Eklund, P. C.; Bandow, S.; Thess, A.; Smalley, R. E., Evidence for Charge Transfer in Doped Carbon Nanotube Bundles from Raman Scattering. *Nature* **1997,** *388*, 257-259.

64. Avouris, P.; Freitag, M.; Perebeinos, V., Carbon-Nanotube Photonics and Optoelectronics. *Nature Photonics* **2008,** *2*, 341-350.

65. Steuerman, D. W.; Star, A.; Narizzano, R.; Choi, H.; Ries, R. S.; Nicolini, C.; Stoddart, J. F.; Heath, J. R., Interactions between Conjugated Polymers and Single-Walled Carbon Nanotubes. *Journal of Physical Chemistry B* **2002,** *106* (12), 3124-3130.

66. Wu, Z.; Chen, Z.; Du, X.; Logan, J. M.; Sippel, J.; Nikolou, M.; Kamaras, K.; Reynolds, J. R.; Tanner, D. B.; Hebard, A. F.; Rinzler, A. G., Transparent, Conductive Carbon Nanotube Films. *Science* **2004,** *305*, 1273-1276.

67. Bisri, S. Z.; Shimizu, S.; Nakano, M.; Iwasa, Y., Endeaver of Ionotronics: From Fundamentals to Applications of Ion-Controlled Electronics. *Advanced Materials* **2017,** *29*, 1607054.

68. Shimotani, H.; Tsuda, S.; Yuan, H.; Yomogida, Y.; Moriya, R.; Takenobu, T.; Yanagi, K.; Iwasa, Y., Continuous Band-Filling Control and One-Dimensional Transport in Metallic and Semiconducting Carbon Nanotube Tangled Films. *Advanced Functional Materials* **2014,** *24*, 3305-3311.

69. Samouhos, S.; McKinley, G., Carbon nanotube-magnetite composites, with applications to developing unique magnetorheological fluids. *Journal of Fluids Engineering* **2007,** *129* (4), 429-437.

Chapter 7. Summary and perspective

Conclusions and future work

In this dissertation, methods for engineering the morphology of different polyaromatic carbon-based materials have been developed and refined. First, focused ion beam milling was applied to shape PAH crystals in a top-down fashion. The shaped features had a spatial resolution around 100 nm with the majority (90%) of the photoluminescence being retained. FIB shaping of organic crystals demonstrates the possibility of patterning molecular crystals in a top-down fashion using the cleanroom fabrication methods which have already been heavily applied to inorganic materials such as silicon. The main drawback of FIB milling is that the Ga ion beam can dope the sample with Ga atoms during the process. The metal ions inside PAH crystals can affect the photophysical properties of surrounding molecules. A cleaner ion beam such as an He ion beam (HIB) could be applied in the future for better resolution and less doping.[1] A high energy electron beam, which can destroy the organic molecular structure and crystal packing, is also a potential tool to pattern organic PAH crystals.[2]

In addition, surface-passivation of PAH crystals by graphene has also been developed. We have adopted the conventional wet-transfer method of graphene for substrates coated with PAH crystals. Transferred graphene formed a conformal coating around molecular crystals with regular shapes. A slight graphene lattice deformation was detected by Raman spectroscopy. The graphene encapsulated crystals can withstand harsh environments like high temperature, organic solvents, and vacuum for multiple hours, demonstrating the

impermeability and exceptional mechanical stability of the graphene lattice. This work also showed a potential way to modulate the morphology and lattice strain of graphene by transferring graphene on top of a substrate patterned with pre-designed morphological features.

The graphene encapsulation was then compared with hBN encapsulation. We found that monolayer graphene can encapsulate larger crystals with a higher success rate as compared to few-layer hBN. The reason behind this is that graphene has higher flexibility which helps it to wrap around bulk crystals without breaking its lattice integrity. The more rigid few-layer hBN was more subject to breakage when the lattice was deformed by the protruding objects (micro-size PAH crystals in this case). However, the benefit of using hBN is still clear. Compared with the zero-band gap graphene, hBN is a wide band gap (~6 eV) insulator which will not quench the photoluminescence from molecular crystals, at least in theory. Time dependent PL measurements showed that graphene had a more significant quenching effect as compared to few-layer hBN. Surprisingly, there was some energy transfer between PAH dyes and hBN, probably due to defects in the hBN lattice generated during the wet-transfer process. The dry transfer method was found to produce no detectable PL quenching.

In the future, the assembly between molecular crystals and 2D materials can be done in a deterministic fashion using the method that people apply to stack different 2D materials together.[3] A layer of heat release polymer can be used as an adhesive layer to pick up molecular crystals and 2D materials in sequence under a microscope. The microscope can align the target molecular crystal and the target 2D layer on the substrate during the pickup

step. This transfer method will not involve any solvent, so defects in 2D material can be minimized.

Finally, an aligned single wall CNT film was achieved by speed-controlled filtration with low-surfactant concentration. The alignment of the CNTs caused the number of inter-tube junctions to depend on the direction of the applied electrical potential. The conductivity was improved by reducing the junction number in the alignment direction. Further changes in morphology were achieved by interconnecting the aligned CNTs with chromium atoms. The Cr atom between adjacent CNTs can serve as an atomic electrical channel for carriers to pass through, increasing the inter-tube conductance. During the Cr organometallic functionalization, aligned CNT films show a much higher conductivity increase in the transverse (to the CNT alignment) direction as compared to the parallel direction. This was expected because the transverse path contains more junctions for the Cr atoms to bridge.

In the future, the Cr functionalization can be applied to connect other graphitic surfaces beyond carbon nanotubes. It can also be used to bridge graphene/graphene or graphene/CNT interfaces. The functionalization can be a universal way to enhance the electrical performance of large-scale aromatic carbon-based devices.

Perspective on all-carbon-based electronics

This dissertation explores different methods to control the shape, interfaces, and alignments of different polyaromatic carbon materials. Those contributions are the steppingstone for the development of practical all-carbon-based electronics in the future.

There are several essential components that compose a functional electronic device: metallic conductors that transport carriers with minimum resistance, semiconductors that

modulate current under outside stimulation, and insulators that serve as spacers to block charge transfer or to act as optical conductors. The library of carbon-based materials contains all of these components. Graphene and metallic CNT can be the conducting wires to replace traditional metal conductors, such as gold and copper. Semiconducting CNTs and PAHs can serve as semiconductors that cover the bandgap from ultraviolet to infrared. Some wide-bandgap PAHs and polymers can function as insulating spacers or substrates and photonic elements that conduct light. Most electronics such as transistors, light-emitting diodes, photovoltaics, and sensors can already be built by interfacing different carbon-based materials together and connecting them through circuits of metallic CNTs or graphene. To further improve the performance, the inter-material junctions between different graphitic materials, like CNT/CNT, CNT/graphene, and graphene/graphene interfaces, can be bridged by slight Cr doping that provides atomic conducting bridges for better conductivity.

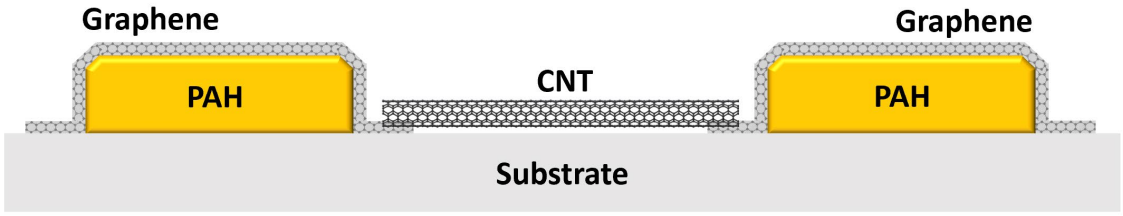

Figure. 7.1. A schematic of a potential all-carbon-based device.

With the development of processing techniques that can manipulate those materials with higher and higher spatial resolution, hopefully, in the near future, all-carbon-based electronics can be built that outperform traditional Si-based electronics with lower cost and better scalability. The computer could be much more lightweight for more cost-efficient

space transportation to the Moon or Mars. The carbon-neutral goal of the entire human civilization could be realized sooner when carbon dioxide in the atmosphere becomes one of the carbon sources to build electronics.

References

1. Cho, E. Y.; Zhou, Y. W.; Cho, J. Y.; Cybart, S. A., Superconducting nano Josephson junctions patterned with a focused helium ion beam. *Applied Physics Letters* **2018,** *113* (2), 022604.

2. Talmon, Y., Electron beam radiation damage to organic and biological cryospecimens. In *Cryotechniques in Biological Electron Microscopy*, Springer: 1987; pp 64-84.

3. Castellanos-Gomez, A.; Buscema, M.; Molenaar, R.; Singh, V.; Janssen, L.; Zant, H. S. J. v. d.; Steele, G. A., Deterministic Transfer of Two-Dimensional Materials by All-Dry Viscoelastic Stamping. *2D Materials* **2014,** *1*, 011002/1-9.